DISSERTATION

DEEP AND SHALLOW OVERTURNING CIRCULATIONS IN THE TROPICAL ATMOSPHERE

Submitted by

Gabriela Mora Rojas

Department of Atmospheric Science

In partial fulfillment of the requirements

For the Degree of Doctor of Philosophy

Colorado State University

Fort Collins, Colorado

Fall 2013

Doctoral Committee:

Advisor: Wayne H. Schubert

Thomas Birner
Mark DeMaria
Eric D. Maloney
Craig W. Trumbo

ABSTRACT

DEEP AND SHALLOW OVERTURNING CIRCULATIONS IN THE TROPICAL ATMOSPHERE

This dissertation examines the dynamics of zonally symmetric, deep and shallow overturning circulations in the tropical atmosphere. The dynamics are discussed in the context of idealized analytical solutions of the equatorial β-plane version of the Eliassen meridional circulation equation that arises in balanced models of the Hadley circulation. This elliptic equation for the meridional circulation has been solved analytically by first performing a vertical normal mode transform that converts the partial differential equation into a system of ordinary differential equations for the meridional structures of all the vertical modes. These meridional structure equations can be solved via the Green's function, which can be expressed in terms of parabolic cylinder functions of half-integer order. The analytical solutions take simple forms in two special cases: (1) Forcing by deep diabatic heating that projects only onto the first internal mode in the absence of Ekman pumping; (2) Forcing by Ekman pumping in the absence of any diabatic heating. Case (1) leads to deep overturning circulations, while case (2) leads to shallow overturning circulations. Both circulations show a marked asymmetry between the winter hemisphere and summer hemisphere overturning cells. This asymmetry is due to the basic anisotropy introduced by the spatially varying inertial stability coefficient in the Eliassen meridional circulation equation. A simple physical interpretation is that fluid parcels forced near the equator to overturn by diabatic and frictional processes tend to move much more easily in the horizontal direction because the resistance to horizontal motion (i.e. inertial stability) is so much less than the resistance to vertical motion (i.e., static stability).

ACKNOWLEDGMENTS

It has been a great honor to obtain my degree and to be a student of the Department of Atmospheric Science at Colorado State University. Several people made this possible and I could not have done it without them. I would like to thank my advisor Dr. Wayne Schubert for his dedication and all the hours spent sharing his vast knowledge. I have received great feedback and support from my committee members, for which I am very thankful. For the support and help, I am thankful to members of the University of Costa Rica: Dr. Jorge Amador, Dr. Rodrigo Carboni, Dr. Eric Alfaro, Dr. Walter Fernandez, as well as the OAICE, UCR for financing my studies and for their understanding. The multiple generations of the Schubert group have always been exceptionally helpful overall, and I would like to thank them in general. I would like to aknowledge the academic, professional and technical help provided by Paul Ciesielski, Rick Taft, Alex Gonzalez, Chris Slocum and Dr. Bernie Connell. I am forever thankful to my parents, sisters and brothers and Geoff for their patience, love and encouragement, for their unconditional support and all the sacrifice throughout all these years. To my closest friends Joyce, Javier, Francisco, and many other friends, thanks for your constant support and for always being there for me.

DEDICATION

This work is dedicated to my parents, Leonel, Ana, Luis Diego, Diego, Paty, Pablo, Fede, Geoff, Marsha, Joe, Joyce.

TABLE OF CONTENTS

LIST OF TABLES

LIST OF FIGURES

CHAPTER 1

INTRODUCTION

The winter and summer hemisphere Hadley cells are well known features of the tropical atmospheric circulation. They consist of ascending motion close to the equator, divergent flow at upper tropospheric levels, convergent flow toward the ITCZ near the surface, and descending motion in the subtropics. In addition to this deep circulation, Zhang et al. (2004) have presented evidence for a shallow meridional circulation (SMC) in the eastern Pacific. As schematically illustrated in Fig. 1.1, this shallow overturning circulation resembles the deep overturning circulation in many respects, but its cross-equatorial return flow occurs just above the top of the frictional boundary layer. This SMC is observed as southerly flow at the lowest levels, with a shallow return northerly flow between 1 and 5 km, in contrast to the well-known northerly flow of the deep Hadley circulation, found between 10 and 12 km. Wang et al. (2005) found that the SMC is strongest between $85°$W and $125°$W, with a tendency to become deeper toward the west, which seems to be correlated with the increase of the inversion height toward the west (Neiburger et al. 1961; von Ficker 1936). Its meridional extent also varies in the zonal direction. For example, east of $105°$W the SMC is confined between $5°$S and the northern Intertropical Convergence Zone (ITCZ), which occurs at $\sim 10°$N, whereas near $120°$W the SMC penetrates to $15°$S.

Zhang et al. (2004) and Nolan et al. (2007) attributed the cause of the SMC to sea surface temperature (SST) gradients. In particular, Nolan et al. (2007) analyzed the SMC as a large-scale sea-breeze type circulation, driven by north-south SST gradients with shallow convection in the ITCZ region. They suggest that these SST gradients induce pressure gradients that produce the SMC; they find that a stronger SMC occurs when deep convection in the ITCZ is absent. In a later paper, Nolan et al. (2010) performed idealized simulations of the ITCZ and its multilevel

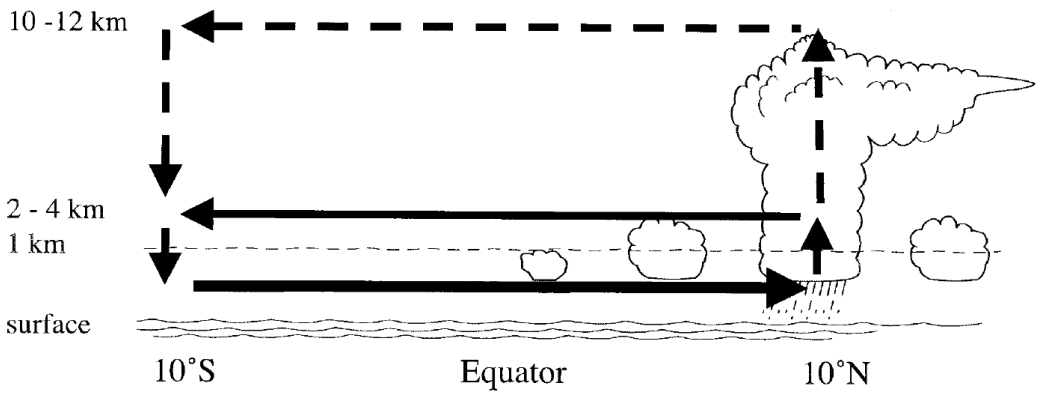

FIG. 1.1. Schematic cross section of the deep (dashed lines) and shallow (solid lines) meridional circulations in the tropical eastern Pacific. From Zhang et al. (2004).

flows. These multilevel flows include: Boundary Layer Inflow (BLI), Shallow Return Flow (SRF), Midlevel Inflow (MLI) and Upper-Level Outflow (ULO). In their study the SRF is analyzed as a sea-breeze-like response to surface gradients of pressure and temperature, in particular, a strong meridional SST gradient near the equator. Their simulations show that both the SRF and the MLI are robust features of the ITCZ in the eastern Pacific. Lindzen and Nigam (1987) proposed this mechanism of surface temperature and pressure gradients to explain low-level wind in the trade cumulus boundary layer, and they found that SST and its gradients are correlated positively in the vertical through the depth of the trade cumulus layer.

From previous global analyses, it appears that shallow meridional circulations occur in several other parts of the globe. For example, Trenberth et al. (2000) studied the mean annual cycle of the divergent wind and vertical motion using both the NCEP-NCAR reanalysis and the ECMWF reanalysis. They applied a complex empirical orthogonal function (CEOF) analysis to the divergent wind, which produced two dominant modes of overturning throughout the tropical and subtropical troposphere. The first mode (CEOF1) is the deep overturning global monsoon mode in the troposphere, with a maximum in vertical motion at approximately 400 hPa, divergence in the upper troposphere (with a maximum at 150 hPa), and convergence in the lower troposphere with a

maximum at 925 hPa (ECMWF) or 850 hPa (NCEP). The Hadley circulation, the Pacific and Atlantic Walker cells, and the Asia-Africa transverse cell are part of this deep overturning mode. The CEOF1 has a maximum in July and a secondary maximum in January.

The CEOF2 is the lower-tropospheric overturning cell centered about 800 hPa, where it reaches its maximum vertical velocity, with outflow from 750 to 350 hPa and inflow peaking at 925 hPa. This second mode is strong over Africa, migrating back and forth across the equator with the seasons. It is also observed in the Middle East, Australia, the tropical eastern Pacific and the Atlantic. The upward motion peaks at $10°$N in August and at $10°$S in February. The downward motion peaks at $25°$N in February and at $30°$S in August. Two examples from the Trenberth et al. (2000) analysis are shown in Figures 1.2 and 1.3. Figure 1.2 shows the regional meridional cross section of the divergent flow, averaged between $170°$W and $90°$W, for July. This example illustrates the simultaneous occurrence of deep and shallow Hadley cells. In contrast, Figure 1.3 shows the regional meridional cross section of the divergent flow, averaged between $30°$W and $10°$E, for January. This example illustrates the occurrence of the shallow Hadley cell during a period when the deep Hadley cell is largely absent.

Observational insights into the role of sea surface temperature in boundary layer processes in the eastern tropical Pacific have been provided by Wallace et al. (1989) and Deser et al. (1993). They found that northward moving boundary layer flow, upon crossing into the cold SST tongue at $1°$S, is stabilized to such an extent as to inhibit the downward turbulent mixing of northward momentum from aloft, due to the high static stability (Chelton et al. 2000b). As this low-level air subsequently flows across the equator and over the SST frontal zone at $2°$N (i.e., toward warmer waters), the boundary layer is destabilized, leading to increased turbulence and therefore increased downward mixing of northward momentum. The low-level wind thus displays strong horizontal

divergence as it moves through the frontal zone. These northward winds are influenced by the El Niño/Southern Oscillation and the annual cycle, with stronger flow during the cold seasons, in particular during cold seasons of warm years. Satellite images and SST data were used by Deser et al. (1993) to test the hypothesis that cool low-level winds blowing across the SST front in the equatorial eastern Pacific produce stratiform clouds on the warm side of the front. When the front is strong (weak), there is a maximum (minimum) of cloudiness. A strong (weak) front is found during cold (warm) ENSO episodes. Lindzen and Nigam (1987) argued that the motion in the lower layer of the trade cumulus boundary layer is due to the pressure gradients resulting from the SST distribution. Similar results were found by Back and Bretherton (2009a), who showed that the distribution of convergence is primarily due to boundary layer temperature gradients related to SST gradients.

It appears that all SMCs undergo marked seasonal cycles, reaching their peak in different seasons at different longitudes: Spring over West Africa, Summer over the Atlantic Ocean and Fall over the Eastern Pacific. SMCs can be classified into two types: (i) the maritime ITCZ type and (ii) the summer monsoon type (Zhang et al. 2008). Stratocumulus clouds are found north and south of the equator. Using data from EPIC 2001 to study the atmospheric boundary layer over the cold tongue and ITCZ, de Szoeke et al. (2005) found that during the boreal fall, a weak return circulation is present above the boundary layer along $95°$W, between 1.2 and 2.8 km height, $3°$N and $8°$N with average speed of 1.25 m s^{-1}. The area between $1°$N and $3°$N shows the highest cloud fraction of stratocumulus and they lay over the convective mixed layer, whereas stratocumulus south of the equator are found near the inversion base. The authors interpret these southern clouds as residual stratocumulus maintained by cloud-top radiative cooling. The area over the cold tongue displays occasional thin altostratus clouds above the boundary layer. The radiative cooling caused

by the presence of these clouds strengthens the SST gradients, enhances the southeast trade winds and therefore increases precipitation in the ITCZ region north of the equator. The authors then argue that, if the cloud-radiative effect over the southeast Pacific is removed, the boundary layer clouds almost disappear south of the equator and the precipitation in the ITCZ north of the equator would be reduced by 15%-20% over the eastern Pacific. The maximum net cloud-induced radiative cooling found by Wang et al. (2005) through the use of a linear steady state primitive equation model, was 2 K day^{-1}, which drives an anomalous surface southerly flow of 2 m s^{-1}. According to Masunaga and L'Ecuyer (2010), clouds offset the net radiation by 10–15 W m^{-2} throughout the year in the tropical southeast Pacific. If these clouds were not present, a double ITCZ would also be present during the boreal Fall. This short-wave reflection by high clouds of the southern ITCZ produces a meridional asymmetry of the annual mean climatology of the absorbed shortwave flux, with a marked difference of 40 W m^{-2} between $10°$S and $10°$N (Masunaga and L'Ecuyer 2011). Using the same data from EPIC 2001, McGauley et al. (2004) found the strongest meridional wind between 0 and $5°$N; however, these winds do not accelerate due to the forcing of the strong pressure gradient found in the boundary layer. The meridional pressure gradient reverses sign above 1 km at certain latitudes, resulting in reversal of the meridional wind near 1200 m, where the northerlies are strongest near $5°$N.

The treatment of the circulation between $10°$S and $10°$N as a sea-breeze circulation (Nolan et al. 2007) does not account for important mechanisms such as the variation of the Coriolis parameter with latitude, which causes important variations in the inertial stability. Vorticity in the region of the ITCZ produces Ekman pumping out the boundary layer. The most likely horizontal trajectory for this air is toward an area with low inertial stability (low resistance to displacement due to the Coriolis force), i.e., equatorward rather than poleward where the inertial stability $\beta^2 y^2$ is larger

and the inertial stability more effectively retards the flow. In the present study we explore the hypothesis that Ekman pumping out of the boundary layer is one of the driving mechanisms for the SMC.

Over the past several decades, considerable understanding of Hadley cell dynamics has been obtained through the use of idealized analytical and numerical models of zonally symmetric flow. For example, using the Held and Hou (1980) numerical model of zonally symmetric Hadley cells, Lindzen and Hou (1988) simulated the seasonal migration of these cells in response to the north-south migration of the sea surface temperature maximum. Their results show that, as the center of the heating moves off the equator, the latitude separating the winter and summer cells moves much further into the summer hemisphere while the summer cell becomes negligible. The summer cell is the one found in the hemisphere where the ITCZ is located, while the winter cell is found in the opposite hemisphere. Using a high resolution version of the numerical model, steady state solutions were found, and the meridional streamfunctions were computed for cases with the heat source located at the equator, 2°N, and 6°N. Symmetric cells centered on the equator were found when the heat source is located at the equator, but when the heat source is at 2°N, the winter cell is 50% stronger than the symmetric cells, while the summer cell is half the strength of the symmetric cells. The latitude where the two cells meet is no longer the area of maximum vertical velocity; instead, it remains near the latitude of the heat source. When the heat source is located at 6°N, the winter cell dominates and it is more than four times as intense as the symmetric cells. The meridional displacement of the ITCZ was studied by Kang et al. (2008) using a GCM coupled to a slab mixed layer ocean. In their experiments, the northern extratropics are cooled and the southern extratropics are warmed by a cross-equatorial flux beneath the mixed layer, in simple words, heat is substracted from one hemisphere and simultaneously added to the other hemisphere. This

procedure forced a southward displacement of the ITCZ and subsidence is created in the tropics of the cooler hemisphere, favoring low-level clouds. The asymmetry between the summer hemisphere and winter hemisphere Hadley cells was also explored by Hack et al. (1989) and Hack and Schubert (1990) using dynamical arguments based on the Eliassen meridional circulation equation (with variable coefficients: static stability, baroclinicity and inertial stability) and by Schubert et al. (1991) based on potential vorticity dynamics. These dynamical arguments are quite different than those used by Lindzen and Hou (1988) since they are not based on a steady state assumption, but rather involve wind and mass fields that are evolving into states that satisfy the Charney-Stern necessary condition for combined barotropic-baroclinic instability. Another possible aspect of the dynamics was noted by Tomas and Webster (1997), who point out that strong cross-equatorial flow can lead to an area in the meridional plane, between the equator and the zero absolute vorticity surface, where $f(f+\zeta) < 0$, i.e., the absolute vorticity $(f+\zeta)$ has the opposite sign of the Coriolis parameter f, which is the condition for inertial instability. Whether this potential instability plays an important role in the Hadley circulation remains an open question.

To address both the deep and shallow overturning problems, the present study uses a zonally symmetric, equatorial β-plane model. From the governing equations for this simplified model we derive a meridional circulation equation for the streamfunction. This equation has two variable coefficients—the static stability and the inertial stability. It also has two forcing effects—the diabatic heating, which appears in the interior equation, and the boundary layer frictional pumping, which appears in the lower boundary condition. By assuming that the diabatic heating and the boundary layer pumping are confined to the ITCZ region, other types of circulations not related to the present study are eliminated. The meridional circulation equation is solved analytically using vertical and horizontal transform methods. These analytical solutions serve as the basis for

a better understanding of the processes that force deep and shallow overturning circulations and the dynamics that leads to large asymmetries between winter hemisphere and summer hemisphere Hadley cells.

The dynamics are presented in the context of idealized analytical solutions of the meridional circulation equation that arises in the zonally symmetric model of the Hadley circulation. Under certain simplifications of its coefficients, this elliptic partial differential equation for the meridional circulation can be solved by first performing a vertical transform to obtain a horizontal structure equation from which arises the concept of a spectrum of Rossby lengths. In the tropics, Rossby lengths are large and Rossby depths are small, so the interior circulation associated with Ekman pumping cannot penetrate deep into the troposphere. The purpose of this dissertation is to examine several other dynamical aspects, which in addition to the hypothesis of sea surface temperature gradients, appear to play an important role in understanding the SMC. The three dynamical aspects examined here are: (i) Ekman pumping out of the boundary layer in the high vorticity region of the ITCZ; (ii) low inertial stability in the equatorial region, causing most of the Ekman pumped air to be returned across the equator; (iii) a spectrum of small Rossby depths, causing the return flow to be trapped just above the boundary layer.

The arguments presented here are based on the assumption of balanced zonal flow. If the zonal flow is balanced in the sense that it is continuously evolving from one geostrophically balanced state to another, then the meridional circulation is determined by the solution of a second order partial differential equation in the (y, z)-plane. According to this "meridional circulation equation", the streamfunction for the poleward and vertical motion is determined by the following factors: the meridional derivative of the diabatic heating, the Ekman pumping at the top of the boundary layer, the static stability, and the inertial stability. Although solutions of the meridional

circulation equation generally yield poleward and vertical velocities that are much weaker than the zonal velocity, the poleward and vertical directions are the directions of large gradients, so the relatively weak meridional circulation is crucial for zonal flow evolution.

The remainder of this dissertation is organized as follows. In Chapter 2, data from the "Year of Tropical Convection (YOTC)" is used to examine the boreal summer wind fields and cloud distributions in the eastern Pacific, where the SMC has been previously observed. The design of a simplified, zonally symmetric model of the deep and shallow Hadley circulations is presented in Chapter 3. This chapter presents the governing equations (section 3.1), the vertical transform method that transforms the meridional circulation equation from a partial differential equation in (y, z, t) into a system of partial differential equations in (y, t) for the meridional structure of each vertical mode (section 3.2), and finally the solution of these partial differential equations via both a Green's function method (section 3.3) and a Hermite transform method (section 3.4). Chapter 4 discusses the analytical solutions obtained in Chapter 3, concentrating on two interesting cases: (1) Deep overturning circulations, representing the deep Hadley circulation forced by diabatic heating in the ITCZ region; (2) Shallow overturning circulations, in this case forced by Ekman pumping out of the top of the boundary layer in the high vorticity region of the ITCZ. Conclusions are given in Chapter 5. Several detailed mathematical derivations of the differential equation solution methods are given in the appendices.

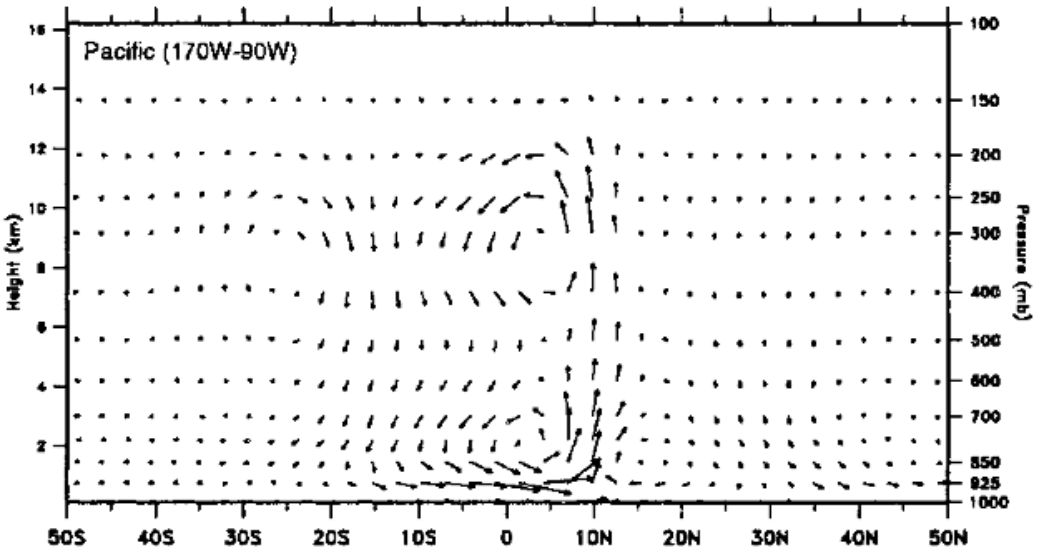

FIG. 1.2. Regional meridional cross section (170°W to 90°W) of the divergent mass flux as vectors from 50°S to 50°N, derived from ECMWF data for July. The mass flux scale is is given below Figure 1.3. From Trenberth et al. (2000).

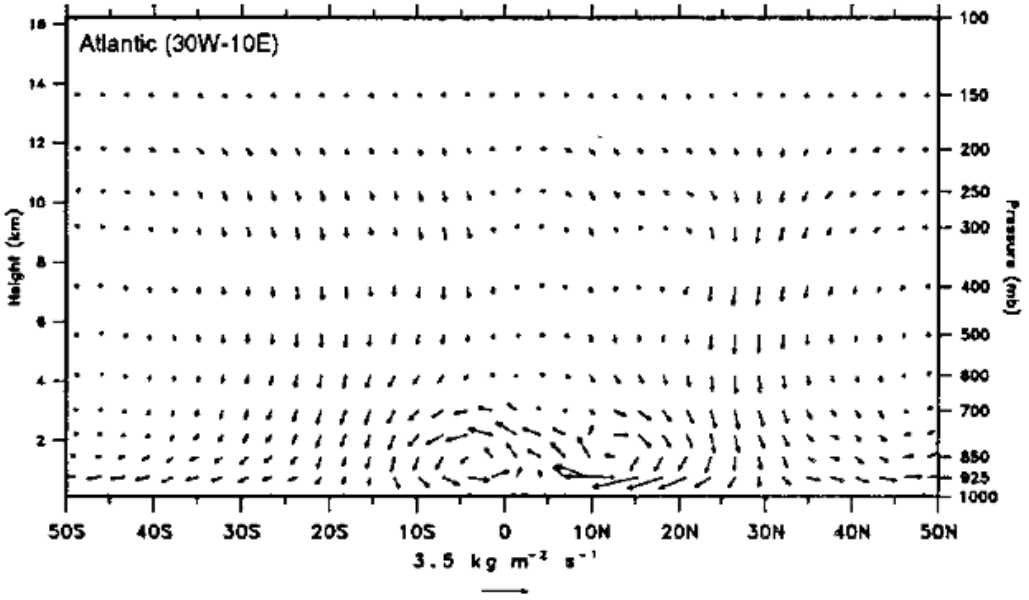

FIG. 1.3. Regional meridional cross section (30°W to 10°E) of the divergent mass flux as vectors from 50°S to 50°N, derived from ECMWF for January. The mass flux scale is below the figure. From Trenberth et al. (2000).

CHAPTER 2

AN OBSERVATIONAL ANALYSIS OF THE EASTERN PACIFIC USING YOTC DATA

Analysis from the research program known as the Year of Tropical Convection (YOTC) (Waliser et al. 2012) is used in this chapter to examine the relationship of SSTs, clouds, and low-level circulation features over the Eastern Pacific during boreal summer. The temporal resolution of the YOTC analysis fields is 6 h and the horizontal resolution is $0.5^\circ \times 0.5^\circ$ with 15 irregularly spaced vertical levels between 1000 and 100 hPa. YOTC analyses are available for the 2-yr period between May 2008 and April 2010. Although originally proposed to be a 1-yr research program, YOTC was extended for an additional year in order to capture both La Nina and El Nino phases of an ENSO cycle. In this chapter we only consider analyses from the boreal summer of 2009, during which time the Multivariate ENSO Index ranged from 0.36 to 0.96 corresponding to weak warm anomalies over the Eastern Pacific. The excellent agreement between ECMWF and QuikSCAT surface divergence and vorticity analyses over the tropical Eastern Pacific, found by McNoldy et al. (2004), gives us confidence that the ECMWF-based YOTC analyses are accurately depicting conditions over this region. However, it must be kept in mind that the YOTC analyses provide only 2 years of data.

During May, an area of warm water known as the Western Hemisphere Warm Pool (WHWP) starts to develop in the Eastern Tropical Pacific. The evolution of SSTs over this region in boreal Spring, Summer and Fall 2009 is shown in Fig. 2.1. The WHWP, defined as the region covered by water warmer than 28.5°C (Wang and Enfield 2001, 2005; Enfield and Lee 2005), provides an environment conducive for producing deep convective clouds and upper-level cirrus. The 28.5°C isotherm and the oceanic mixed layer have an annual average depth of 25 m. The WHWP is divided into four regions: Eastern North Pacific (ENP), Gulf of Mexico, western Tropical North

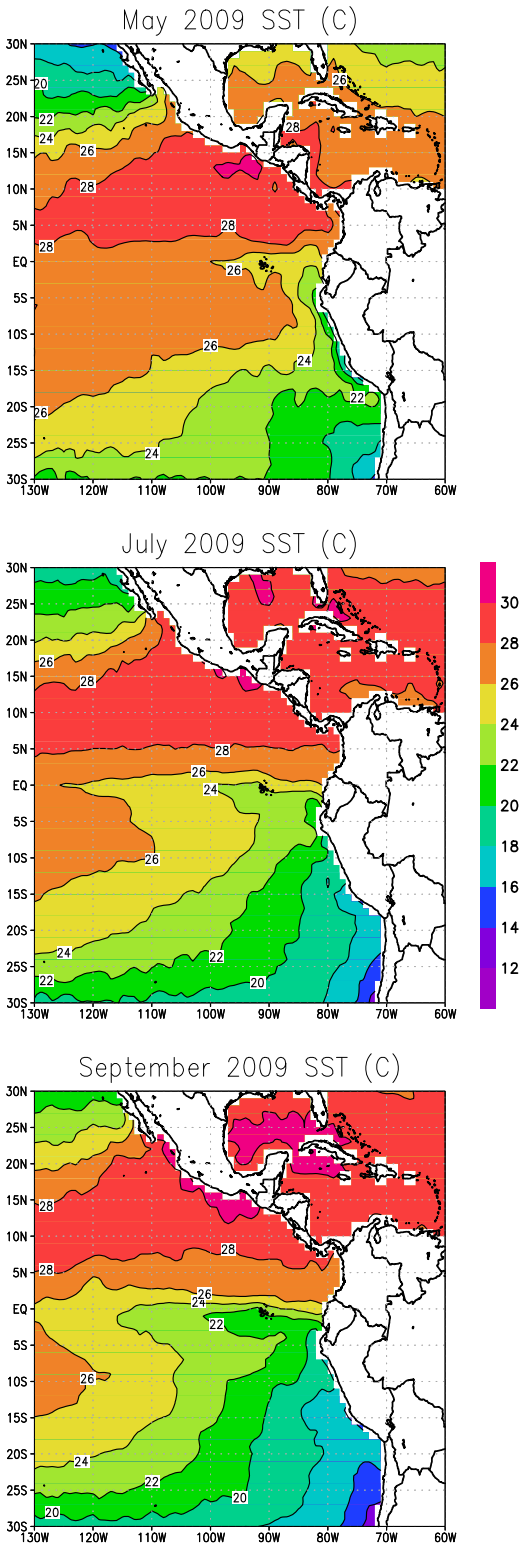

FIG. 2.1. Sea surface temperature (°C) for May, July, and September 2009. Note the development of the cold tongue along the equator, the SST front just north of the Galapagos, and SSTs warmer than 30°C in September.

Atlantic (TNA) and Caribbean. These four regions correspond to areas of hurricane genesis and development.

High and low cloudiness superimposed with surface winds over this region for September 2009 are shown in Figs. 2.2 and 2.3. Low clouds are usually found between the surface and 2 km while high clouds are located above 8 km. As seen here low-level trade winds from the Southern Hemisphere converge strongly with those of the Northern Hemisphere forming an ITCZ at approximately 10°N (Fig. 2.3). High level clouds can be seen near the average position of the ITCZ (low-level wind convergence) whereas low-level clouds are found south of the ITCZ, including the southeastern Pacific, which correspond to areas of maximum meridional low-level wind (Fig. 2.2). As it was pointed out by Philander et al. (1996), thin layers of stratus clouds develop in regions of subsidence where the surface winds evaporate water vapor from the ocean. A strong low-level atmospheric inversion traps this moist air, forming stratus clouds at the base of the inversion.

Low-level convergence associated with the ITCZ in the eastern tropical Pacific is located between 2.5°N and 15°N (Figs. 2.4–2.6), with maximum surface southerly winds between the equator and 5°N (e.g., Fig. 2.10). These results are consistent with the QuikScat divergence patterns found in Fig. 3 of McNoldy et al. (2004), although their average values are over 4 years (1999–2002). The strongest values of low-level divergence are found between the equator and 2°N, with less-well-defined convergence often occuring near 5°S, noting of course that the YOTC data sample pnly a brief period during the transition from La Nina to El Nino. During these summer months, cyclonic vorticity is present north of 8°N, zero relative vorticity near 7°N (white shading) and anticyclonic vorticity south of 7°N (Figs. 2.7–2.9).

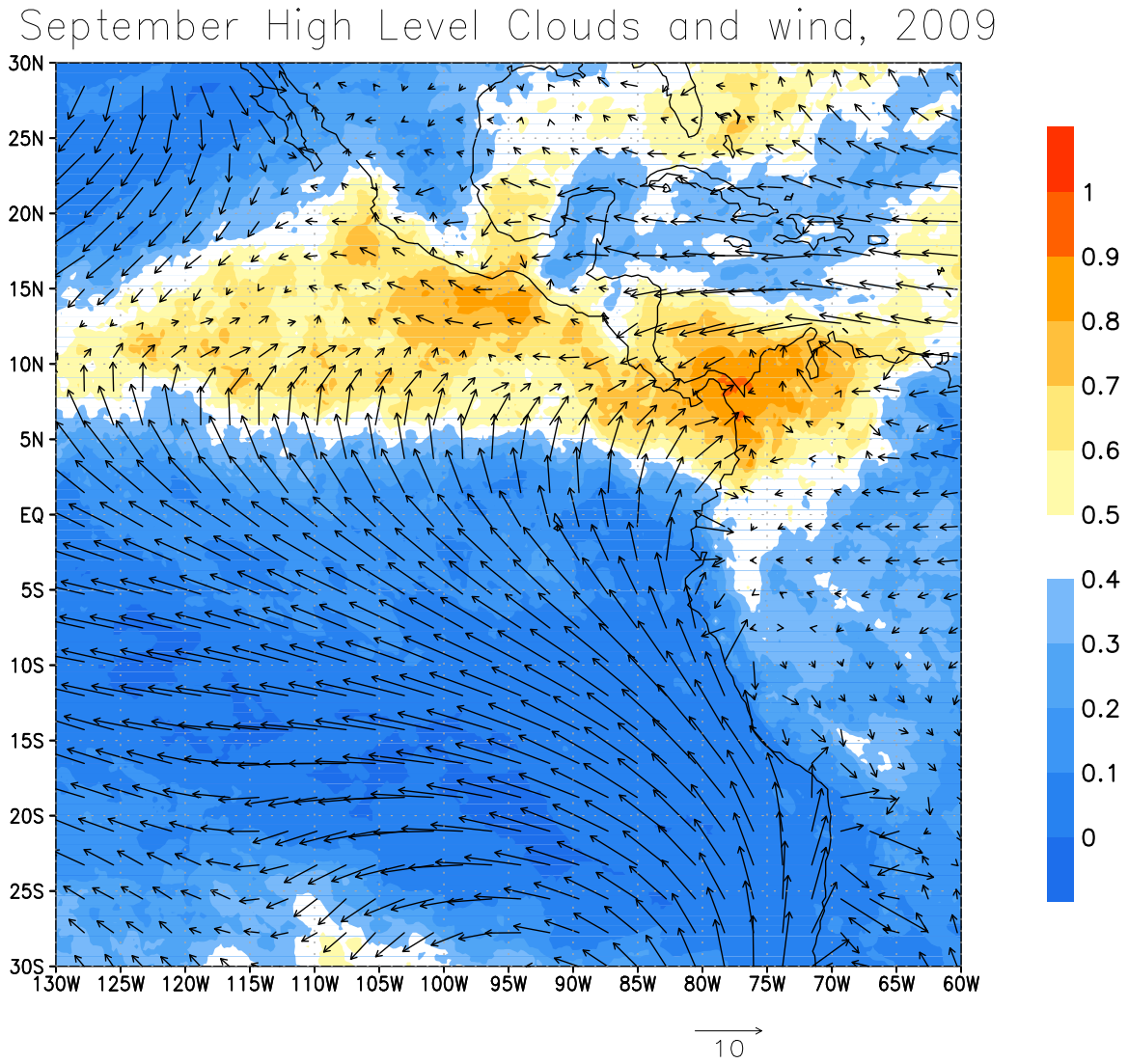

FIG. 2.2. Fractional high-level cloud cover (scale on right) and surface wind (with the reference 10 m s^{-1} vector shown at the bottom).

By July the ITCZ is genallly located between 8°N and 10°N (Fig. 2.5), and it continues moving north until September, when it reaches its northernmost position, often slightly north of 10°N (Fig. 2.6). Strong low-level southerly winds south of the ITCZ display magnitudes between 4 to 7 m s^{-1} (Fig. 2.10), and start decreasing in magnitude and horizontal extent during October (not shown).

As mentioned in Chapter 1, as part of the SMC, a shallow return flow (northerly winds) near the equator has been observed over the Eastern Pacific in the lowest 2–5 km of the atmosphere.

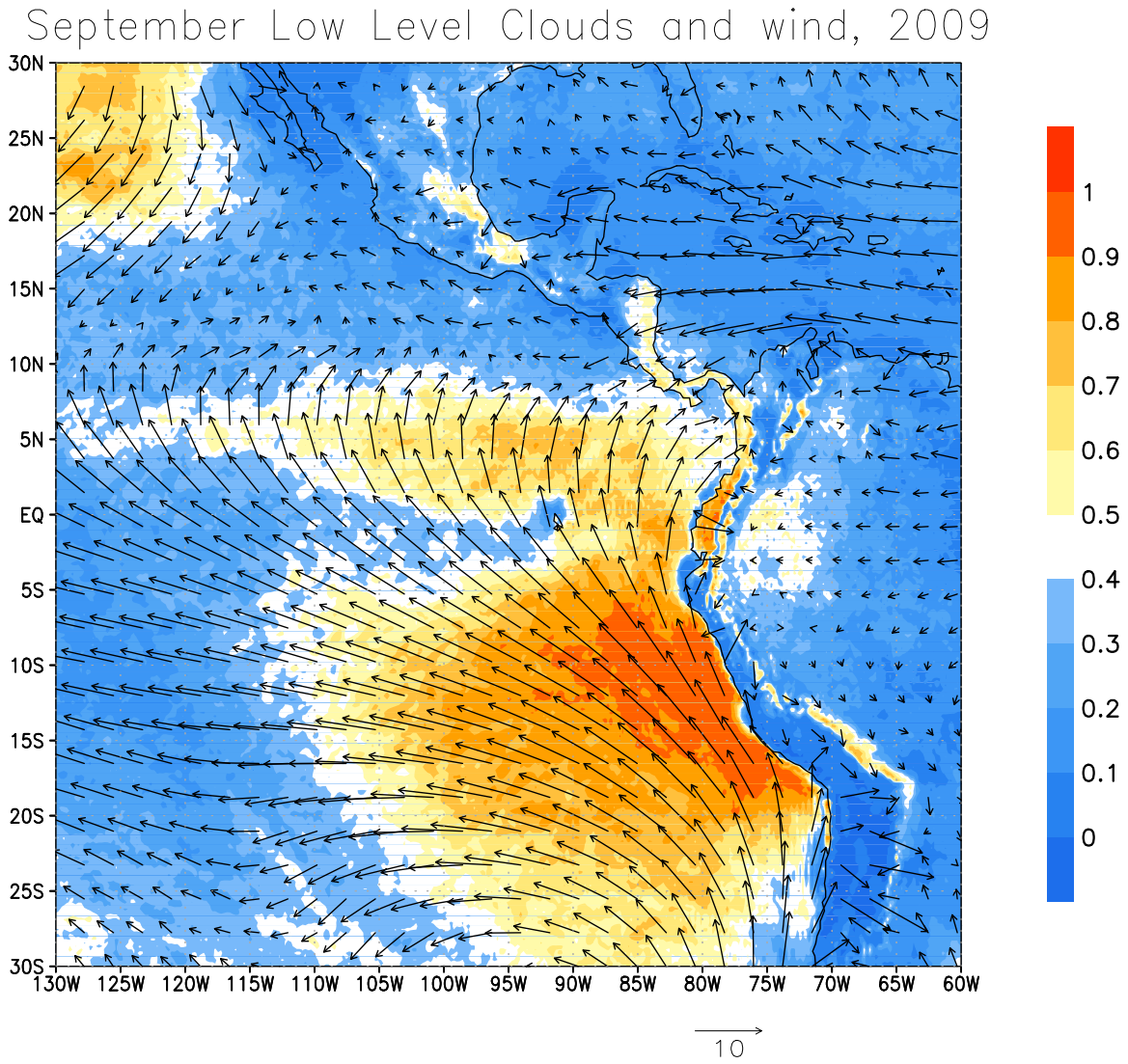

FIG. 2.3. Fractional low-level cloud cover (scale on right) and surface wind (with the reference 10 m s^{-1} vector shown at the bottom).

To examine the characteristics of the SMC over this region in more detail, Figs. 2.11–2.13 show monthly-averaged cross sections of YOTC meridional winds between 85°W and 95°W for the months of May, July and September 2009, respectively. The upper panels, which show the full depth of the troposphere, reveal the traditional deep Hadley circulation with a stronger cross-equatorial cell and upper-level northerlies to the south of the ITCZ. To better reveal details of the lower-level SMC, the bottom panels of Figs. 2.11–2.13 focus on the 1000–600 hPa layer. As noted in earlier figures, low-level winds converge between 5°N and 10°N during these months. To

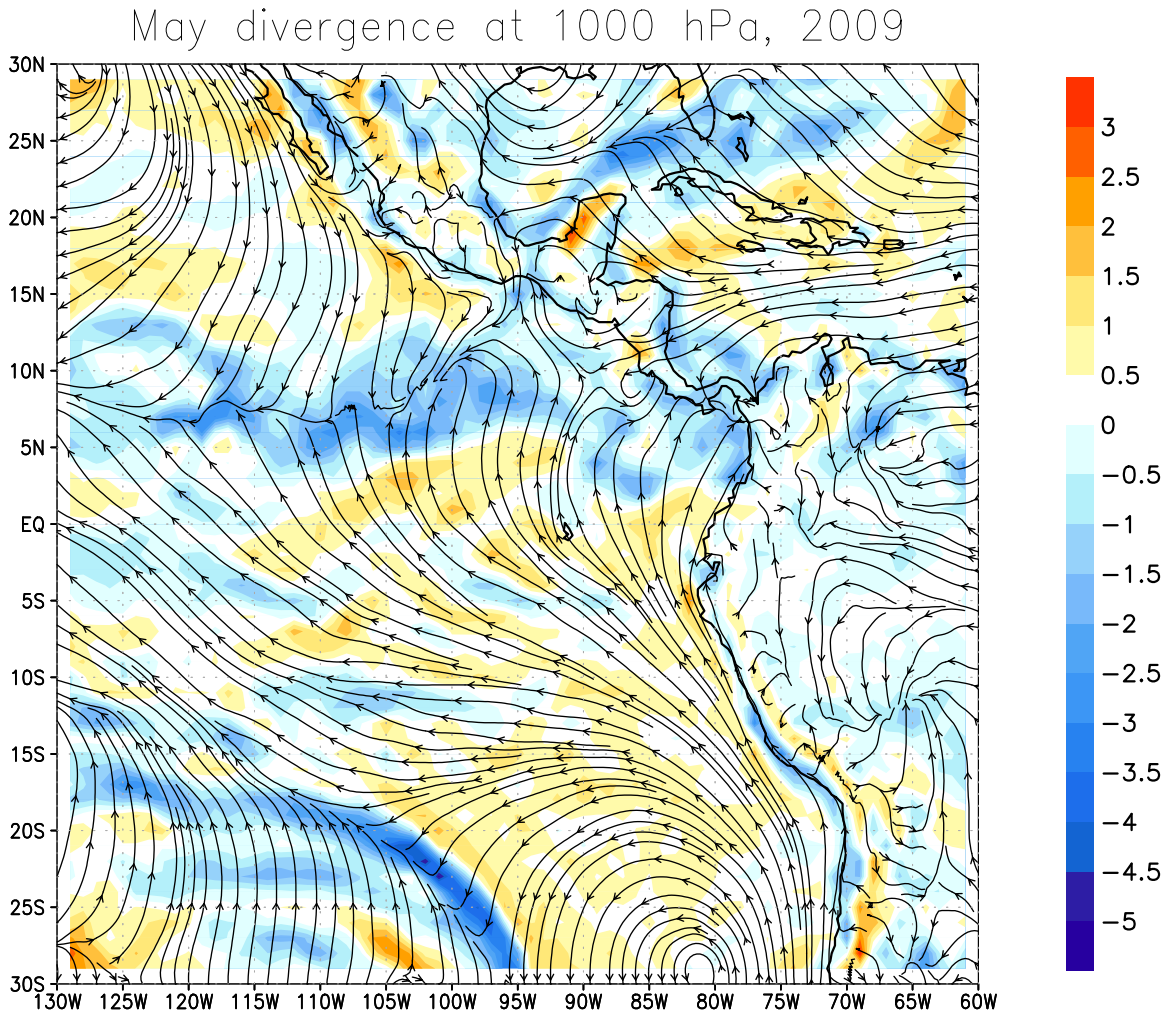

FIG. 2.4. May divergence (scale at right in units of 10^{-5} s^{-1}) and streamlines at 1000 hPa.

the south of the ITCZ, low-level southerlies with peak speeds between 6 and 7 m s^{-1} are observed between $20°$S and $10°$N. Above the southerlies, a weak northerly (1–2 m s^{-1}) return flow centered near $2.5°$N is observed between 700 and 800 hPa. Although not shown here, this shallow return flow in the YOTC analyses deepens and its meridional extent increases towards the west, consistent with the findings of Wang et al. (2005). Some strengthening of the SMC between May and the later months is consistent with wind profiler observations from this region (Zhang et al. 2004). To the north of the ITCZ, low-level northerlies are present roughly between $10°$N and $20°$N, with no evidence of a shallow southerly return flow to the north. Note that the northerly maximum in July

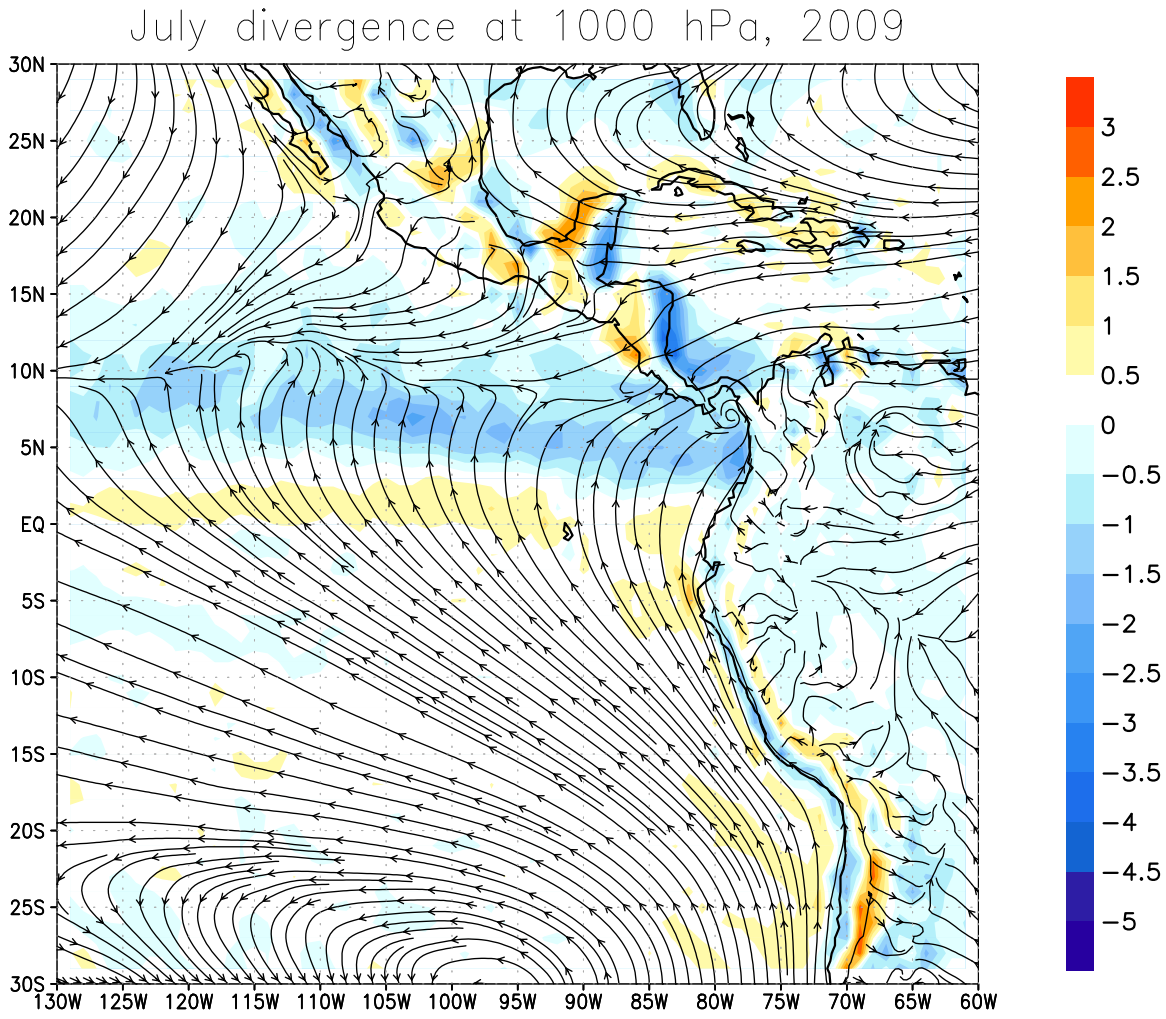

FIG. 2.5. July divergence (scale at right in units of 10^{-5} s^{-1}) and streamlines at 1000 hPa.

found near 12°N and 900 hPa is partially a reflection of the Papagayo Jet (Chelton et al. 2000a) which has a peak northerly component near 925 hPa.

The characteristics of the SMC, and in particular, the northerly return flow between 800 hPa and 700 hPa in the 2009 YOTC analyses are largely consistent with the Tropical East Pacific observations of this flow presented in Zhang et al. (2004). With such consistency between model analyses and observations, examining additional years of model analyses and interannual variability patterns, would be helpful in understanding the variability of the SMC in this region.

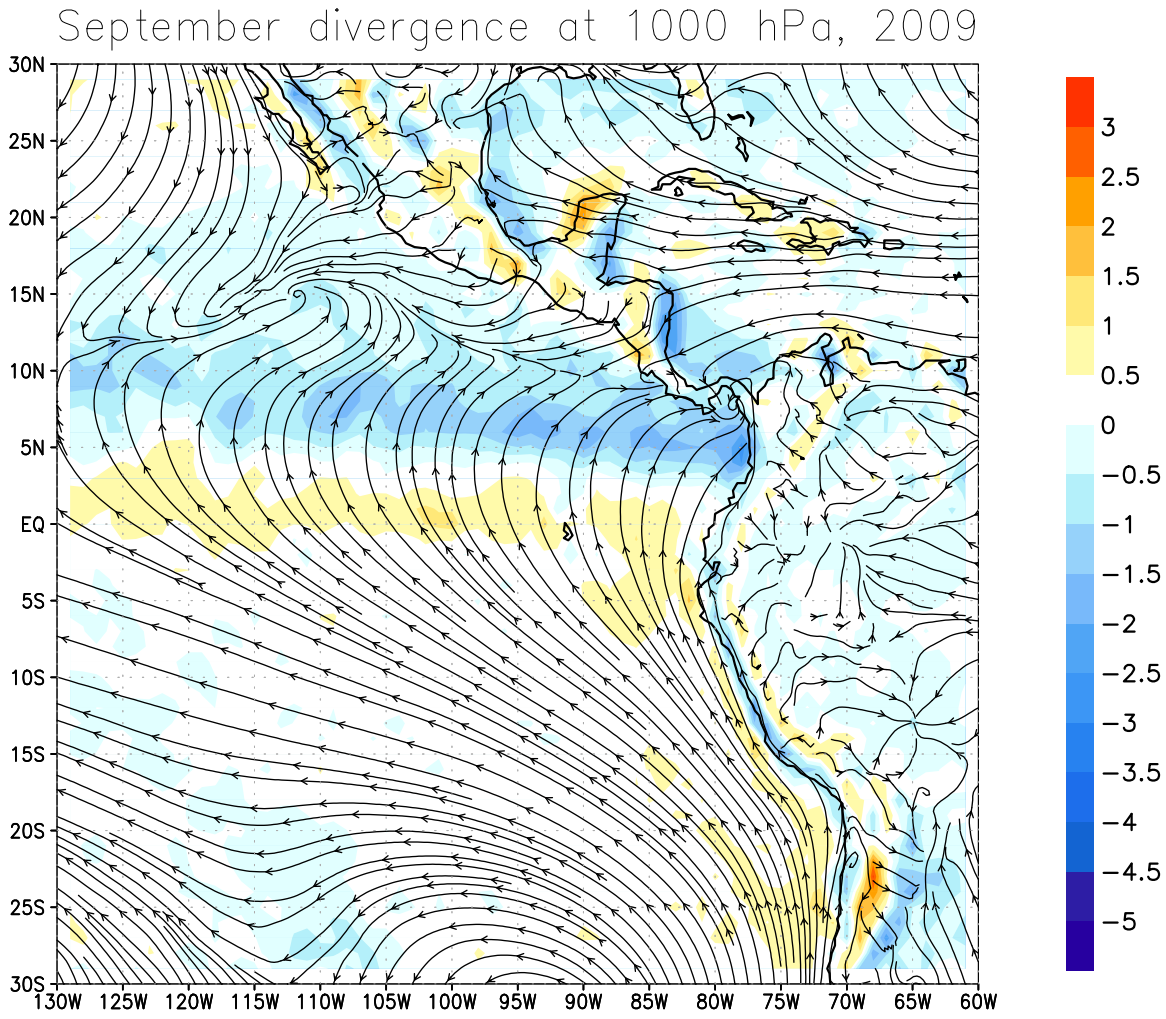

FIG. 2.6. September divergence (scale at right in units of 10^{-5} s^{-1}) and streamlines at 1000 hPa.

In the following two chapters we derive and solve the equations for a simple, zonally symmetric model that elucidates some of the fundamental dynamics of these deep and shallow overturning circulations.

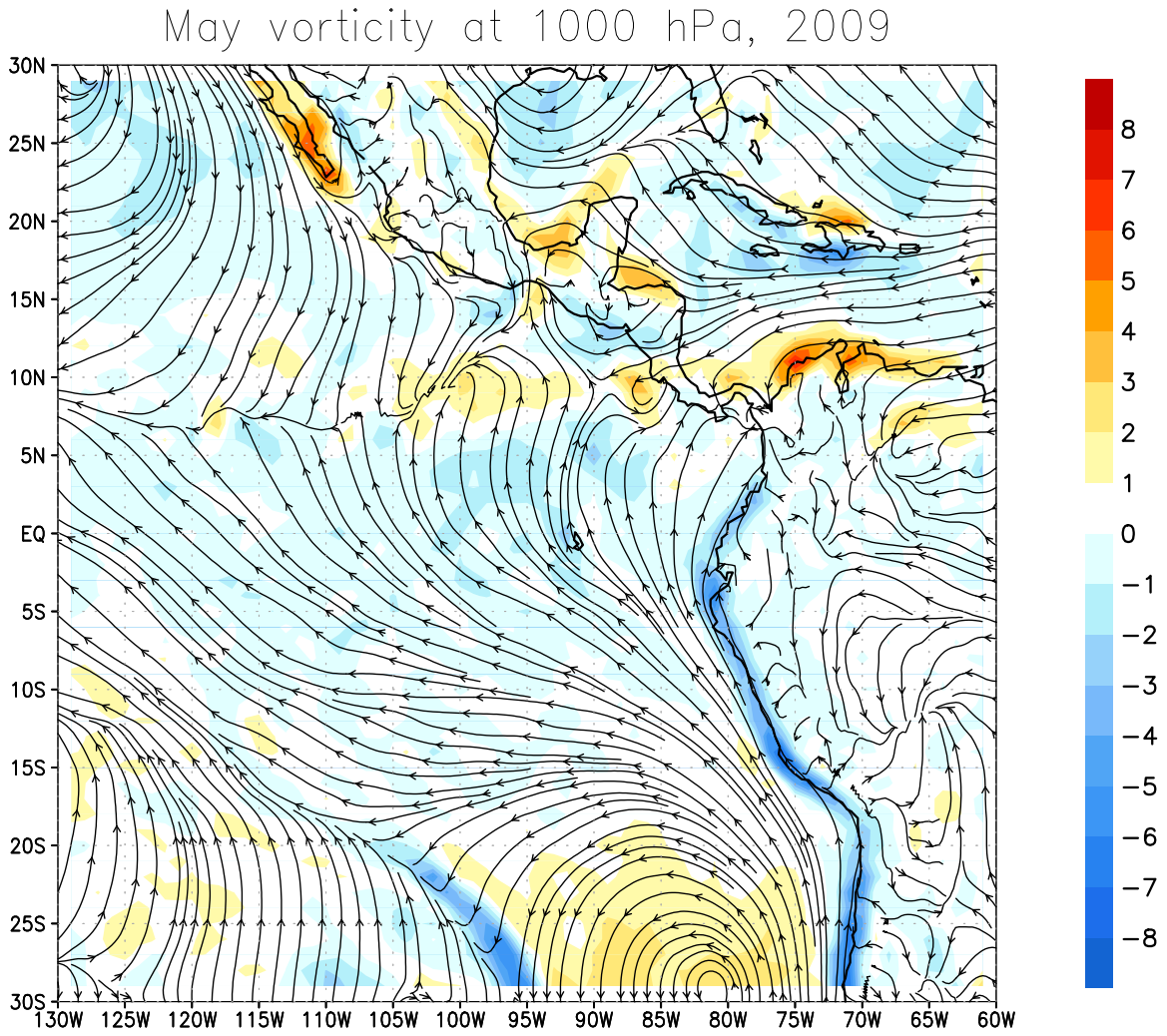

FIG. 2.7. May vorticity (scale at right in units of 10^{-5} s^{-1}) and streamlines at 1000 hPa.

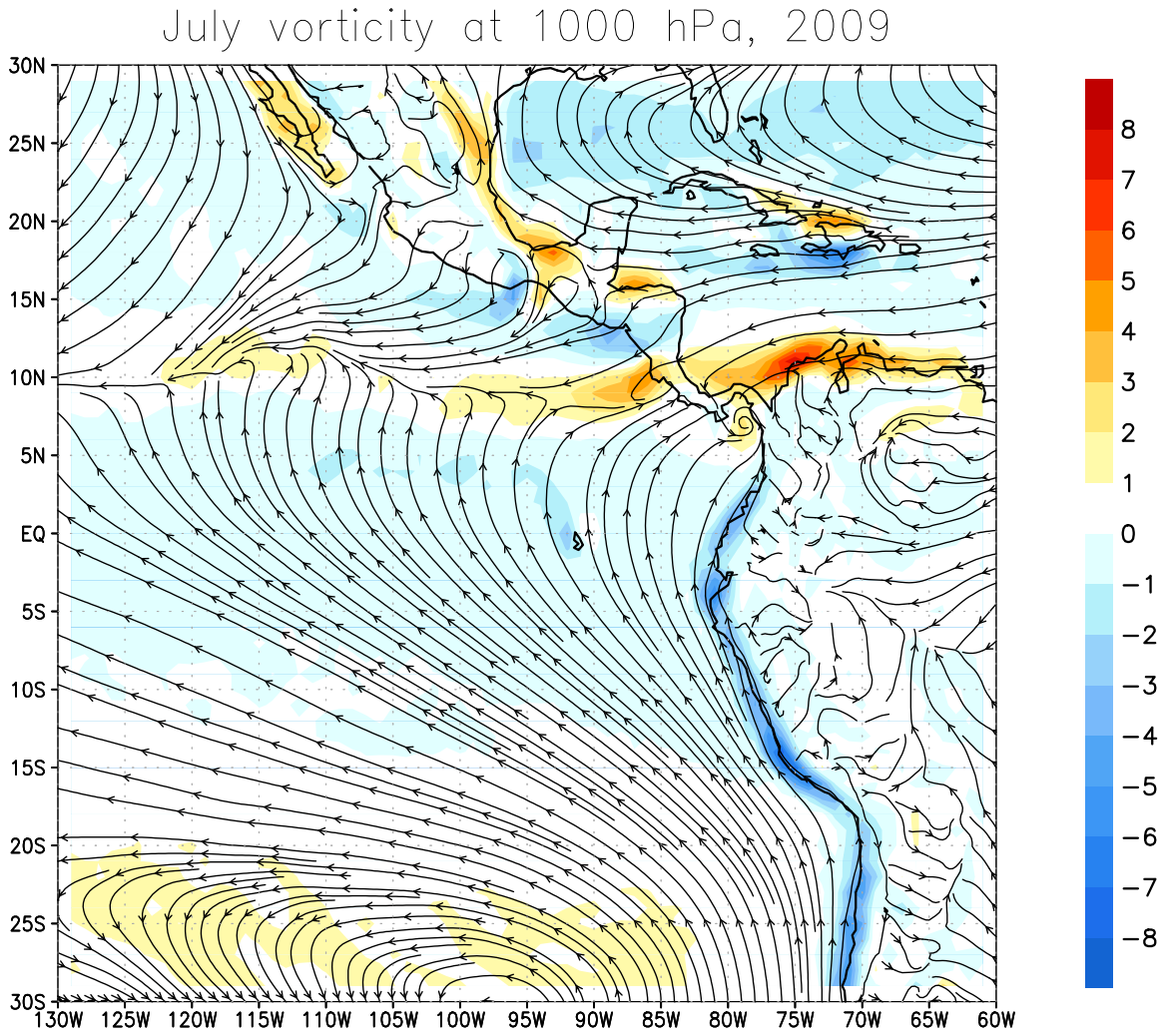

FIG. 2.8. July vorticity (scale at right in units of 10^{-5} s^{-1}) and streamlines at 1000 hPa.

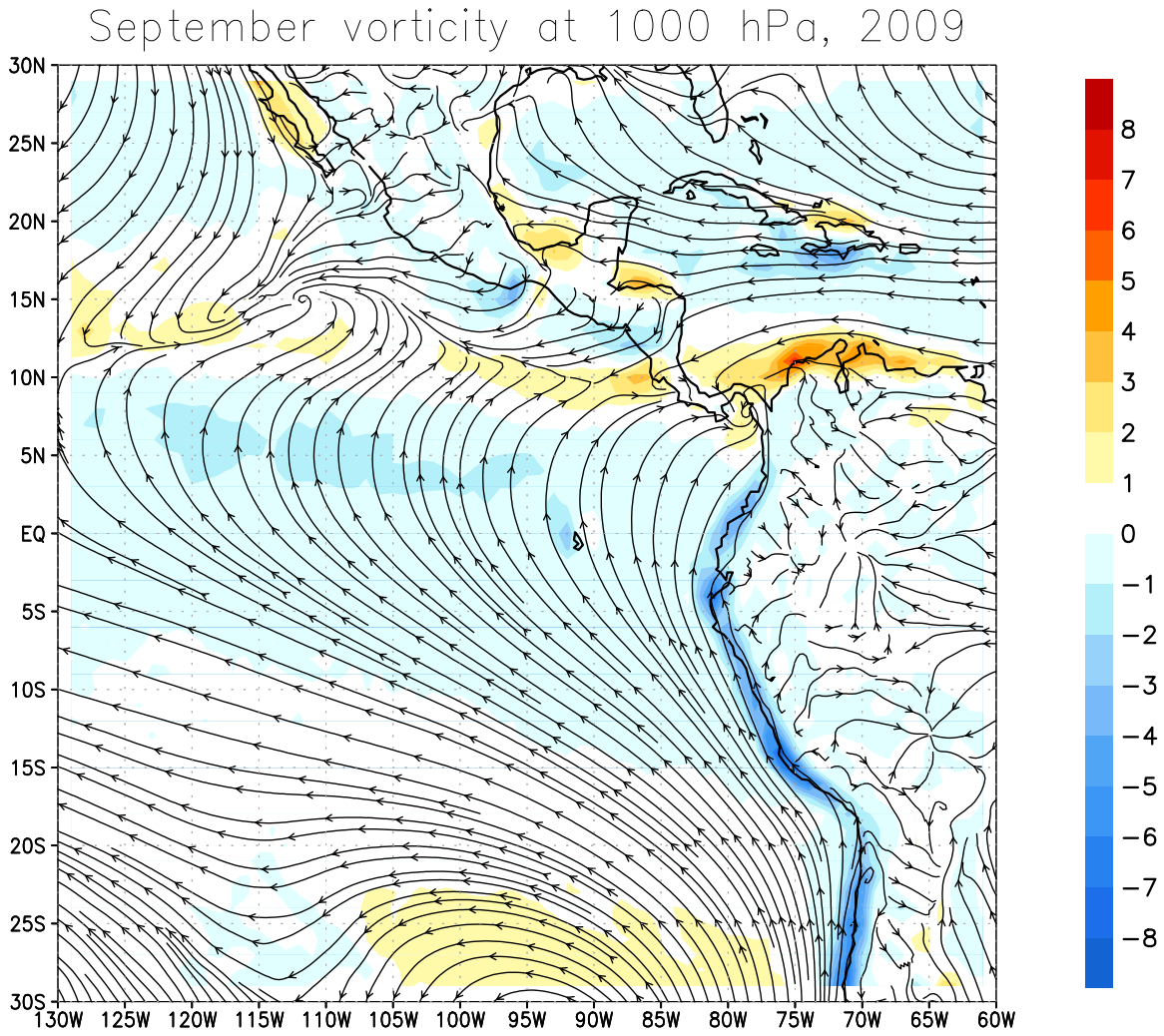

FIG. 2.9. September vorticity (scale at right in units of 10^{-5} s^{-1}) and streamlines at 1000 hPa.

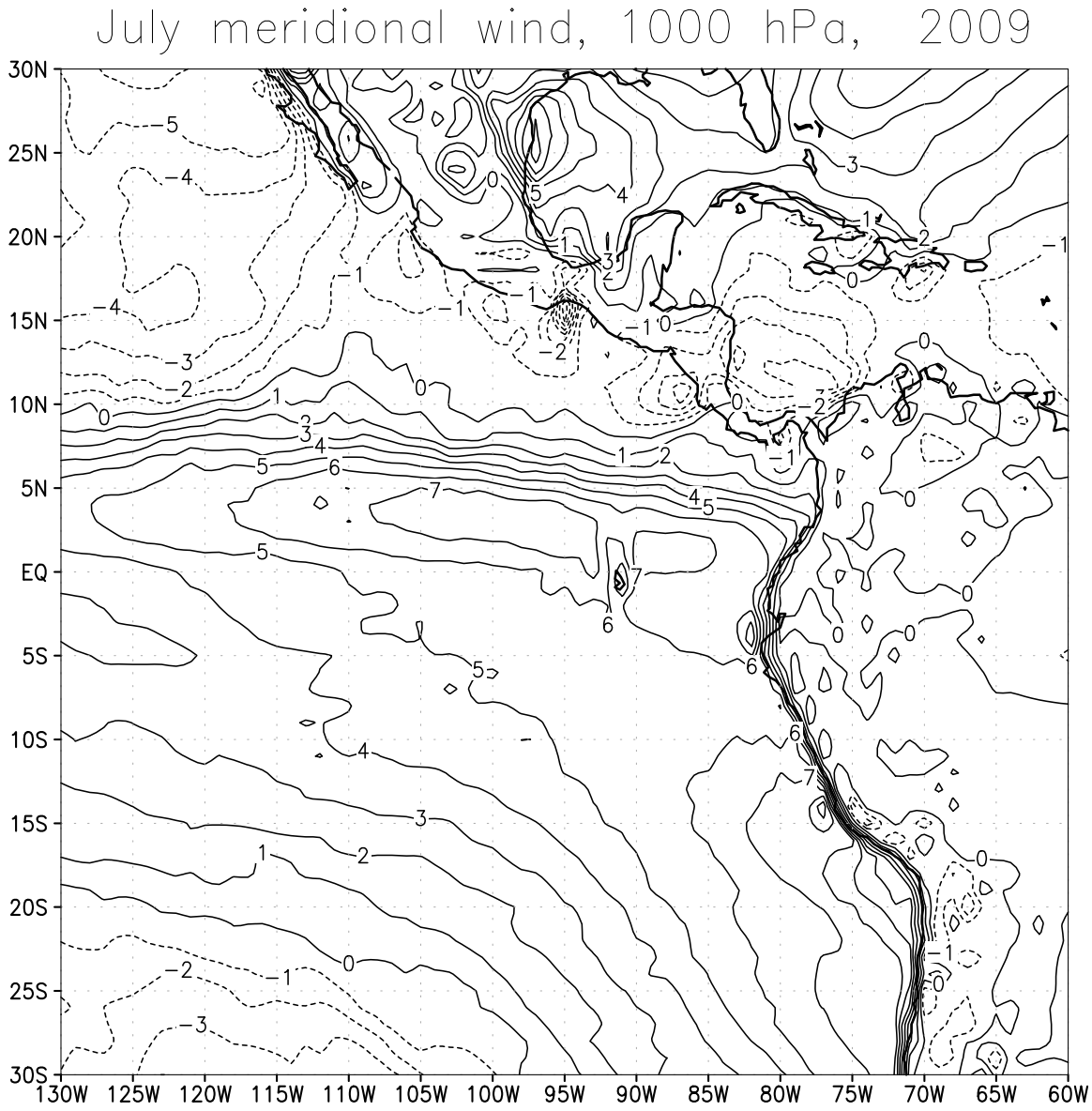

FIG. 2.10. July meridional wind (m s^{-1}) at 1000 hPa.

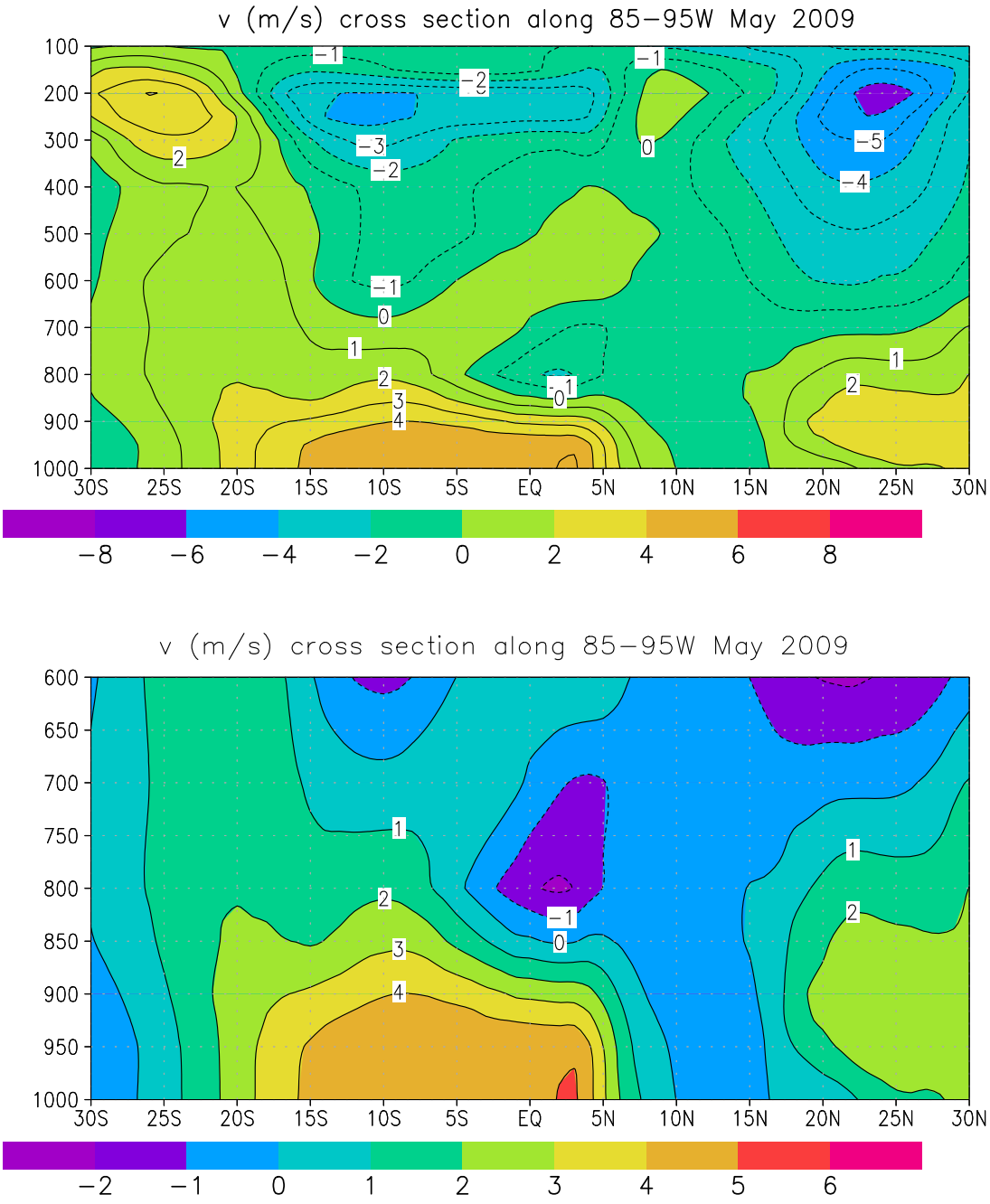

FIG. 2.11. May meridional wind (m s^{-1}) cross section, averaged over the longitude range 85°W–95°W.

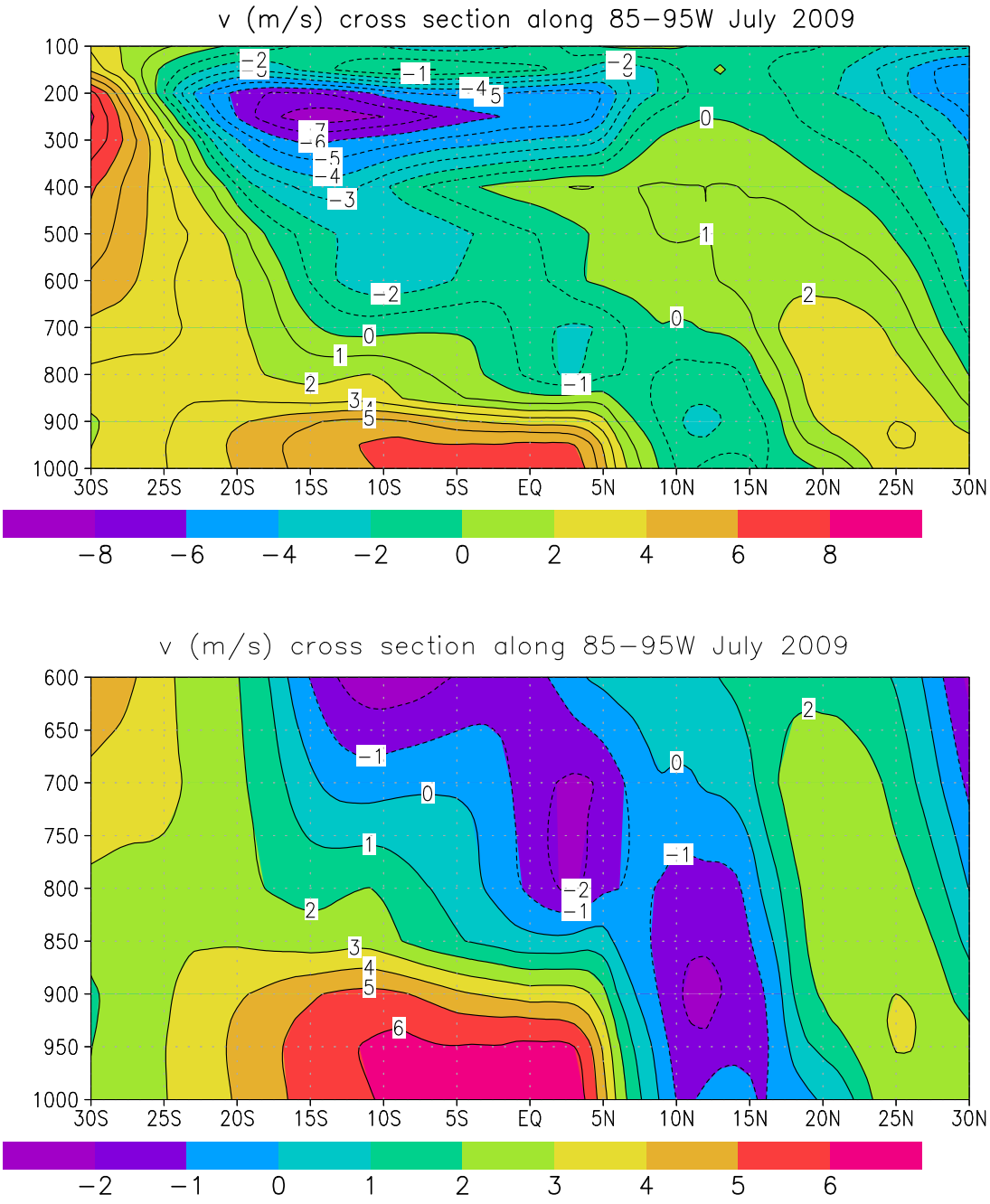

FIG. 2.12. July meridional wind (m s^{-1}) cross section, averaged over the longitude range 85°W–95°W.

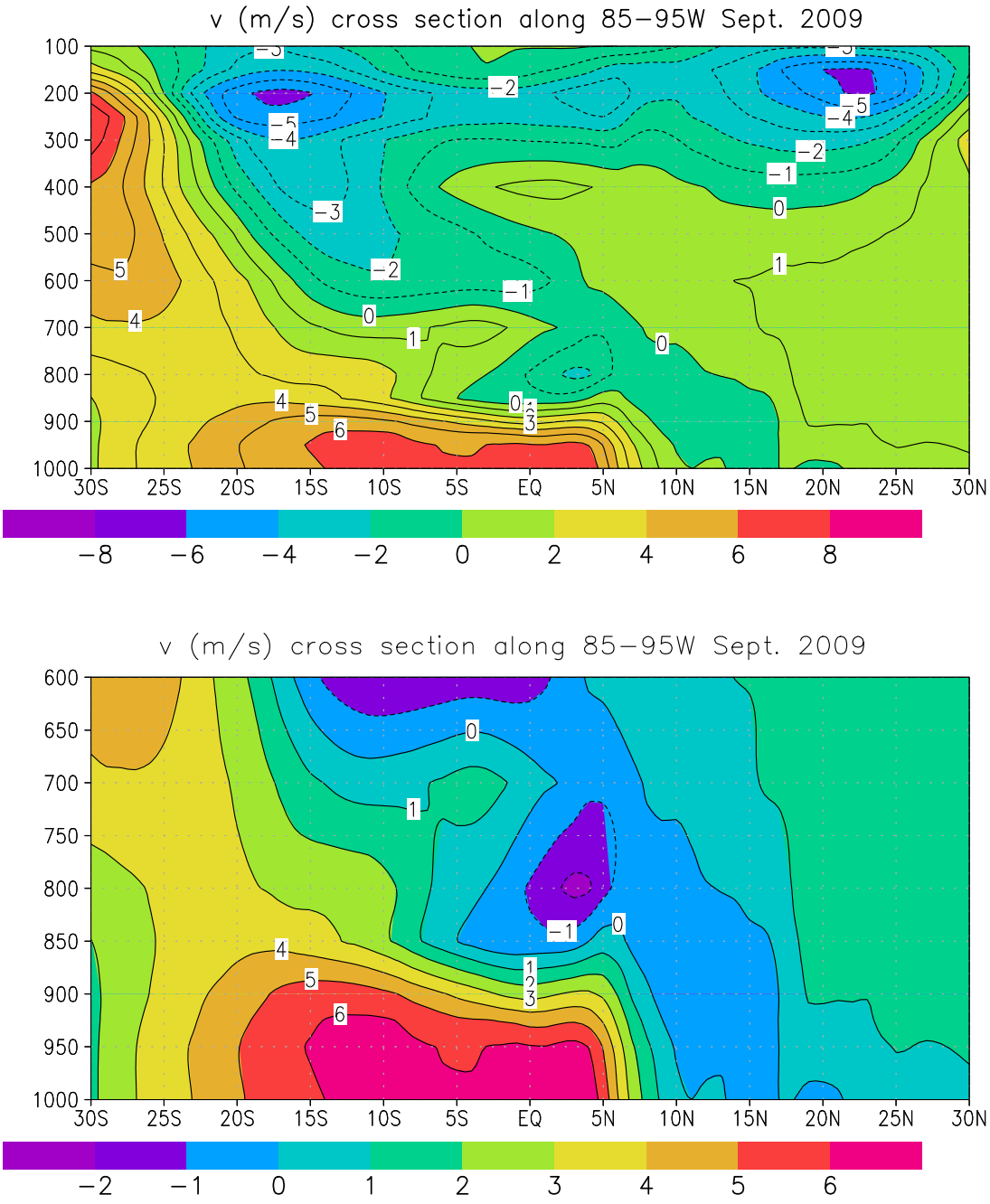

FIG. 2.13. September meridional wind (m s^{-1}) cross section, averaged over the longitude range 85°W–95°W.

CHAPTER 3

THE ZONALLY SYMMETRIC MODEL AND THE MERIDIONAL CIRCULATION EQUATION

In order to gain insight into the dynamics of the shallow and deep Hadley circulations, this chapter considers zonally symmetric motions in a stratified, compressible atmosphere on the equatorial β-plane. The limitation to zonally symmetric motions is a strong one, because it precludes simulation of Walker-type circulations. However, as we shall see, the zonally symmetric model can yield insight into situations such as the one depicted in Figure 3.1, which shows a typical, boreal summer 6.7 μm water vapor image of the eastern Pacific from the GOES West satellite. Under clear sky conditions, the 6.7 μm channel is sensitive to the vertically averaged humidity in the 200–500 hPa layer, so the dark blue areas on either side of the ITCZ indicate regions of low humidity in the upper troposphere, and hence regions of enhanced subsidence in the downward branches of the summer hemisphere and winter hemisphere Hadley and Walker cells. The complete explanation of atmospheric water vapor distributions can be quite complicated and involve several different physical processes, such as the stretching and folding processes associated with the Rossby wave pattern just east of Hawaii in Figure 3.1. For detailed discussions of tropical moisture distributions, including trajectory analysis and the concept of "time since last condensation," see Sun and Lindzen (1993), Soden and Fu (1995), Salathé and Hartmann (1997), Galewsky et al. (2005), Sherwood et al. (2006), Cau et al. (2007), and Schreck et al. (2013). In spite of the intricacies involved in comprehensive explanations of tropical water vapor distributions, it appears that, during much of the year, the explanation of the water vapor distribution in the eastern Pacific is simpler than in many other areas. An important part of the explanation lies in the dynamics of the Hadley cells, with the winter hemisphere Hadley cell having a large meridional extent and a large overturning mass flux. These are the aspects on which we shall focus.

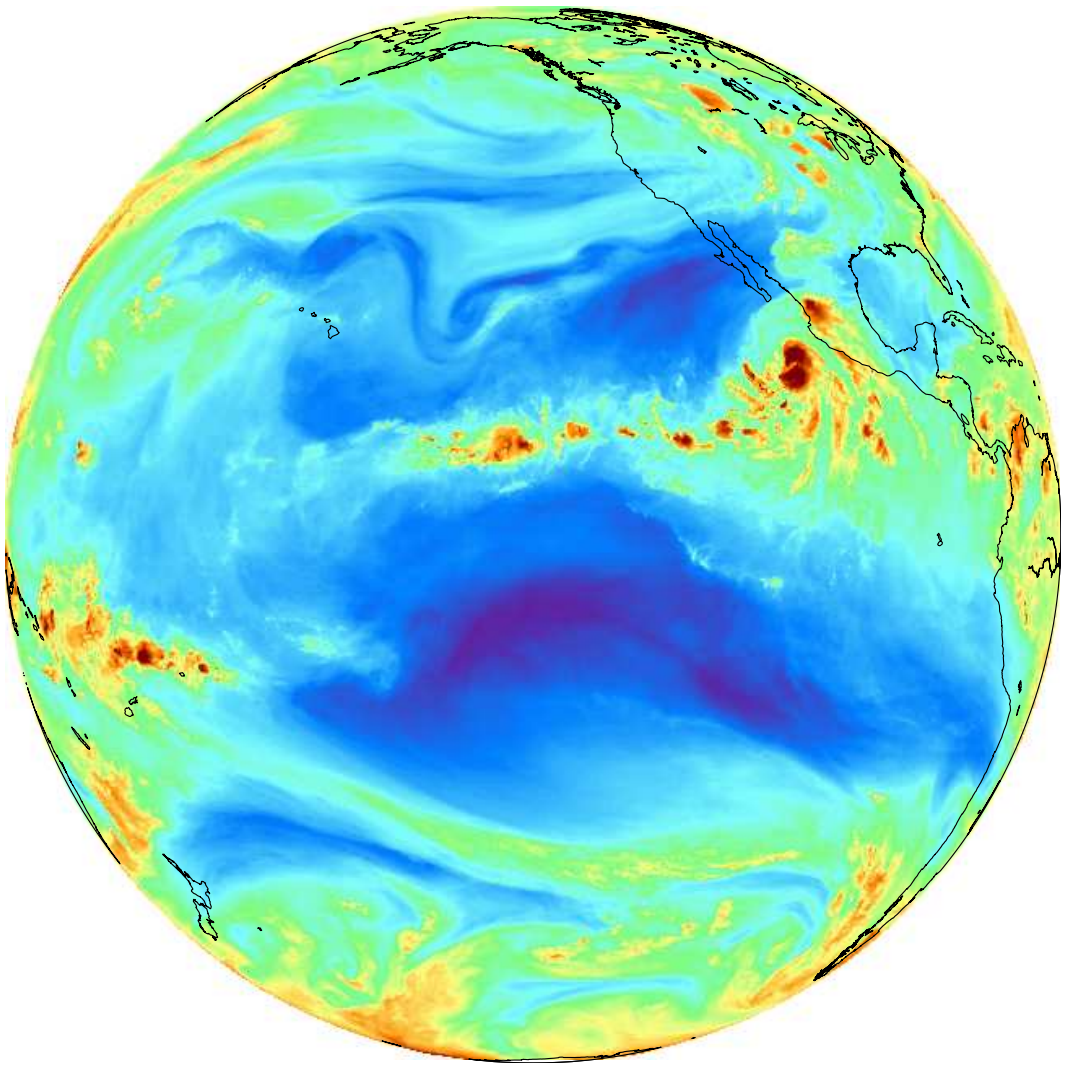

FIG. 3.1. The 06 UTC 25 June 2013 water vapor image (6.7 μm) from the GOES West satellite. The image is typical of the eastern Pacific during the boreal summer when the ITCZ is located near 10–15N. The dark blue areas on either side of the ITCZ indicate regions of low humidity in the upper troposphere, and hence regions of enhanced subsidence in the downward branches of the summer hemisphere and winter hemisphere Hadley cells. For a detailed discussion of 6.7 μm radiance-to-humidity transformation formulas, see Soden and Bretherton (1993, 1996) and Jackson and Bates (2001).

In the theory presented here, only the flow in the inviscid interior (i.e., above the 900 hPa isobaric surface) is explicitly considered. The effects of the frictional boundary layer will appear as the lower boundary condition on the inviscid interior. The derivation of the time dependent problem for the meridional circulation is given in section 3.1. The problem consists of a partial differential

equation in (y, z, t), with appropriate boundary and initial conditions. This problem can be solved by a variety of methods. The methods used here are analytical and provide important insights into the dynamics. As described in section 3.2, the first step involves application of a vertical transform that converts the original partial differential equation in (y, z, t) into a system of partial differential equations in (y, t). Two different analytical methods have been used here to solve the partial differential equations in (y, t). The first method, described in section 3.3, uses the Green's function approach (evanescent basis functions). This approach yields the most physical insight into the quasi-balanced meridional flow and the fundamental asymmetry between the summer hemisphere and winter hemisphere Hadley cells. The second method, described in section 3.4, uses the Hermite transform approach (oscillatory basis functions). This approach yields the most physical insight into the transient aspects of the flow and, in particular, how zonally symmetric inertia-gravity waves can be emitted due to pulsating convection in the ITCZ. The primary results obtained in this chapter are the mathematical statement of the meridional circulation problem, given below in (3.11)–(3.15), the analytical solution of the filtered version of this problem, given below in (3.42), (3.44), and (3.45), the analytical solution of the fully time dependent problem, given below in (3.56)–(3.58), and finally a second analytical representation of the filtered solution, given below in (3.60). An extensive discussion of these solutions is given in Chapter 4.

3.1. Derivation of the time dependent meridional circulation equation

As the vertical coordinate we use $z = H \ln(p_0/p)$, where $p_0 = 900$ hPa, $T_0 = 293$ K, and $H = RT_0/g = 8581$ m. We consider the case of weak zonal and meridional flow and weak baroclinicity, so that the $v(\partial u/\partial y)$ and $w(\partial u/\partial z)$ terms in the zonal momentum equation, the $v(\partial v/\partial y)$ and $w(\partial v/\partial z)$ terms in the meridional momentum equation, and the $v(\partial T/\partial y)$ term in the thermodynamic equation can be neglected. Under these assumptions, the governing equations

for zonally symmetric flow are

$$\frac{\partial u}{\partial t} - \beta y v = 0, \tag{3.1}$$

$$\frac{\partial v}{\partial t} + \beta y u + \frac{\partial \phi}{\partial y} = 0, \tag{3.2}$$

$$\frac{\partial \phi}{\partial z} = \frac{g}{T_0} T, \tag{3.3}$$

$$\frac{\partial v}{\partial y} + \frac{\partial w}{\partial z} - \frac{w}{H} = 0, \tag{3.4}$$

$$\frac{\partial T}{\partial t} + \frac{T_0}{g} N^2 w = \frac{Q(y,z)S(t)}{c_p}, \tag{3.5}$$

where u and v are the zonal and meridional components of velocity, w is the log-pressure vertical velocity, ϕ is the geopotential, $\beta = 2\Omega/a$ is the constant northward gradient of the Coriolis parameter, Ω and a are the Earth's rotation rate and radius, and $N^2(z) = (g/T_0)[(d\bar{T}/dz) + (\kappa \bar{T}/H)]$ is the square of the buoyancy frequency, which is computed from the specified mean temperature profile $\bar{T}(z)$. The diabatic heating has been assumed to have the spatial dependence $Q(y,z)$ and the time dependence

$$S(t) = 1 - (1 + \gamma t)e^{-\gamma t}, \tag{3.6}$$

with the constant γ specifying the sharpness of the switch-on function $S(t)$. Figure 3.2 displays four $S(t)$ curves for the particular values $\gamma^{-1} = 3,\ 6,\ 12,\ 24$ hours. Equations (3.1)–(3.5) constitute a system of five equations in the five unknowns u, v, w, ϕ, T, so long as the diabatic forcing is considered known. We have avoided use of a "parameterization" relating the diabatic heating to u, v, w, ϕ, T. Obviously, adding an equation in this manner has the serious disadvantage that our confidence that this additional equation is an accurate description of nature is much lower than our confidence that (3.1)–(3.5) are accurate descriptions of nature. Because of this, we attempt here to

see what physical insights can be gained about the meridional circulation without making use of such comparatively uncertain parameterization relations.

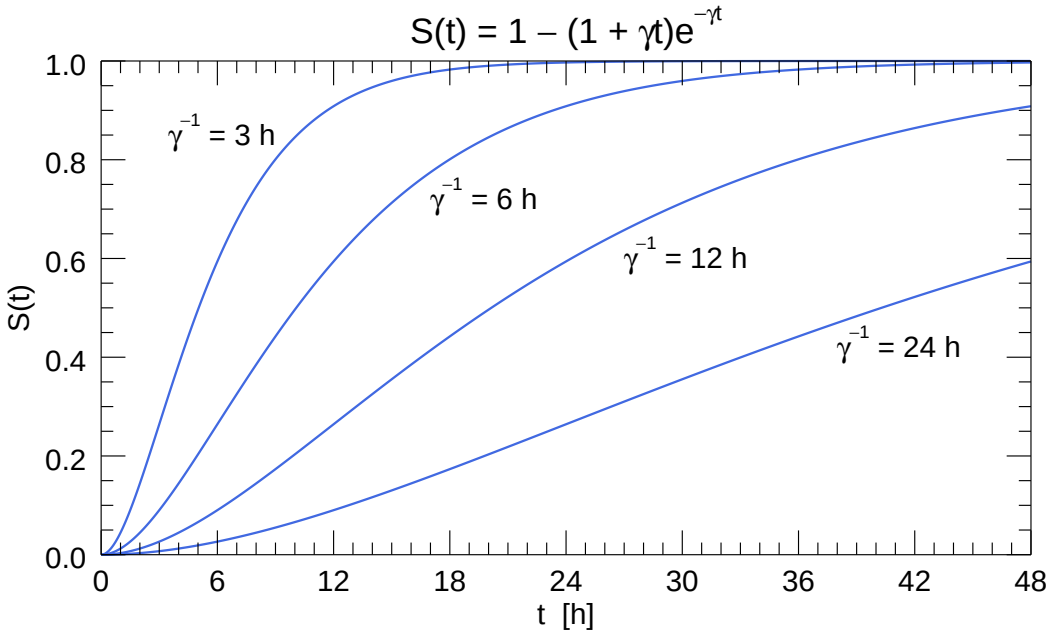

FIG. 3.2. Plots of the switch-on function $S(t)$ for the four choices $\gamma^{-1} = 3,\ 6,\ 12,\ 24$ hours. The "filtered solutions" discussed in sections 3.3 and 3.4 are valid for the "slow switch-on" cases, i.e., for large values of γ^{-1}.

We shall now combine (3.1)–(3.5) in such a way as to obtain a single equation for the stream-function of the meridional overturning circulation. We begin by multiplying the zonal wind equation (3.1) by βy and the thermodynamic equation (3.5) by (g/T_0), and then make use of the meridional wind equation (3.2) and the hydrostatic equation (3.3), thereby obtaining

$$\frac{\partial}{\partial y}\left(\frac{\partial \phi}{\partial t}\right) + \left(\frac{\partial^2}{\partial t^2} + \beta^2 y^2\right) v = 0, \tag{3.7}$$

$$\frac{\partial}{\partial z}\left(\frac{\partial \phi}{\partial t}\right) + N^2 w = \frac{gS(t)}{c_p T_0} Q. \tag{3.8}$$

The next step in the derivation is to eliminate $(\partial\phi/\partial t)$ between (3.7) and (3.8), thereby obtaining

$$N^2\frac{\partial w}{\partial y} - \left(\frac{\partial^2}{\partial t^2} + \beta^2 y^2\right)\frac{\partial v}{\partial z} = \frac{gS(t)}{c_p T_0}\frac{\partial Q}{\partial y}. \tag{3.9}$$

We can now regard (3.4) and (3.9) as a closed system in v and w. One way of proceeding with this system is to make use of (3.4) to express the meridional circulation (v, w) in terms of the streamfunction ψ by

$$e^{-z/H}v = -\frac{\partial \psi}{\partial z} \quad \text{and} \quad e^{-z/H}w = \frac{\partial \psi}{\partial y}, \tag{3.10}$$

and then to use (3.10) in (3.9) to obtain a single equation in ψ. This procedure yields the partial differential equation given below in (3.11). Assuming that $v \to 0$ as $y \to \pm\infty$ and that w vanishes at the top boundary ($z = z_T$), we obtain the boundary conditions given below in (3.12) and (3.13). Concerning the lower boundary condition, we assume that the actual vertical velocity (i.e., the physical height vertical velocity) is specified at the lower isobaric surface $z = 0$ (i.e., the top of the boundary layer). The appropriate linearized version of this lower boundary condition is $(\partial\phi/\partial t) + g(\partial\psi/\partial y) = gS(t)\mathcal{W}(y)$ at $z = 0$, where $\mathcal{W}(y)$ is the specified meridional distribution of the physical height vertical velocity at $z = 0$ and where we have assumed a time dependence $S(t)$ identical to that for the diabatic heating. From (3.7), we also have $(\partial/\partial y)(\partial\phi/\partial t) - (\partial^2/\partial t^2 + \beta^2 y^2)(\partial\psi/\partial z) = 0$ at $z = 0$. Eliminating $(\partial\phi/\partial t)$ from these last two relations, we obtain the lower boundary condition given below in (3.14). Concerning the initial conditions, we assume that the meridional circulation and its tendency both vanish at $t = 0$. In summary, the meridional circulation problem is

$$N^2 e^{z/H}\frac{\partial^2 \psi}{\partial y^2} + \left(\frac{\partial^2}{\partial t^2} + \beta^2 y^2\right)\frac{\partial}{\partial z}\left(e^{z/H}\frac{\partial \psi}{\partial z}\right) = \frac{gS(t)}{c_p T_0}\frac{\partial Q}{\partial y}, \tag{3.11}$$

with boundary conditions

$$\psi \to 0 \ \text{ as } \ y \to \pm\infty, \tag{3.12}$$

$$\psi = 0 \ \text{ at } \ z = z_T, \tag{3.13}$$

$$g\frac{\partial^2 \psi}{\partial y^2} + \left(\frac{\partial^2}{\partial t^2} + \beta^2 y^2\right)\frac{\partial \psi}{\partial z} = gS(t)\frac{\partial \mathcal{W}}{\partial y} \ \text{ at } \ z = 0, \tag{3.14}$$

and with initial conditions

$$\psi = 0 \ \text{ and } \ \frac{\partial \psi}{\partial t} = 0 \ \text{ at } \ t = 0. \tag{3.15}$$

Note that the diabatic forcing appears through the right hand side of the interior equation (3.11) while the frictional forcing appears through the right hand side of the lower boundary condition (3.14).

The meridional circulation problem (3.11)–(3.15) can be written in a slightly simpler form by defining $\hat{\psi}(y, z, t)$ and $\hat{Q}(y, z)$ as

$$\begin{aligned} \hat{\psi}(y, z, t) &= \psi(y, z, t)e^{z/2H}, \\ \hat{Q}(y, z) &= Q(y, z)e^{-z/2H}. \end{aligned} \tag{3.16}$$

Using (3.16) in (3.11)–(3.15) we can write the meridional circulation problem in the form

$$N^2\frac{\partial^2 \hat{\psi}}{\partial y^2} + \left(\frac{\partial^2}{\partial t^2} + \beta^2 y^2\right)\left(\frac{\partial^2 \hat{\psi}}{\partial z^2} - \frac{\hat{\psi}}{4H^2}\right) = \frac{gS(t)}{c_p T_0}\frac{\partial \hat{Q}}{\partial y}, \tag{3.17}$$

with boundary conditions

$$\hat{\psi} \to 0 \ \text{ as } \ y \to \pm\infty, \tag{3.18}$$

$$\hat{\psi} = 0 \ \text{ at } \ z = z_T, \tag{3.19}$$

$$g\frac{\partial^2\hat{\psi}}{\partial y^2}+\left(\frac{\partial^2}{\partial t^2}+\beta^2y^2\right)\left(\frac{\partial\hat{\psi}}{\partial z}-\frac{\hat{\psi}}{2H}\right)=gS(t)\frac{\partial\mathcal{W}}{\partial y}\ \text{ at }\ z=0, \tag{3.20}$$

and with initial conditions

$$\hat{\psi}=0\ \text{ and }\ \frac{\partial\hat{\psi}}{\partial t}=0\ \text{ at }\ t=0. \tag{3.21}$$

Note that (3.17) has a convenient form because of the absence of the $e^{z/H}$ factors that occur in (3.11). Because of the linearity of the problem and the associated superposition principle, we can separately calculate the responses to the two forcing effects and then add these to obtain the total response. This approach will be adopted in Chapter 4, where the response to diabatic forcing is discussed in section 4.1 and the response to Ekman pumping is discussed in section 4.2.

The meridional circulation problem (3.17)–(3.21) constitutes the primitive equation, equatorial β-plane version of the balanced problem first formulated by Eliassen (1952). Because of the simplifications introduced into (3.1) and (3.5), baroclinic terms (i.e., cross derivative terms) are absent from (3.17) and the inertial stability factor takes the simplified form β^2y^2. Baroclinic effects can be important in the overturning circulations of tropical cyclones, where they lead to substantial tilts in the eyewall updrafts (Schubert and McNoldy 2010). However, as discussed by Hack et al. (1989), baroclinic effects play only a minor role in the Hadley circulation.

It is interesting to note that the lower boundary condition (3.20) relates a combination of $\hat{\psi}$, $(\partial\hat{\psi}/\partial z)$, and $(\partial^2\hat{\psi}/\partial y^2)$ to the physical height vertical velocity $\mathcal{W}$ at the top of the boundary layer. The importance of formulating the lower boundary condition in this way has been emphasized by Haynes and Shepherd (1989), who have studied solutions of the spherical coordinate version of the meridional circulation equation. As we shall see in the next section, a consequence of the mathematical form of the lower boundary condition (3.20) is a slightly generalized version of the Sturm-Liouville eigenvalue-eigenfunction problem for the vertical structure functions, with

the eigenvalue appearing in both the second order ordinary differential equation and in the lower boundary condition, as will be seen below in (3.24)–(3.26).

3.2. VERTICAL TRANSFORM OF THE MERIDIONAL CIRCULATION EQUATION

We seek solutions of (3.17)–(3.21) via the vertical transform pair

$$\hat{\psi}_m(y,t) = \frac{1}{g}\int_0^{z_T} \hat{\psi}(y,z,t)\,\mathcal{Z}_m(z)\,N^2(z)\,dz + \hat{\psi}(y,0,t)\,\mathcal{Z}_m(0), \tag{3.22}$$

$$\hat{\psi}(y,z,t) = \sum_{m=0}^{\infty} \hat{\psi}_m(y,t)\,\mathcal{Z}_m(z). \tag{3.23}$$

In other words, the streamfunction $\hat{\psi}(y,z,t)$ is represented in terms of a series of vertical structure functions $\mathcal{Z}_m(z)$, with the coefficients $\hat{\psi}_m(y,t)$ given by (3.22). The reason for the last term in (3.22) arises from the lower boundary condition (3.20), as will become apparent shortly. The vertical structure functions $\mathcal{Z}_m(z)$ are solutions of the Sturm-Liouville eigenvalue problem

$$\frac{d^2\mathcal{Z}_m}{dz^2} - \frac{\mathcal{Z}_m}{4H^2} = -\frac{N^2\mathcal{Z}_m}{gh_m}, \tag{3.24}$$

$$\mathcal{Z}_m = 0 \ \text{ at } \ z = z_T, \tag{3.25}$$

$$\frac{d\mathcal{Z}_m}{dz} - \frac{\mathcal{Z}_m}{2H} = -\frac{\mathcal{Z}_m}{h_m} \ \text{ at } \ z = 0, \tag{3.26}$$

with eigenvalues (or equivalent depths) denoted by h_m. A discussion of the transform pair (3.22)–(3.23) is given in Appendix A, along with a proof that $h_m > 0$. The derivation of the solutions to the eigenvalue problem (3.24)–(3.26) for the special case of constant N^2 is given in Appendix B. For the case $N = 1.2 \times 10^{-2}$ and $z_T = 13$ km, the eigenvalues h_m are given in the second column of Table 3.1. The corresponding eigenfunctions $\mathcal{Z}_m(z)$ for $m = 0, 1, 2, 3, 4$ are displayed in Figure 3.3. In the remainder of the derivation in this section, we retain the generality of allowing

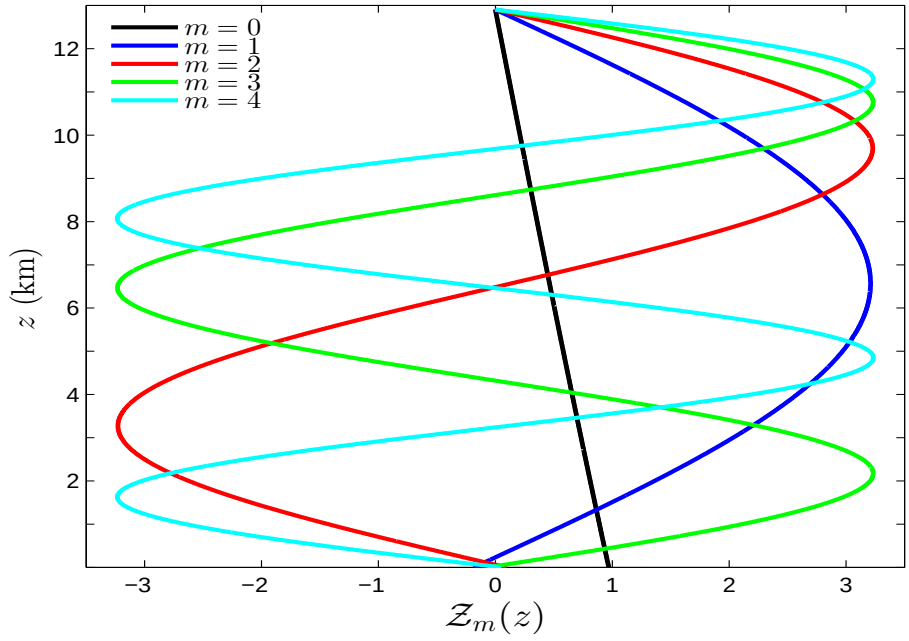

FIG. 3.3. Vertical structure functions $\mathcal{Z}_m(z)$ for the external mode $m = 0$ and the first four internal modes $m = 1, 2, 3, 4$. As discussed in Appendix B, these vertical structure functions are solutions of the Sturm-Liouville problem (3.24)–(3.26) with the constant buoyancy frequency $N = 1.2 \times 10^{-2}$ s^{-1} and $z_T = 13$ km.

the buoyancy frequency to be a function of z. However, for simplicity, the sample solutions shown in Chapter 4 are for the special case of constant N. An interesting possibility (not explored here) is that $N(z)$ could have reduced values just above the boundary layer, thereby simulating an "effective N" associated with shallow moist convection.

To take the vertical transform of (3.17), we first multiply it by $\mathcal{Z}_m(z)$ and integrate over z from 0 to z_T. The integral originating from the second order vertical derivative term in (3.17) is then integrated by parts twice to yield

$$\frac{\partial^2}{\partial y^2}\int_0^{z_T} \hat{\psi}(y,z,t)\mathcal{Z}_m(z)\,N^2(z)\,dz + \left(\frac{\partial^2}{\partial t^2}+\beta^2 y^2\right)\left[\mathcal{Z}_m(z)\frac{\partial\hat{\psi}(y,z,t)}{\partial z} - \hat{\psi}(y,z,t)\frac{d\mathcal{Z}_m(z)}{dz}\right]_0^{z_T}$$
$$+\left(\frac{\partial^2}{\partial t^2}+\beta^2 y^2\right)\int_0^{z_T}\hat{\psi}(y,z,t)\left(\frac{d^2\mathcal{Z}_m(z)}{dz^2}-\frac{\mathcal{Z}_m(z)}{4H^2}\right)dz = \frac{gS(t)}{c_pT_0}\frac{\partial}{\partial y}\int_0^{z_T}\hat{Q}(y,z)\mathcal{Z}_m(z)\,dz. \tag{3.27}$$

To simplify (3.27) we first use (3.24) in the third term and then use (3.19) and (3.25) to show that the upper boundary term vanishes. To evaluate the lower boundary term we first use (3.20) to eliminate $\partial\hat{\psi}/\partial z$ and then group the resulting $\partial^2\hat{\psi}/\partial y^2$ term with the first term of (3.27). Similarly, we use (3.26) to eliminate $d\mathcal{Z}_m/dz$ and then group the resulting $\mathcal{Z}_m/h_m$ term with the third term of (3.27). This procedure simplifies (3.27) to

$$\begin{aligned}
&\frac{\partial^2}{\partial y^2}\left\{\frac{1}{g}\int_0^{z_T}\hat{\psi}(y,z,t)\mathcal{Z}_m(z)\,N^2(z)\,dz+\hat{\psi}(y,0,t)\mathcal{Z}_m(0)\right\}\\
&-\frac{1}{gh_m}\left(\frac{\partial^2}{\partial t^2}+\beta^2y^2\right)\left\{\frac{1}{g}\int_0^{z_T}\hat{\psi}(y,z,t)\mathcal{Z}_m(z)\,N^2(z)\,dz+\hat{\psi}(y,0,t)\mathcal{Z}_m(0)\right\}\\
&=\frac{gS(t)}{c_pT_0}\frac{d}{dy}\left\{\int_0^{z_T}\hat{Q}(y,z)\mathcal{Z}_m(z)\,dz+\mathcal{W}(y)\mathcal{Z}_m(0)\right\}.
\end{aligned}\tag{3.28}$$

Then, with the use of (3.22), we obtain the meridional structure equation

$$\frac{\partial^2\hat{\psi}_m(y,t)}{\partial y^2}-\frac{1}{gh_m}\left(\frac{\partial^2\hat{\psi}_m(y,t)}{\partial t^2}+\beta^2y^2\hat{\psi}_m(y,t)\right)=S(t)\frac{\partial F_m(y)}{\partial y},\tag{3.29}$$

with boundary conditions

$$\hat{\psi}_m(y,t)\to 0 \text{ as } y\to\pm\infty,\tag{3.30}$$

and the initial conditions

$$\hat{\psi}_m(y,t)=0 \text{ and } \frac{\partial\hat{\psi}_m(y,t)}{\partial t}=0 \text{ at } t=0,\tag{3.31}$$

where the forcing term $F_m(y)$ on the right hand side of (3.29) is given by

$$F_m(y)=\int_0^{z_T}\frac{\hat{Q}(y,z)}{c_pT_0}\mathcal{Z}_m(z)\,dz+\mathcal{W}(y)\mathcal{Z}_m(0).\tag{3.32}$$

To summarize the results of this section, we have used the vertical transform pair (3.22)–(3.23) to reduce the partial differential equation (3.17) to the meridional structure equations (3.29), with a single forcing term (3.32) that combines the diabatic forcing term $\hat{Q}(y,z)$ with the frictional boundary layer forcing term $\mathcal{W}(y)$. After solution of the meridional structure equations (3.29) for $\hat{\psi}_m(y,t)$, the solution for $\hat{\psi}(y,z,t)$ can be recovered from (3.23).

3.3. Solution of the filtered meridional structure equations via Green's functions

In general, if the diabatic and frictional forcing vary slowly in time, the $\partial^2/\partial t^2$ term in (3.29) can be neglected. This is the special case we shall explore in this section. In this "slow forcing" case, the meridional circulation has no memory of the past forcing and is diagnostically determined by the current forcing only. Thus, the initial conditions (3.31) are no longer needed, and the meridional structure equation (3.29) simplifies to the diagnostic equation

$$\frac{d^2\hat{\psi}_m(y,t)}{dy^2} - \frac{y^2}{4b_m^4}\hat{\psi}_m(y,t) = S(t)\frac{dF_m(y)}{dy}, \tag{3.33}$$

with boundary conditions

$$\hat{\psi}_m(y,t) \to 0 \text{ as } y \to \pm\infty, \tag{3.34}$$

where the Rossby length b_m is given by

$$b_m = \left(\frac{gh_m}{4\beta^2}\right)^{1/4} = \epsilon_m^{-1/4}\frac{a}{\sqrt{2}}, \tag{3.35}$$

with Lamb's parameter defined by $\epsilon_m = 4\Omega^2 a^2/(gh_m)$. The spectra of equivalent depths h_m, Rossby lengths b_m, and Lamb's parameters ϵ_m for $m = 0, 1, 2, \ldots, 10$ are shown in Table 3.1.

TABLE 3.1. The spectra of equivalent depths h_m, gravity wave speeds $(gh_m)^{1/2}$ (with approximate values in parentheses), Rossby lengths $\bar{b}_m = [gh_m/\beta^2]^{1/4}$ (for Hermite functions) and $b_m = [gh_m/(4\beta^2)]^{1/4}$ (for parabolic cylinder functions), and Lamb's parameters $\epsilon_m = 4\Omega^2 a^2/(gh_m)$ for the eleven values of m listed in the left column. The values have been computed from (B.5) and (B.11) using $z_T = 12.91$ km, $g = 9.8$ m s^{-2}, $a = 6371$ km, $\Omega = 7.292 \times 10^{-5}$ s^{-1}, $N = 1.2 \times 10^{-2}$ s^{-1}, and $H = 8581$ m.

m	h_m (m)	$(gh_m)^{1/2}$ (m s^{-1})	$\bar{b}_m$ (km)	b_m (km)	ϵ_m
0	7074	263.3 (—)	3391	2398	12.44
1	226.7	47.14 (47.94)	1435	1015	388.4
2	60.55	24.36 (24.47)	1032	729.4	1454
3	27.26	16.35 (16.38)	845.0	597.5	3229
4	15.41	12.29 (12.30)	732.7	518.1	5715
5	9.882	9.841 (9.848)	655.6	463.6	8910
6	6.870	8.205 (8.210)	598.6	423.3	12815
7	5.051	7.036 (7.038)	554.4	392.0	17431
8	3.869	6.158 (6.159)	518.6	366.7	22757
9	3.058	5.474 (5.476)	489.0	345.8	28792
10	2.478	4.927 (4.928)	464.0	328.1	35538

We now solve (3.33) and (3.34) via the Green's functions $G_m(y, y')$, which are the solutions of the ordinary differential equations

$$\frac{d^2 G_m}{dy^2} - \frac{y^2}{4b_m^4} G_m = -\frac{1}{b_m^2}\delta\left(\frac{y - y'}{b_m}\right), \tag{3.36}$$

with the boundary conditions

$$G_m(y, y') \to 0 \text{ as } y \to \pm\infty, \tag{3.37}$$

where the Dirac delta function, $\delta((y - y')/b_m)$, vanishes for $y \neq y'$ and satisfies

$$\frac{1}{b_m}\int_{y'-}^{y'+} \delta\left(\frac{y - y'}{b_m}\right) dy = 1. \tag{3.38}$$

The Green's function $G_m(y, y')$ is constructed from the parabolic cylinder functions $D_\nu(x)$, which satisfy

$$\frac{d^2 D_\nu(y/b_m)}{dy^2} + \left(\nu + \frac{1}{2} - \frac{y^2}{4b_m^4}\right) D_\nu(y/b_m) = 0. \tag{3.39}$$

Note that the order $\nu = -1/2$ parabolic cylinder functions $D_{-1/2}(y/b_m)$ and $D_{-1/2}(-y/b_m)$ are solutions of the homogeneous version of (3.36). The functions $D_{-1/2}(x)$ and $D_{-1/2}(-x)$ for $-3 \leq x \leq 3$ are plotted in Figure 3.4. The half-integer order parabolic cylinder functions have also been used by Dias and Pauluis (2009) in their study of convectively coupled waves along the ITCZ.

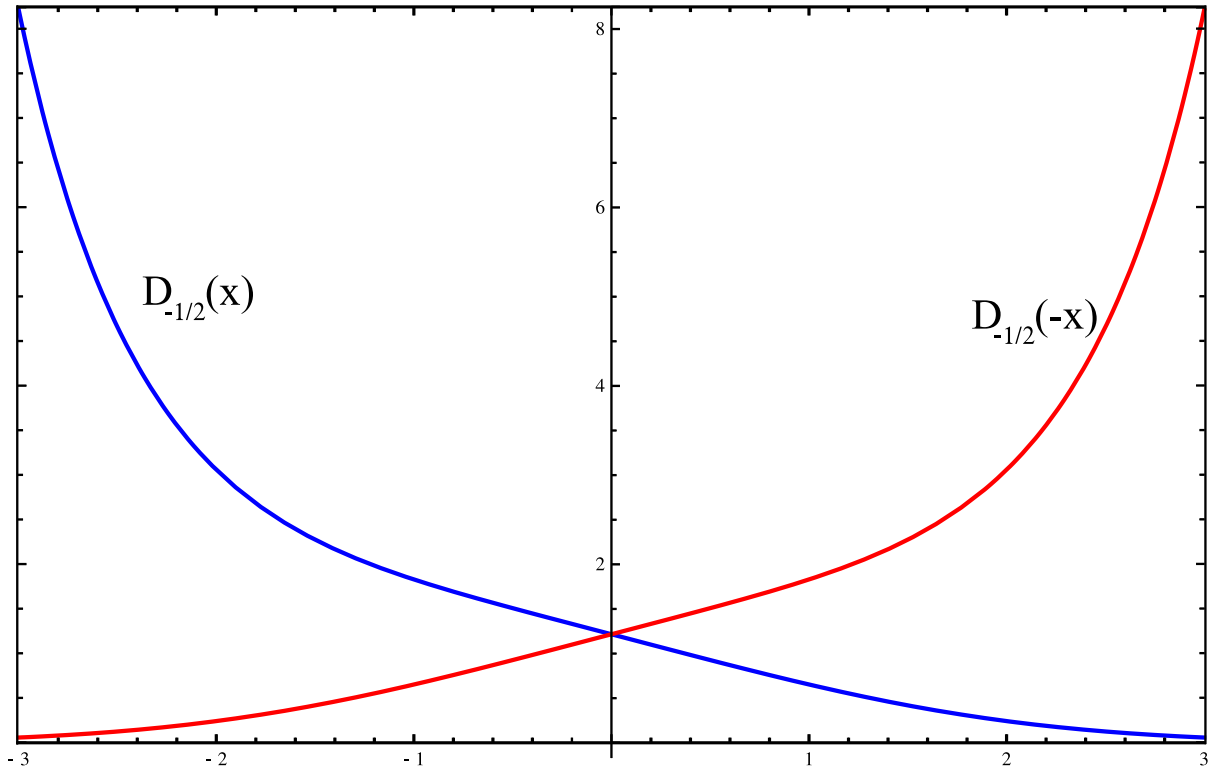

FIG. 3.4. Parabolic cylinder functions $D_{-1/2}(x)$ and $D_{-1/2}(-x)$ for $-3 \leq x \leq 3$. The function $D_{-1/2}(x)$, shown by the blue curve, satisfies the $y \to \infty$ boundary condition and is used to construct the Green's function $G_m(y, y')$ north of y'. Similarly, the function $D_{-1/2}(-x)$, shown by the red curve, satisfies the $y \to -\infty$ boundary condition and is used to construct the Green's function $G_m(y, y')$ south of y'. Because these two parabolic cylinder functions are solutions of the Weber differential equation (3.39) with $\nu = -1/2$, their second derivatives are zero at the equator but become large away from the equator. All the calculations presented here use the Mathematica function ParabolicCylinderD$[\nu, x]$.

Because of the lateral boundary conditions given in equation (3.34), only the solution $G_m(y, y') = \alpha_1 D_{-1/2}(-y/b_m)$ is valid for $-\infty \leq y \leq y'$ and only the solution $G_m(y, y') = \alpha_2 D_{-1/2}(y/b_m)$ is valid for $y' \leq y < \infty$, where α_1 and α_2 depend on y'. The two factors α_1 and α_2 are determined by requiring that $G_m(y, y')$ is continuous at $y = y'$ and that the jump in the first derivative satisfies

$$b_m \left[\frac{dG_m}{dy} \right]_{y'-}^{y'+} = -1, \tag{3.40}$$

which is obtained by integrating (3.36) across a narrow region surrounding $y = y'$, making use of the delta function property (3.38). The two algebraic equations for α_1 and α_2 can be solved with the aid of the Wronskian

$$D_{-1/2}(x) \frac{dD_{-1/2}(-x)}{dx} - D_{-1/2}(-x) \frac{dD_{-1/2}(x)}{dx} = \sqrt{2}. \tag{3.41}$$

This procedure results in

$$G_m(y, y') = \frac{1}{\sqrt{2}} \begin{cases} D_{-1/2}(y'/b_m) D_{-1/2}(-y/b_m) & \text{if } -\infty < y \leq y' \\ \\ D_{-1/2}(-y'/b_m) D_{-1/2}(y/b_m) & \text{if } y' \leq y < \infty. \end{cases} \tag{3.42}$$

Plots of $G_m(y, y')$ for $y' = -1500, -750, 0, 750, 1500$ km and $m = 0, 1, 2$ are shown in Figure 3.5. For larger values of m the jump in the derivative of $G_m(y, y')$ at $y = y'$ is larger and the Green's function is more confined to the region near $y = y'$.

To express the solution $\hat{\psi}_m(y, t)$ in terms of the Green's function, we multiply (3.33) by $G_m(y, y')$, multiply (3.36) by $\hat{\psi}_m(y, t)$, and then take the difference of the resulting equations

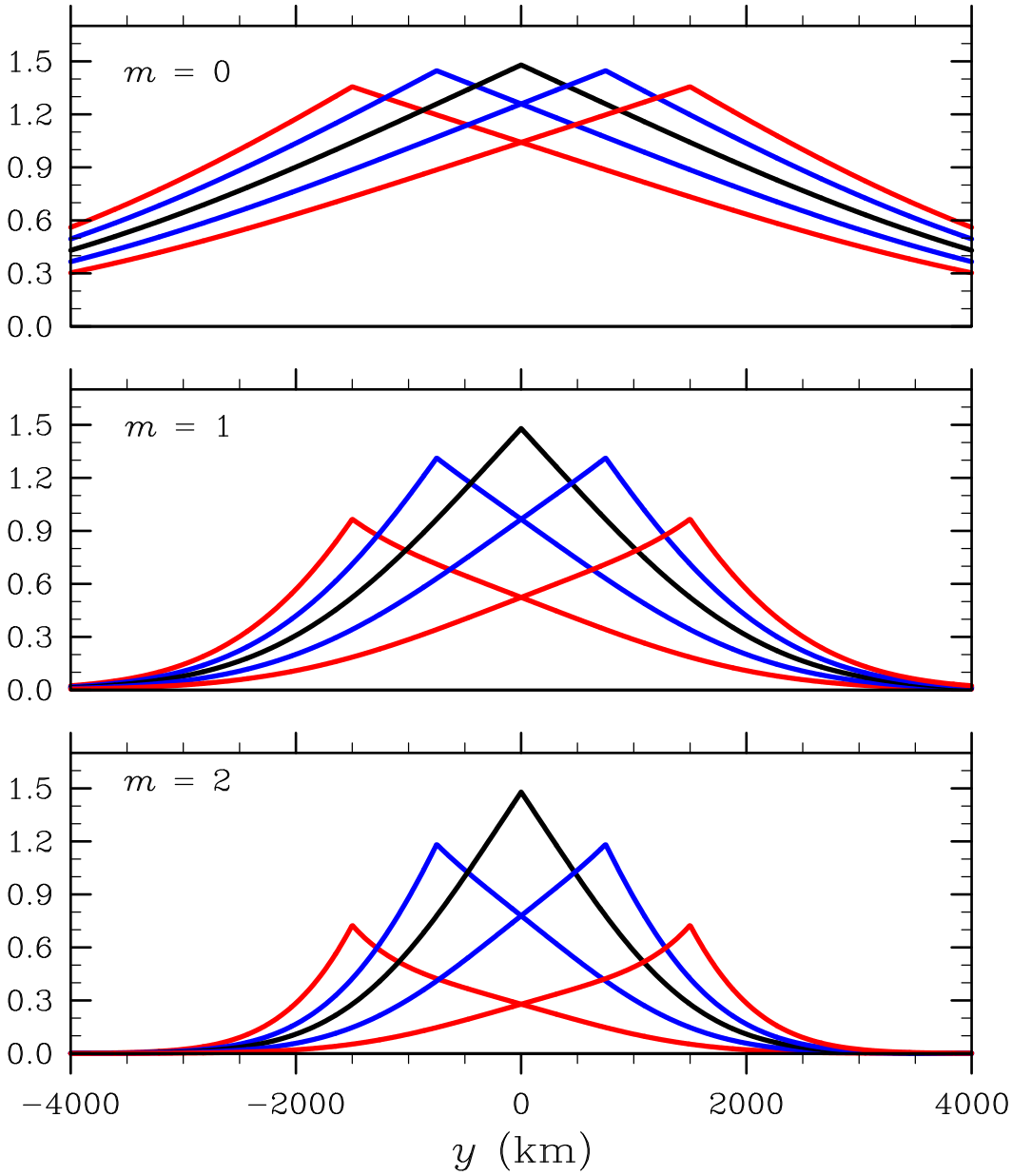

FIG. 3.5. Green's functions $G_m(y, y')$ for $y' = -1500, -750, 0, 750, 1500$ km and for $m = 0$ (top panel), $m = 1$ (middle panel), and $m = 2$ (bottom panel). These curves have been computed from (3.42). Note that, because of the b_m factors in (3.42), the Green's functions become more confined as the vertical mode index m becomes larger.

to obtain

$$\frac{\partial}{\partial y}\left(G_m(y,y')\frac{\partial\hat{\psi}_m(y,t)}{\partial y} - \hat{\psi}_m(y,t)\frac{\partial G_m(y,y')}{\partial y}\right) = S(t)\frac{dF_m(y)}{dy}G_m(y,y') + \hat{\psi}_m(y,t)\frac{1}{b_m^2}\delta\left(\frac{y-y'}{b_m}\right). \tag{3.43}$$

Integrating (3.43) over y, using the boundary conditions (3.34) and (3.37), using the delta function property (3.38), and finally using the Green's function symmetry property $G_m(y', y) = G_m(y, y')$, we obtain (3.45). In summary, the solution of the meridional circulation problem is

$$\psi(y, z, t) = e^{-z/2H} \sum_{m=0}^{\infty} \hat{\psi}_m(y, t)\, \mathcal{Z}_m(z), \tag{3.44}$$

where

$$\hat{\psi}_m(y, t) = -b_m S(t) \int_{-\infty}^{\infty} \frac{dF_m(y')}{dy'} G_m(y, y')\, dy'. \tag{3.45}$$

The solution for the streamfunction is obtained by first calculating $F_m(y')$ from (3.32), then calculating $\hat{\psi}_m(y, t)$ from (3.45), and finally calculating $\psi(y, z, t)$ from (3.44). Although this procedure generally involves the calculation of two integrals and an infinite sum, there are two interesting special cases where the formulas (3.44) and (3.45) are considerably simplified. These simple Hadley circulation models are discussed in Chapter 4.

The next section presents an alternative procedure for the solution of (3.29)–(3.30). This alternative procedure uses Hermite transforms instead of Green's functions and results in the filtered solution (3.61), which is simply a different mathematical representation of the solution (3.44)–(3.45). Readers wishing to now examine plots of the solution (3.44)–(3.45) should skip directly to Chapter 4. Section 3.4 can then be read later, especially by those wishing to explore the transient, inertia-gravity wave aspects of the problem.

3.4. Solution of the meridional structure equations via Hermite transforms

In section 3.3 we used Green's functions to solve the problem (3.29)–(3.31) for the case in which the diabatic and frictional forcing varies slowly in time, so that the $\partial^2/\partial t^2$ term in (3.29) could be neglected. The neglect of the $\partial^2/\partial t^2$ term results in a filtered model, i.e., a model that

does not simulate transient inertia-gravity waves. In this section we return to the complete problem (3.29)–(3.31), including the $\partial^2/\partial t^2$ term. We solve this complete problem using Hermite transforms. The Hermite transform pair for the streamfunction is

$$\hat{\psi}_m(y,t) = \sum_{n=0}^{\infty} \hat{\psi}_{mn}(t)\mathcal{H}_n(y/\bar{b}_m), \tag{3.46}$$

$$\hat{\psi}_{mn}(t) = \frac{1}{\bar{b}_m}\int_{-\infty}^{\infty} \hat{\psi}_m(y,t)\mathcal{H}_n(y/\bar{b}_m)dy, \tag{3.47}$$

where $\bar{b}_m = \sqrt{2}\, b_m$ (with numerical values given in the fourth column of Table 3.1)[1] and where the meridional structure functions $\mathcal{H}_n(y/\bar{b}_m)$ are related to the Hermite polynomials $H_n(y/\bar{b}_m)$ by

$$\mathcal{H}_n(y/\bar{b}_m) = \left(\pi^{\frac{1}{2}}2^n n!\right)^{-\frac{1}{2}} H_n(y/\bar{b}_m)e^{-\frac{1}{2}(y/\bar{b}_m)^2}. \tag{3.48}$$

Since the Hermite polynomials satisfy the recurrence relation $(y/\bar{b}_m)H_n(y/\bar{b}_m) = \frac{1}{2}H_{n+1}(y/\bar{b}_m) + nH_{n-1}(y/\bar{b}_m)$ and the derivative relation $dH_n(y/\bar{b}_m)/dy = (2n/\bar{b}_m)H_{n-1}(y/\bar{b}_m)$, it is easily shown that the meridional structure functions $\mathcal{H}_n(y/\bar{b}_m)$ satisfy the recurrence relation

$$(y/\bar{b}_m)\mathcal{H}_n(y/\bar{b}_m) = \left(\frac{n}{2}\right)^{\frac{1}{2}}\mathcal{H}_{n-1}(y/\bar{b}_m) + \left(\frac{n+1}{2}\right)^{\frac{1}{2}}\mathcal{H}_{n+1}(y/\bar{b}_m), \tag{3.49}$$

the derivative relation

$$\bar{b}_m\frac{d\mathcal{H}_n(y/\bar{b}_m)}{dy} = \left(\frac{n}{2}\right)^{\frac{1}{2}}\mathcal{H}_{n-1}(y/\bar{b}_m) - \left(\frac{n+1}{2}\right)^{\frac{1}{2}}\mathcal{H}_{n+1}(y/\bar{b}_m), \tag{3.50}$$

[1]Note that the b_m definition of Rossby length is convenient when working with parabolic cylinder functions (section 3.3), while the $\bar{b}_m$ definition of Rossby length is convenient when working with Hermite functions (section 3.4). This situation arises because the two functions (for integer n) are related by $\mathcal{H}_n(y/\bar{b}_m) = (\pi^{1/2}n!)^{-(1/2)}D_n(y/b_m)$. Another way of understanding this situation is to simply note that the parabolic cylinder functions are defined by the differential equation (3.39), which includes a factor $1/4$, while the Hermite functions are defined by the differential equation (3.51), which does not include this factor.

and the second order equation

$$\left(\frac{d^2}{dy^2} - \frac{y^2}{\bar{b}_m^4}\right)\mathcal{H}_n(y/\bar{b}_m) = -\left(\frac{2n+1}{\bar{b}_m^2}\right)\mathcal{H}_n(y/\bar{b}_m). \tag{3.51}$$

The first two meridional structure functions are $\mathcal{H}_0(y/\bar{b}_m) = \pi^{-\frac{1}{4}} e^{-\frac{1}{2}(y/\bar{b}_m)^2}$ and $\mathcal{H}_1(y/\bar{b}_m) = 2^{\frac{1}{2}}\pi^{-\frac{1}{4}}(y/\bar{b}_m)e^{-\frac{1}{2}(y/\bar{b}_m)^2}$, from which all succeeding structure functions can be computed using the recurrence relation (3.49). Computing $\mathcal{H}_n(y/\bar{b}_m)$ via its recurrence relation is much preferable to computing $H_n(y/\bar{b}_m)$ via its recurrence relation and then computing $\mathcal{H}_n(y/\bar{b}_m)$ by evaluation of the right hand side of (3.48), because the former method avoids explicit calculation of the factor $2^n n!$ for large n. The Hermite functions satisfy the orthonormality relation

$$\frac{1}{\bar{b}_m}\int_{-\infty}^{\infty} \mathcal{H}_n(y/\bar{b}_m)\mathcal{H}_{n'}(y/\bar{b}_m)\,dy = \begin{cases} 1 & n' = n, \\ 0 & n' \neq n. \end{cases} \tag{3.52}$$

Note that (3.47) can be obtained through multiplication of (3.46) by $\mathcal{H}_{n'}(y/\bar{b}_m)$, followed by integration over y and use of (3.52). Plots of $\mathcal{H}_n(y/\bar{b}_m)$ for $n = 0, 1, 2, 3, 4$ are shown in Figure 3.6.

To take the meridional transform of (3.29), we first multiply it by $\mathcal{H}_n(y/\bar{b}_m)$ and integrate over y. The integral originating from the second order y-derivative term in (3.29) is then integrated by parts twice, making use of the boundary conditions (3.30), to yield

$$\begin{aligned} &\int_{-\infty}^{\infty} \hat{\psi}_m(y,t)\left(\frac{d^2}{dy^2} - \frac{y^2}{\bar{b}_m^4}\right)\mathcal{H}_n(y/\bar{b}_m)\,dy \\ &- \frac{1}{gh_m}\frac{\partial^2}{\partial t^2}\int_{-\infty}^{\infty} \hat{\psi}_m(y,t)\mathcal{H}_n(y/\bar{b}_m)\,dy = S(t)\int_{-\infty}^{\infty} \frac{dF_m(y)}{dy}\mathcal{H}_n(y/\bar{b}_m)\,dy. \end{aligned} \tag{3.53}$$

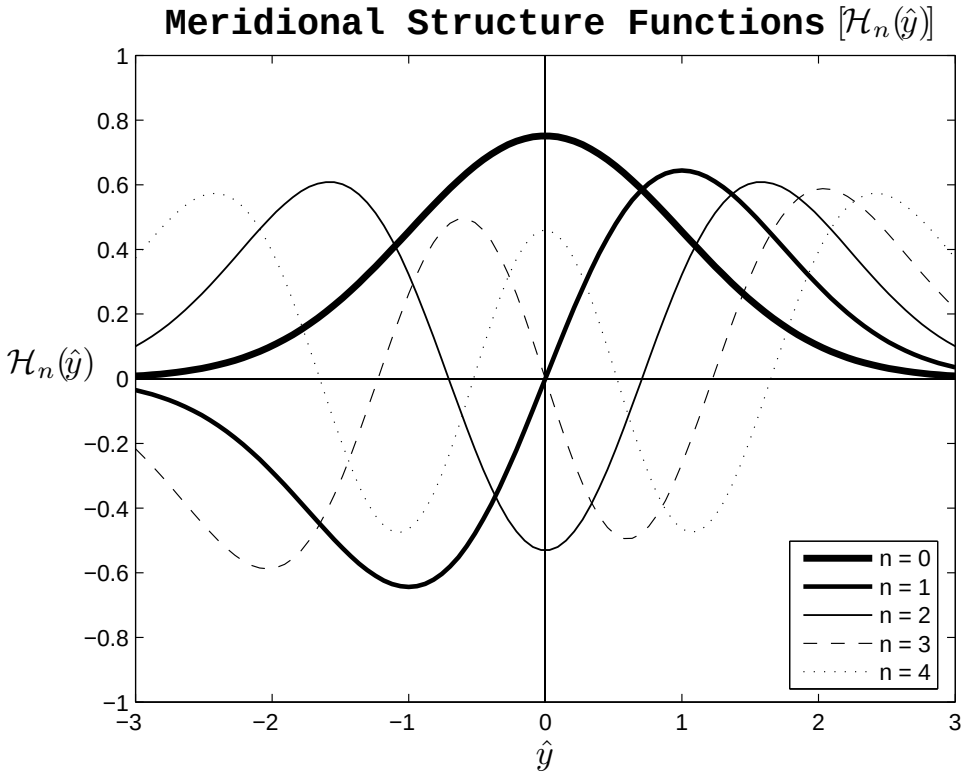

FIG. 3.6. The Hermite functions $\mathcal{H}_n(\hat{y})$ for $n = 0,\ 1,\ 2,\ 3,\ 4$. The dimensionless argument $\hat{y}$ is defined by $\hat{y} = y/\bar{b}_m$.

To simplify (3.53) we first use (3.51) in the integrand of the first integral. We then make use of (3.47) to simplify (3.53) to the second order ordinary differential equation

$$\frac{d^2\hat{\psi}_{mn}}{dt^2} + \nu_{mn}^2\hat{\psi}_{mn} = F_{mn}S(t), \tag{3.54}$$

with the initial conditions

$$\hat{\psi}_{mn} = 0 \ \text{ and } \ \frac{d\hat{\psi}_{mn}}{dt} = 0 \ \text{ at } \ t = 0, \tag{3.55}$$

where the inertia-gravity wave frequency ν_{mn} is given by

$$\nu_{mn} = \frac{c_m}{\bar{b}_m}\left(2n+1\right)^{1/2}, \tag{3.56}$$

and the forcing by

$$F_{mn} = -\frac{1}{\bar{b}_m} \int_{-\infty}^{\infty} \frac{dF_m(y)}{dy} \mathcal{H}_n(y/\bar{b}_m)\, dy. \tag{3.57}$$

The solution of (3.53) consists of the sum of the homogeneous solution and a particular solution. As is easily checked by direct substitution into (3.53), the solution satisfying the initial conditions (3.54) is

$$\begin{aligned} \hat{\psi}_{mn}(t) = \frac{F_{mn}}{\nu_{mn}^2} \Bigg\{ \left(\frac{\gamma^2(\nu_{mn}^2 - \gamma^2)}{(\nu_{mn}^2 + \gamma^2)^2} \right) \cos(\nu_{mn} t) - \left(\frac{2\gamma^3 \nu_{mn}}{(\nu_{mn}^2 + \gamma^2)^2} \right) \sin(\nu_{mn} t) \\ + 1 - \left(\frac{\nu_{mn}^2 + 3\gamma^2}{\nu_{mn}^2 + \gamma^2} + \gamma t \right) \left(\frac{\nu_{mn}^2 e^{-\gamma t}}{\nu_{mn}^2 + \gamma^2} \right) \Bigg\}. \end{aligned} \tag{3.58}$$

In summary, the solution of the original meridional circulation problem (3.11)–(3.15) is obtained by combining (3.16), (3.23), and (3.46) into

$$\psi(y, z, t) = e^{-z/2H} \sum_{m=0}^{\infty} \sum_{n=0}^{\infty} \hat{\psi}_{mn}(t)\, \mathcal{Z}_m(z) \mathcal{H}_n(y/\bar{b}_m), \tag{3.59}$$

where $\hat{\psi}_{mn}(t)$ is given by (3.57). The full transient solution for the streamfunction is obtained by first calculating F_{mn} from (3.56), then calculating $\hat{\psi}_{mn}(t)$ from (3.57), and finally calculating $\psi(y, z, t)$ from (3.58).

The spectral space solution (3.58) can be considered to be the sum of three parts, with the first part consisting of the oscillatory terms $\cos(\nu_{mn} t)$ and $\sin(\nu_{mn} t)$, the second part consisting of the steady state term F_{mn}/ν_{mn}^2, and the third part consisting of the decaying term with the $e^{-\gamma t}$ factor. For large times (i.e., $\gamma t \gg 1$), the third part is negligible and the oscillatory terms represent inertia-gravity waves that have propagated far from any confined region of forcing. Thus, no matter how slowly or rapidly the forcing terms are switched on, the final steady state Hadley overturning circulation (near the forcing region) is computed by using $\hat{\psi}_{mn}(t) = F_{mn}/\nu_{mn}^2$ in (3.59).

To understand the conditions for which the filtered solution is accurate at all times, consider the case in which $\gamma \ll \nu_{mn}$. Then, the solution (3.58) simplifies considerably since the coefficients of the $\cos(\nu_{mn}t)$ and $\sin(\nu_{mn}t)$ terms become very small compared to unity, while the second line in (3.58) approaches $S(t)$. Then, the spectral space solution (3.58) simplifies to

$$\hat{\psi}_{mn}(t) = \frac{F_{mn}S(t)}{\nu_{mn}^2}, \tag{3.60}$$

so that the physical space solution (3.59) becomes

$$\psi(y,z,t) = S(t)\, e^{-z/2H} \sum_{m=0}^{\infty}\sum_{n=0}^{\infty} \frac{F_{mn}}{\nu_{mn}^2} \mathcal{Z}_m(z)\mathcal{H}_n(y/\bar{b}_m). \tag{3.61}$$

Since the time dependence on the right hand side of (3.61) is $S(t)$, the $\psi(y,z,t)$ field develops in lockstep with the forcing, i.e., there is no time delay between the forcing and the response, no matter how far one is from the forcing. Since this represents "action at a distance," it should be regarded as a filtered approximation of the actual dynamics, valid only in the case of "slowly varying forcing." To better understand how slow the forcing needs to be, use (3.56) to rewrite the condition $\gamma \ll \nu_{mn}$ as

$$\gamma^{-1} \gg \frac{\bar{b}_m}{c_m(2n+1)^{1/2}} \approx \begin{cases} (3.6\,\mathrm{h})\,(2n+1)^{-1/2} & \text{if } \ m=0, \\ (8.5\,\mathrm{h})\,(2n+1)^{-1/2} & \text{if } \ m=1, \end{cases} \tag{3.62}$$

where, for illustration, the last approximate equality is for $m = 0$ (the external mode) and $m = 1$ (the first internal mode). Thus, for the external mode and the first internal mode, the $\gamma^{-1} = 24$ h curve in Figure 3.2 yields a forcing that is probably slow enough for the filtered approximation

to be reasonably accurate, but the $\gamma^{-1} = 3$ h curve yields a forcing that excites a non-negligible inertia-gravity wave response, especially for the higher internal modes.

It should be noted that the solution (3.41)–(3.42), obtained through the use of Green's functions, and the solution (3.60), obtained through the use of Hermite functions, are simply two different mathematical representations of the same physical solution. In other words, plots generated by evalution of (3.60) are identical to those generated by evalution of (3.41)–(3.42). In Chapter 4 we shall consider some sample solutions resulting from some particularly simple forcing distributions. For physical interpretation of the slowly changing, quasi-balanced meridional circulation, we shall find the Green's function representation more useful.

In concluding this chapter it is interesting to note that, as t becomes large, $S(t) \to 1$ and the forced divergent circulation (v, w) comes into steady state. However, as can be seen from (3.1) and (3.5), the zonal flow and the temperature continue to evolve. In fact, as we shall see in Chapter 4, they evolve in such a way that the associated potential vorticity field develops local extrema in the ITCZ, leading to a zonal flow that satisfies the Charney-Stern necessary condition for combined barotropic-baroclinic instability. Thus, one should not expect the evolving zonal flow to remain zonally symmetric for more than approximaely 10–15 days.

CHAPTER 4

DEEP AND SHALLOW OVERTURNING CIRCULATIONS

The analytical solutions of the meridional circulation equation are given by (3.44) with $\hat{\psi}_m(y,t)$ defined by (3.45) and the Green's function $G_m(y,y')$ defined by (3.42). In this chapter we first see how these formulas simplify for the case in which the diabatic and frictional forcing is localized in the ITCZ (section 4.1). Then, two special cases are considered. Section 4.2 considers the special case of deep diabatic heating, which forces a deep overturning circulation with an asymmetry between the summer hemisphere and winter hemisphere Hadley cells. This asymmetry maximizes when the ITCZ is centered approximately 1200 km off the equator. Section 4.3 considers the special case of frictional forcing through Ekman pumping in a narrow latitude band, which produces a shallow overturning circulation.

4.1. RESPONSE TO LOCALIZED ITCZ FORCING

Consider the response to a forcing that is localized within an ITCZ region, i.e., $F_m(y)$ is assumed to vanish everywhere except in the latitudinal range $y_1 < y < y_2$, where y_1 and y_2 are constants. Within this region the forcing is assumed to be independent of y, i.e.,

$$F_m(y) = \begin{cases} \mathcal{F}_m & \text{if } \; y_1 < y < y_2 \\ 0 & \text{otherwise,} \end{cases} \tag{4.1}$$

where the constants $\mathcal{F}_m$ specify the projection of the forcing onto the vertical modes. With these assumptions, the forcing terms $(\partial\hat{Q}/\partial y)$ and $(\partial\mathcal{W}/\partial y)$ on the right hand sides of (3.17) and (3.20) vanish everywhere except along the edges of the ITCZ, where they become infinitely large over an

infinitesimally thin layer. Thus, the circulation in the (y, z)-plane will consist of a counterclockwise turning gyre on the southern edge of the ITCZ and a clockwise turning gyre on the northern edge of the ITCZ.

Use of (4.1) in (3.45) now yields

$$\begin{aligned}\hat{\psi}_m(y,t) &= -S(t)\, b_m \left(G_m(y,y_1) \int_{y_1-}^{y_1+} \frac{dF_m(y')}{dy'}\, dy' + G_m(y,y_2) \int_{y_2-}^{y_2+} \frac{dF_m(y')}{dy'}\, dy' \right) \\ &= S(t)\, b_m \mathcal{F}_m \Big[G_m(y,y_2) - G_m(y,y_1) \Big],\end{aligned} \tag{4.2}$$

where the final line in (4.2) follows from the fact that the narrow integral across $y = y_1$ is $\mathcal{F}_m$, while the narrow integral across $y = y_2$ is $-\mathcal{F}_m$. Use of (4.2) in (3.44) yields the final solution

$$\psi(y,z,t) = S(t)\, e^{-z/2H} \sum_{m=0}^{\infty} b_m \mathcal{F}_m \Big[G_m(y,y_2) - G_m(y,y_1) \Big] \mathcal{Z}_m(z), \tag{4.3}$$

where the Green's functions $G_m(y, y_1)$ and $G_m(y, y_2)$ are given in (3.42).

4.2. PRODUCTION OF DEEP OVERTURNING CIRCULATIONS THROUGH DIABATIC FORCING

In this section we consider the case in which there is no frictional forcing and the diabatic forcing projects only onto the first internal mode, so that

$$\mathcal{F}_1 = \frac{g Q_{\max}}{c_p T_0 N^2}, \tag{4.4}$$

where $Q_{\max}$ is a constant. Then, the solution (4.3) can be written as

$$\psi(y,z,t) = \frac{gS(t)b_1 Q_{\max}}{c_p T_0 N^2 \sqrt{2}} e^{-z/2H} \mathcal{Z}_1(z)$$

$$\cdot \begin{cases} \Big[D_{-1/2}(y_2/b_1) - D_{-1/2}(y_1/b_1)\Big] D_{-1/2}(-y/b_1) & \text{if } -\infty < y \le y_1, \\ D_{-1/2}(y_2/b_1) D_{-1/2}(-y/b_1) - D_{-1/2}(-y_1/b_1) D_{-1/2}(y/b_1) & \text{if } y_1 \le y \le y_2, \\ \Big[D_{-1/2}(-y_2/b_1) - D_{-1/2}(-y_1/b_1)\Big] D_{-1/2}(y/b_1) & \text{if } y_2 \le y < \infty. \end{cases} \tag{4.5}$$

Figure 4.1 shows isolines of $\psi(y,z,t)$ computed from (4.5) using $S(t) = 1$ and the parameters $z_T = H\ln(9/2) \approx 12.91$ km, $Q_{\max}/c_p = 5$ K day^{-1}, $N = 1.2 \times 10^{-2}$ s^{-1}, and the four ITCZ positions $(y_1, y_2) = (0, 500), (500, 1000), (1000, 1500), (1500, 2000)$ km. Note that the asymmetry between the winter hemisphere Hadley cell and the summer hemisphere Hadley cell becomes larger as the ITCZ shifts off the equator due to the anisotropy of the inertial stability (Hack et al. 1989). Another way to view the meridional circulation is in terms of parcel trajectories, or more precisely, the projection of parcel trajectories onto the (y,z)-plane for our zonally symmetric flow with non-zero zonal winds. A collection of such three-day trajectories is shown in Fig. 4.2. From a rough count of the number of three-day segments needed for a complete cycle, one can estimate that the overturning time of the Hadley cells is on the order of several months, depending of course on how far poleward the cycle extends.

To understand how a localized ITCZ diabatic heating can cause nonzero $(\partial T/\partial t)$ over a large region outside the ITCZ, consider the thermodynamic equation $(\partial T/\partial t) + (T_0/g)N^2 w = (Q/c_p)$. As shown in Fig. 4.3, the $(\partial T/\partial t)$ field attributable to ITCZ diabatic heating tends to be small compared to Q/c_p, but to extend from approximately $30°$S to $30°$N. Outside the ITCZ, $(Q/c_p) = 0$ but there is weak subsidence over a large area, so that $(\partial T/\partial t)$ is small and positive over a large area. Within the ITCZ, (Q/c_p) peaks out at 5 K day^{-1} and $(T_0/g)N^2 w$ is positive, nearly reaching

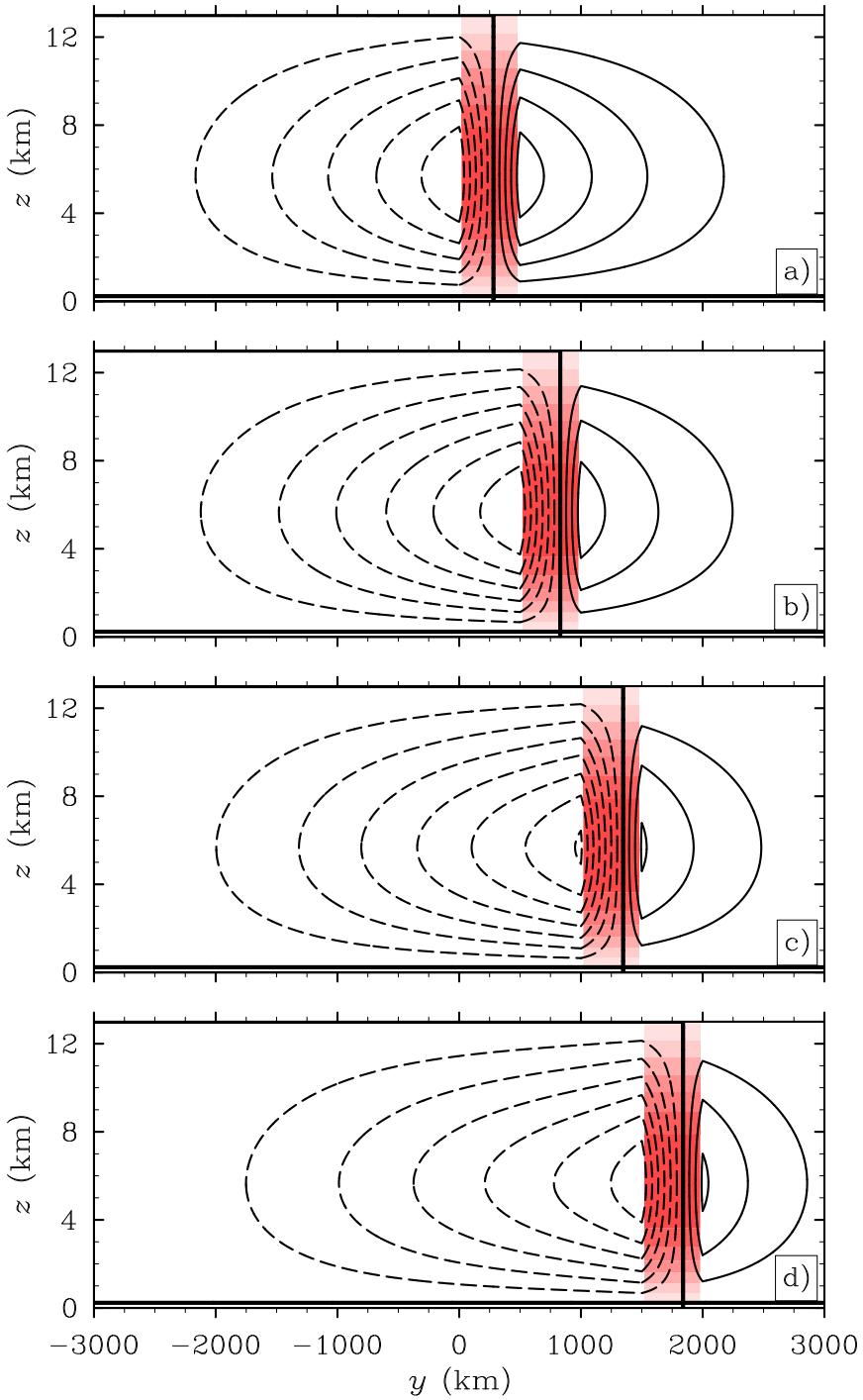

FIG. 4.1. Diabatic heating $e^{-z/H}Q(y,z)/c_p$, shown in color, and streamfunction $\psi(y,z)$, shown in the black contours with solid lines indicating $\psi > 0$ and dashed lines indicating $\psi < 0$, and with a contour interval of 400 m^2 s^{-1}. The maximum magnitude of $\psi(y,z)$ is 2852 m^2 s^{-1}. The $\psi(y,z)$ field has been computed from (4.5). For the $e^{-z/H}Q(y,z)/c_p$ field, the maximum value is 3.5 K day^{-1}, with changes in shading every 0.5 K day^{-1}. Four ITCZ positions are shown: (a) $(y_1, y_2) = (0, 500)$ km; (b) $(y_1, y_2) = (500, 1000)$ km; (c) $(y_1, y_2) = (1000, 1500)$ km; and (d) $(y_1, y_2) = (1500, 2000)$ km.

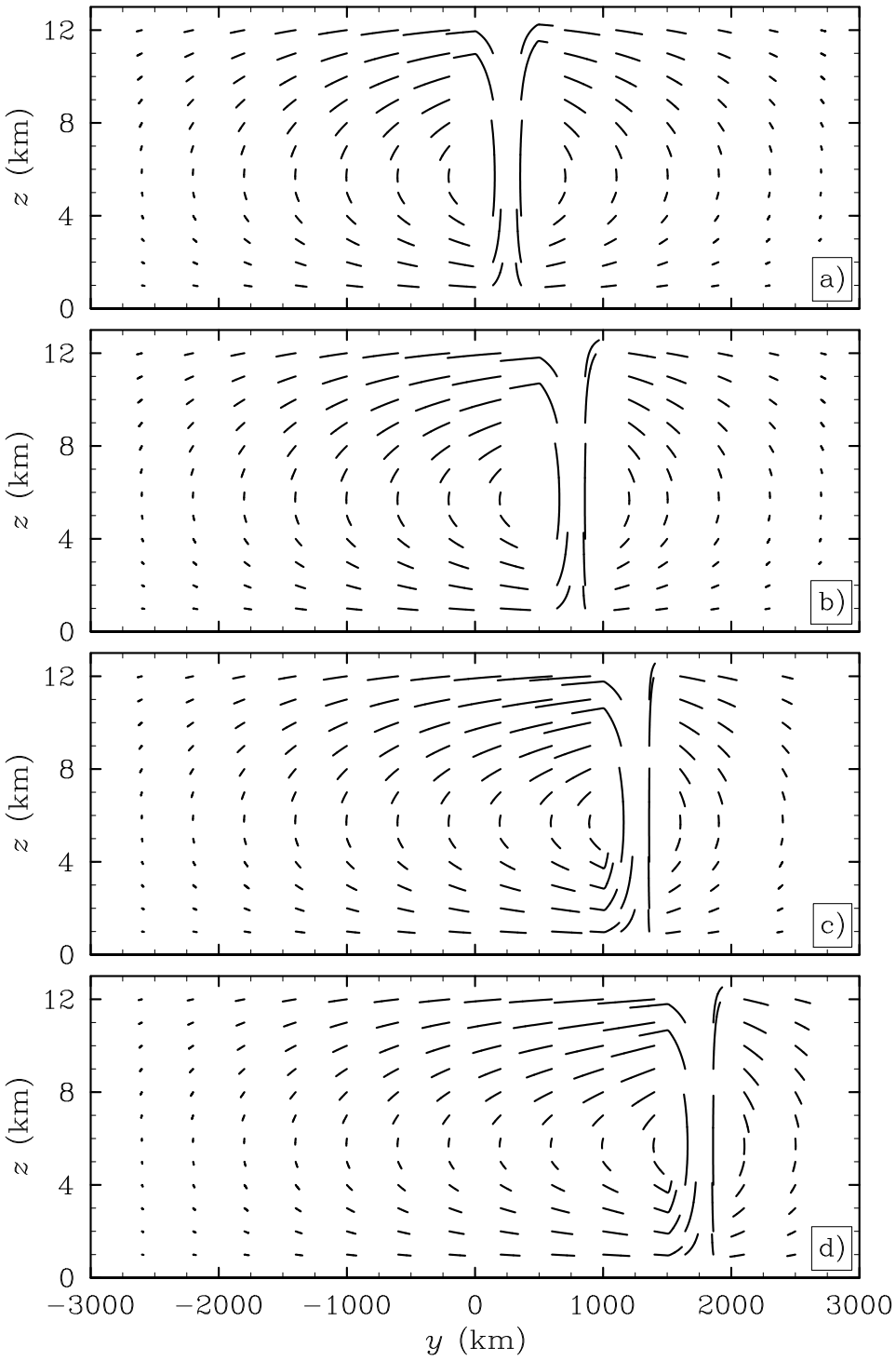

FIG. 4.2. Parcel trajectories during the first three days for the four deep diabatic heating positions (a) $(y_1, y_2) = (0, 500)$ km; (b) $(y_1, y_2) = (500, 1000)$ km; (c) $(y_1, y_2) = (1000, 1500)$ km; and (d) $(y_1, y_2) = (1500, 2000)$ km. Note: the grid changes for each ITCZ displacement.

this same peak value, so $(\partial T/\partial t)$ in the ITCZ is also small and positive. Note that both (Q/c_p) and $(T_0/g)N^2 w$ are discontinuous across the edges of the ITCZ, but, as seen in Fig. 4.3, their resulting tendency $(\partial T/\partial t)$ is continuous. It is interesting to note from Fig. 4.3 that, for ITCZ positions within 10° latitude of the equator, there is very little localization of the resulting temperature anomaly. However, when the (Q/c_p) field occurs near 20° latitude, as in Indian Monsoon convection, the temperature response becomes much more localized. Note that our assumption that $(Q/c_p) = 0$ outside the ITCZ neglects the effects of radiative cooling, but that radiative cooling, if uniform in y, would not appear in the right hand side of (3.7).

It is interesting to note that the determination of the tendencies T_t and u_t, shown in Figs. 4.3 and 4.4, highlight the difference between the present approach to ITCZ and Hadley dynamics and the steady-state approach used by Schneider (1977), Held and Hou (1980), and Lindzen and Hou (1988). The present approach makes no steady-state assumption and focuses attention on the solution of the meridional circulation equation, which does not explicitly appear in the steady state models.

As listed in Table 3.1, the equatorial Rossby length for the first internal mode is $b_1 = 1025$ km. In general terms, the Rossby length (in f-plane theory) is often considered as the approximate distance over which compensating subsidence will occur due to a point source of diabatic heating (Eliassen 1952). However, this simple f-plane argument does not capture the basic anisotropy of tropical dynamics, which is easily seen in the y-structure of the Green's functions shown in Fig. 3.5. For example, in Fig. 4.1d the compensating subsidence extends approximately 1000 km north of the ITCZ, but extends approximately 3500 km south of the ITCZ. This anisotropy is reflected in all the fields shown in Figs. 4.1–4.4 and is a fundamental aspect of the Green's functions shown in Fig. 3.5.

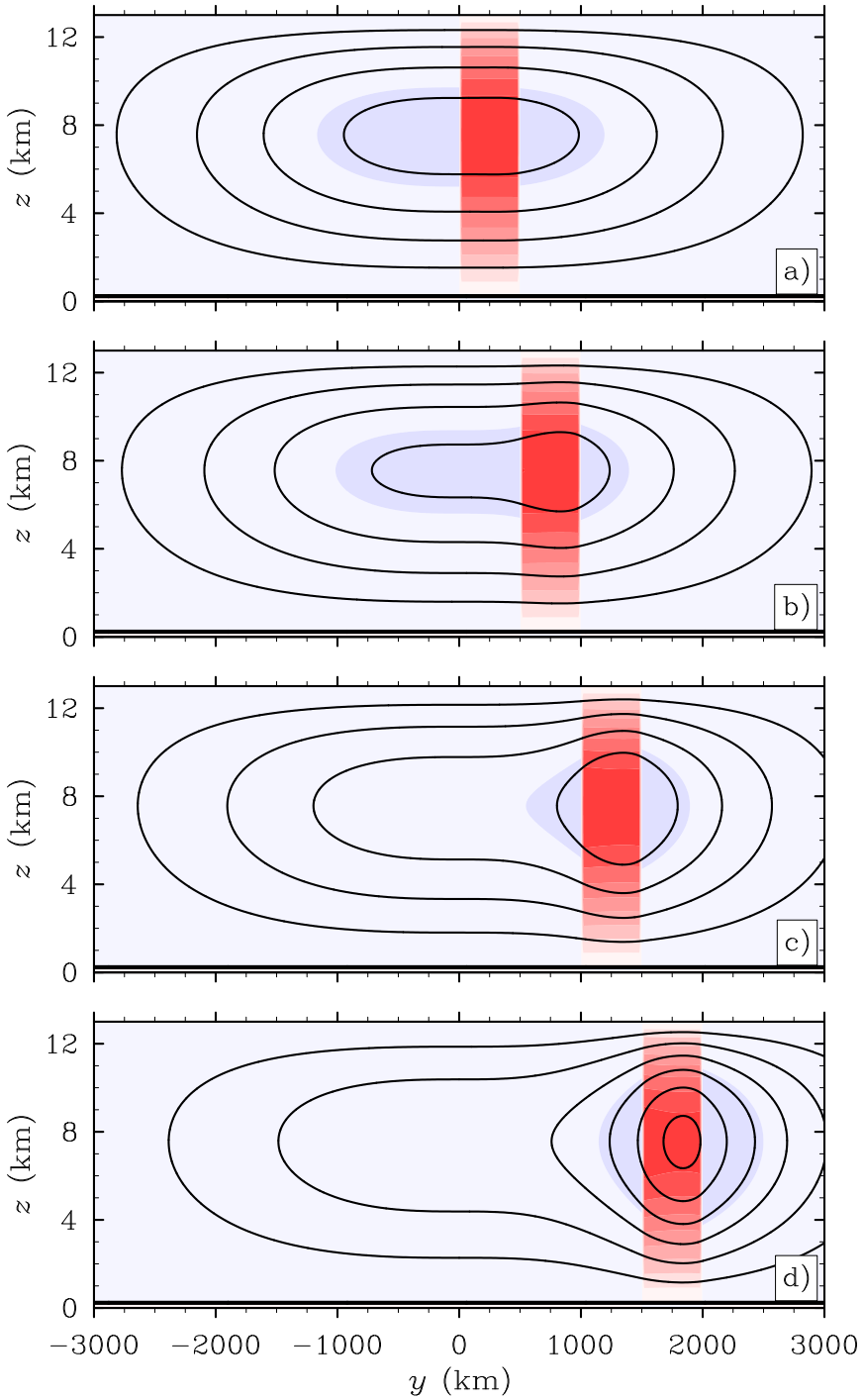

FIG. 4.3. Log-pressure vertical velocity $w(y, z)$, shown in color, and temperature tendency $T_t(y, z)$, shown in the black contours with the zero contour indicated in bold. For w, blue indicates subsidence and red indicates ascent, with changes in the shading every 0.2 cm s^{-1}. Note that the w field is discontinuous at the edges of the ITCZ, but the $T_t(y, z)$ field is continuous. The contour interval for $T_t(y, z)$ is 0.2 K day^{-1}. The maximum magnitude of $w(y, z)$ is 1.801 cm s^{-1}. Four ITCZ positions are shown: (a) $(y_1, y_2) = (0, 500)$ km; (b) $(y_1, y_2) = (500, 1000)$ km; (c) $(y_1, y_2) = (1000, 1500)$ km; and (d) $(y_1, y_2) = (1500, 2000)$ km.

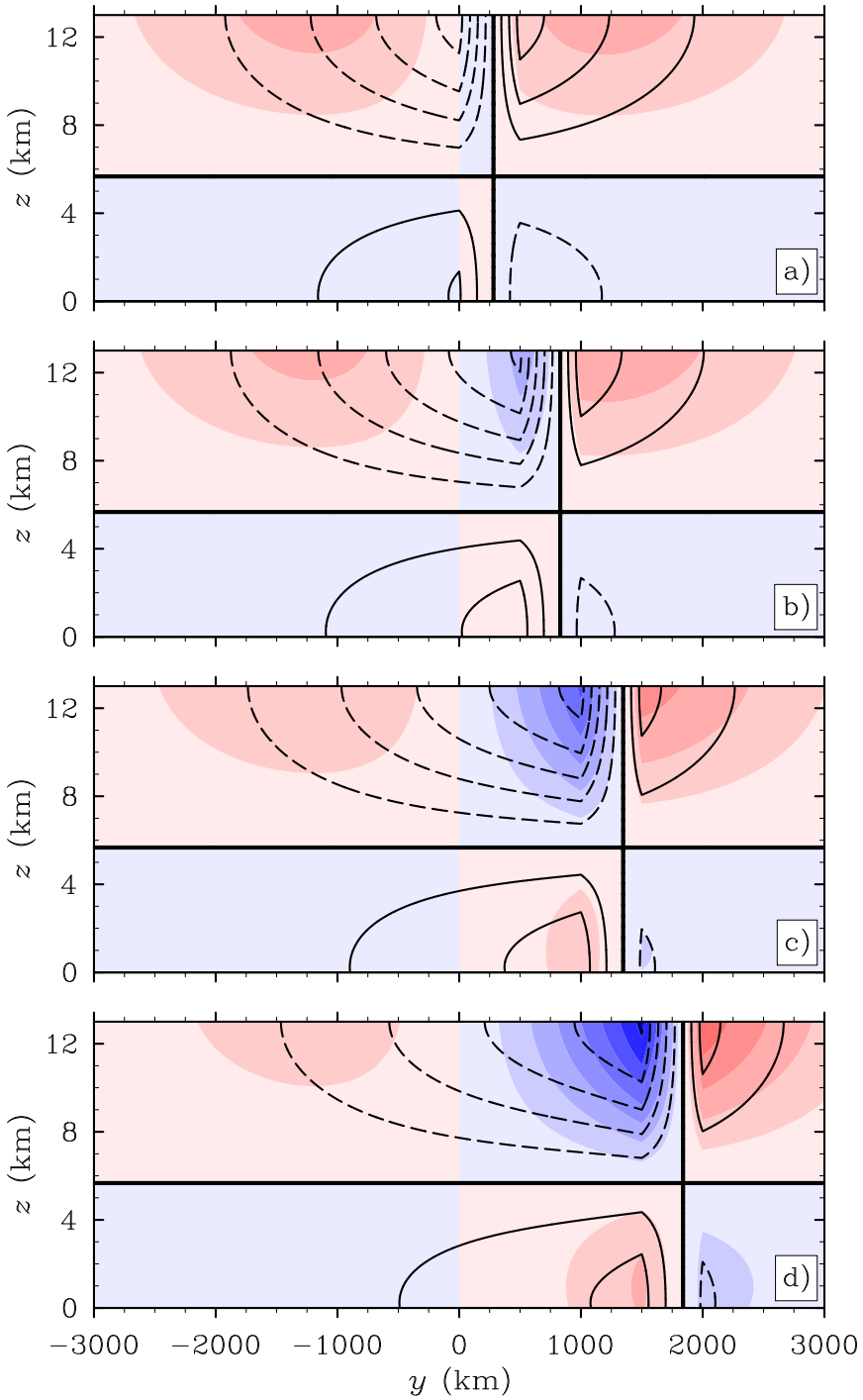

FIG. 4.4. Zonal wind tendency $u_t(y, z)$, shown in color, and meridional wind $v(y, z)$, shown in the black contours with solid lines indicating southerlies ($v > 0$), dashed lines indicating northerlies ($v < 0$), and bold lines indicating the zero contours. The contour interval for $v(y, z)$ is 0.4 m s^{-1} per day. The maximum magnitude for $v(y, z)$ is 2.141 m s^{-1}. For $u_t(y, z)$, blue indicates $u_t > 0$ and red indicates $u_t < 0$, with changes in the shading every 1.0 m s^{-1} day^{-1}. The maximum magnitude for $u_t(y, z)$ is 7.403 m s^{-1} per day. Four ITCZ positions are shown: (a) $(y_1, y_2) = (0, 500)$ km; (b) $(y_1, y_2) = (500, 1000)$ km; (c) $(y_1, y_2) = (1000, 1500)$ km; and (d) $(y_1, y_2) = (1500, 2000)$ km.

A simple formula for the partition of the total ITCZ mass flux between the summer hemisphere and winter hemisphere Hadley cells can be found by considering the case $(y_2 - y_1) \to 0$, but $Q_{\max} \to \infty$ in such a way that the product $Q_{\max}(y_2 - y_1) = \text{constant}$. Equation (4.5) then reduces to

$$\psi(y,z,t) = \frac{gS(t)\,Q_{\max}(y_2-y_1)}{c_p T_0 N^2\sqrt{2}} e^{-z/2H}\mathcal{Z}_1(z) \cdot \begin{cases} D'_{-1/2}(y_1/b_1)D_{-1/2}(-y/b_1) & \text{if } -\infty < y < y_1 \\ D'_{-1/2}(-y_1/b_1)D_{-1/2}(y/b_1) & \text{if } y_1 < y < \infty, \end{cases} \tag{4.6}$$

where $D'_{-1/2}(x) = dD_{-1/2}(x)/dx$ and $D'_{-1/2}(-x) = dD_{-1/2}(-x)/dx$. Note that $\psi(y,z,t)$ is discontinuous at $y = y_1$ and that the total upward mass flux at z is given by

$$\psi(y_1+,z,t) - \psi(y_1-,z,t) = \frac{gS(t)\,Q_{\max}(y_2-y_1)}{c_p T_0 N^2} e^{-z/2H}\mathcal{Z}_1(z). \tag{4.7}$$

Then, the fractional mass fluxes in the two cells are

$$\begin{pmatrix}\text{Fractional Mass}\\ \text{Flux of Summer}\\ \text{Hemisphere Cell}\end{pmatrix} = \frac{\psi(y_1+,z,t)}{\psi(y_1+,z,t) - \psi(y_1-,z,t)} = \frac{1}{\sqrt{2}} D'_{-1/2}(-y_1/b_1)D_{-1/2}(y_1/b_1), \tag{4.8}$$

$$\begin{pmatrix}\text{Fractional Mass}\\ \text{Flux of Winter}\\ \text{Hemisphere Cell}\end{pmatrix} = \frac{-\psi(y_1-,z,t)}{\psi(y_1+,z,t) - \psi(y_1-,z,t)} = -\frac{1}{\sqrt{2}} D'_{-1/2}(y_1/b_1)D_{-1/2}(-y_1/b_1). \tag{4.9}$$

Plots of (4.8) and (4.9), as a function of the ITCZ position y_1, are shown in Fig. 4.5. The maximum asymmetry between the winter and summer hemisphere cells occurs when the ITCZ is located 1200–1300 km off the equator, in which case the winter cell carries approximately twice the mass

flux of the summer cell. Such cross-equatorial mass transports lead to large cross-equatorial moisture and energy transports, as discussed by Kang et al. (2008). This theoretical result, obtained using the equatorial β-plane approximation, is in close agreement with the numerical calculations of Hack et al. (1989), who used the exact spherical coordinate version of the Eliassen meridional circulation equation.

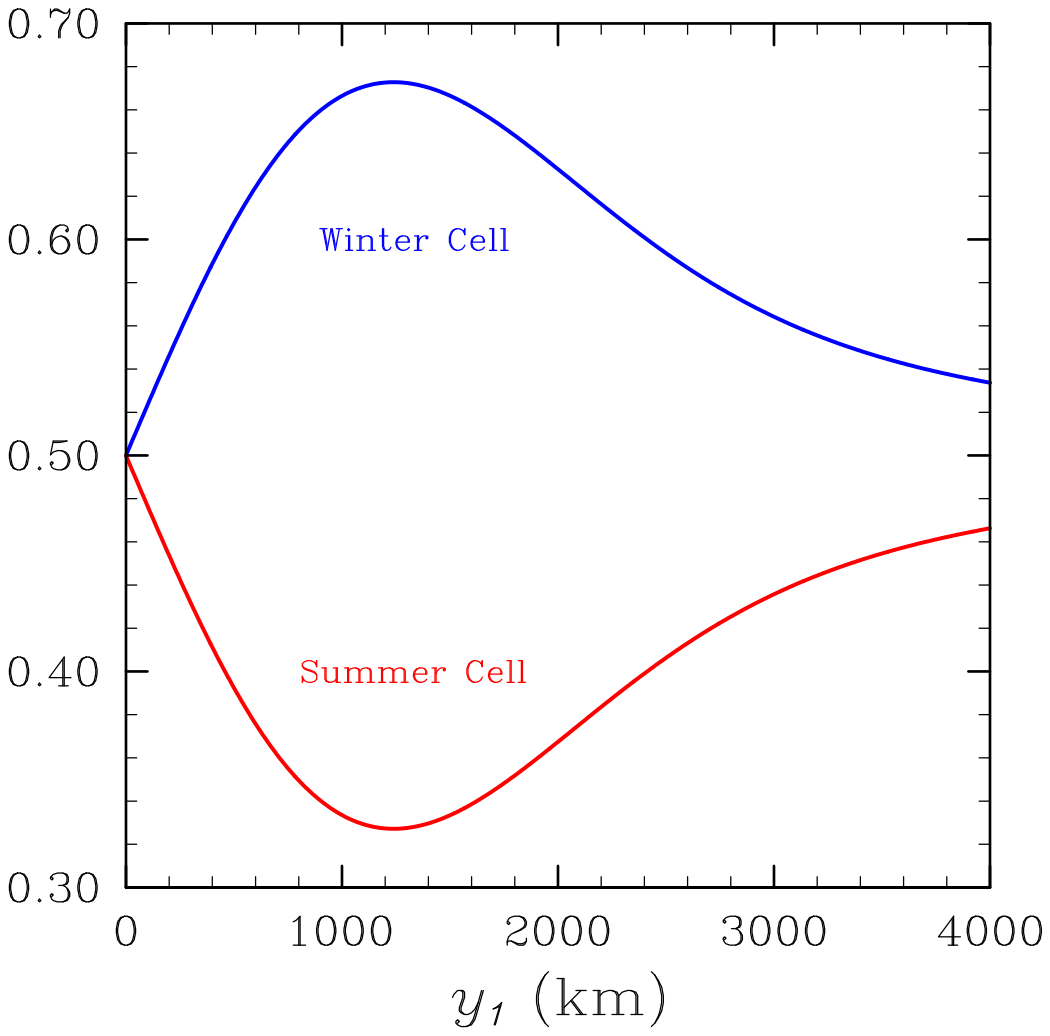

FIG. 4.5. Fractional mass flux carried by the summer hemisphere Hadley cell (red) and fractional mass flux carried by the winter hemisphere Hadley cell (blue), for the case of an infinitesimally thin ITCZ at the distance y_1 from the equator. When $y_1 = 1200$ km, approximately 1/3 of the upward mass flux in the ITCZ is partitioned to the summer hemisphere Hadley cell and 2/3 is partitioned to the winter hemisphere cell.

4.3. PRODUCTION OF SHALLOW OVERTURNING CIRCULATIONS THROUGH EKMAN PUMPING

While the direct effects of friction are confined to the boundary layer flow in the lowest kilometer, the inviscid interior is indirectly affected through the meridional circulation produced by the upward extension of the Ekman pumping at the top of the boundary layer. To isolate the effects of the upward penetration of Ekman pumping, consider the case in which $\hat{Q} = 0$ and

$$\mathcal{W}(y) = \begin{cases} \mathcal{W}_{\max} & \text{if } \; y_1 < y < y_2, \\ 0 & \text{otherwise,} \end{cases} \tag{4.10}$$

where $\mathcal{W}_{\max}$ is a constant. This results in

$$\mathcal{F}_m = \mathcal{W}_{\max} \mathcal{Z}_m(0), \tag{4.11}$$

which leads to the final solution

$$\psi(y,z,t) = \mathcal{W}_{\max} S(t)\, e^{-z/2H} \sum_{m=0}^{\infty} b_m \mathcal{Z}_m(0) \left[G_m(y,y_2) - G_m(y,y_1) \right] \mathcal{Z}_m(z). \tag{4.12}$$

Note that the shallow overturning solution (4.12) differs from the deep overturning solution (4.5) in the sense that (4.12) involves a sum over all vertical modes.

Figure 4.6 shows isolines of $\psi(y,z,t)$ for the four cases $(y_1, y_2) = (0, 500)$, $(y_1, y_2) = (500, 1000)$, $(1000, 1500)$, $(1500, 2000)$ km, all using $S(t) = 1$, as will be the case in all the following diagrams. Figure 4.7 shows essentially the same information in terms of three-hour trajectories, while Figs. 4.8 and 4.9 show isolines of the meridional velocity $v(y,z,t)$ and the log-pressure vertical velocity $w(y,z,t)$. Since the upward penetration of the boundary layer pumping is so restricted in tropical regions, only a small portion (i.e., $0 \leq z \leq 3$ km) of the vertical domain

is displayed in Figs. 4.6–4.9. The main conclusion from these results is that Ekman pumping in the tropical region does not penetrate very far in the vertical. For example, for Ekman pumping in the region $1500 \leq y \leq 2000$ km, the upward penetration is approximately 2 km (see Fig. 4.9), while for pumping in the region $500 \leq y \leq 1000$ km, the upward penetration is only 1 km. In addition, boundary layer fluid that is pumped upward tends to flow equatorward and poleward primarily in a 1–2 km thick layer just above the top of the boundary layer. As shown in Fig. 4.10 (which is the shallow circulation counterpart of Fig. 4.5), most of the shallow return flow is in the equatorward rather than the poleward direction.

Figure 4.11 shows isolines of the streamfunction that results when both the diabatic and frictional forcings act together. The result of this experiment compared to the separate cases is a stronger Hadley cell at low and mid levels away from the ITCZ with subsidence extending further north and south toward the poles. The shallow meridional circulation patterns seem to be most apparent when the ITCZ is close to the equator, i.e., in for Figs. 4.11a,b. In contrast, when the ITCZ is far north of the equator, as in Fig. 4.11d, only a single deep cell occurs in each hemisphere and no shallow meridional circulation is present. When Ekman pumping occurs very close to the equator, the resistance to horizontal motion is so weak that the return meridional flow occurs very close to the top of the boundary layer, i.e., there is very little upward penetration of the Ekman pumping. Thus, very shallow Hadley circulations tend to occur when Ekman pumping occurs close to the equator.

4.4. A POTENTIAL VORTICITY PERSPECTIVE

We have formulated the zonally symmetric balanced model using (y, z)-coordinates. In this formulation the Eliassen meridional circulation equation emerges as a key part of the dynamics. Another approach to this problem is to define an angular momentum coordinate Y by $\frac{1}{2}\beta Y^2 =$

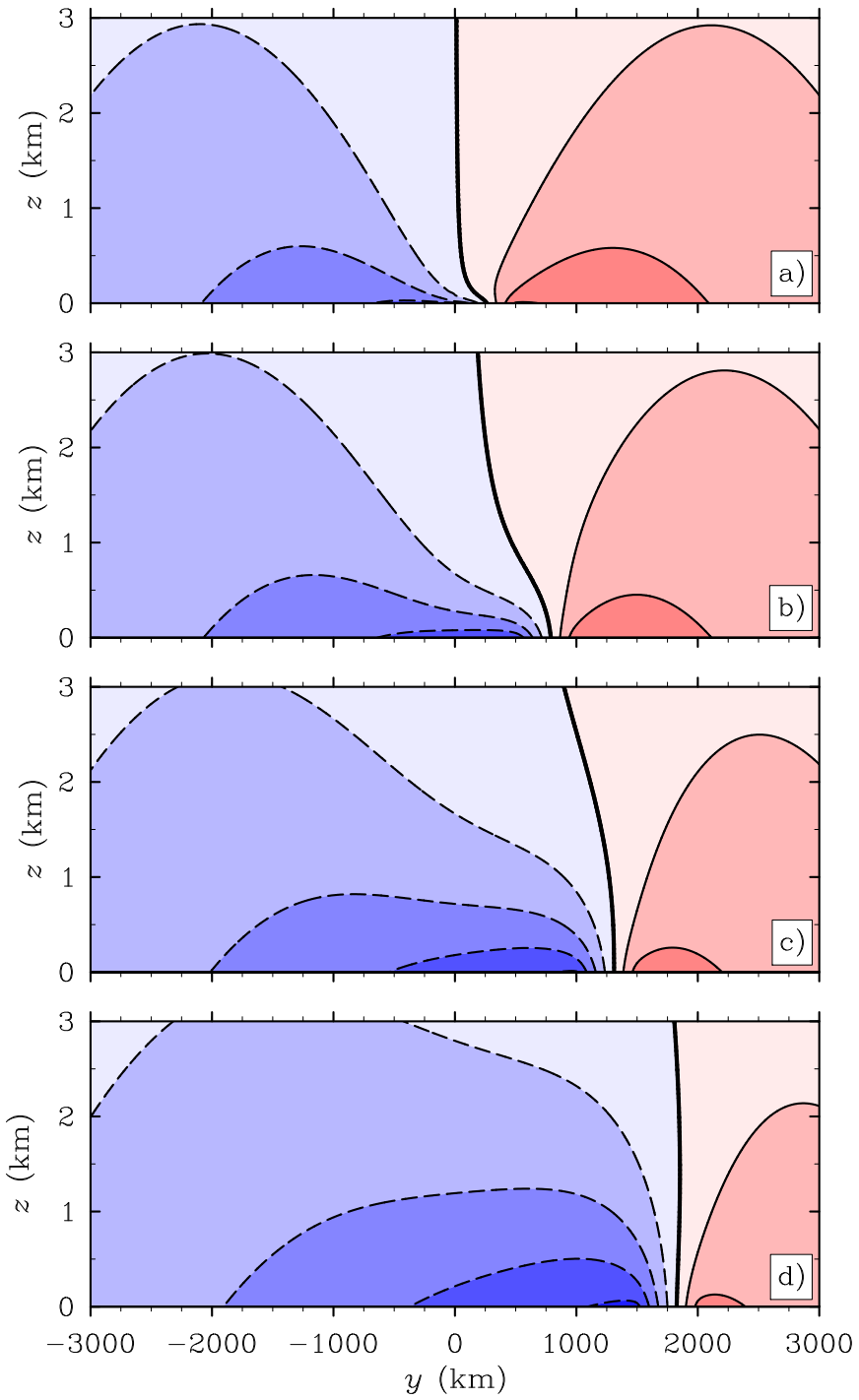

FIG. 4.6. Isolines of the streamfunction $\psi(y, z)$ for the shallow overturning case. Note that here, and in the following three figures, the vertical scale extends upward to only 3 km. Solid contours and red shading are for $\psi > 0$, with dashed contours and blue shading for $\psi < 0$. The contour interval is 400 m^2 s^{-1}. The maximum magnitude for $\psi(y, z)$ is 1712 m^2 s^{-1}. Four ITCZ positions are shown: (a) $(y_1, y_2) = (0, 500)$ km; (b) $(y_1, y_2) = (500, 1000)$ km; (c) $(y_1, y_2) = (1000, 1500)$ km; and (d) $(y_1, y_2) = (1500, 2000)$ km.

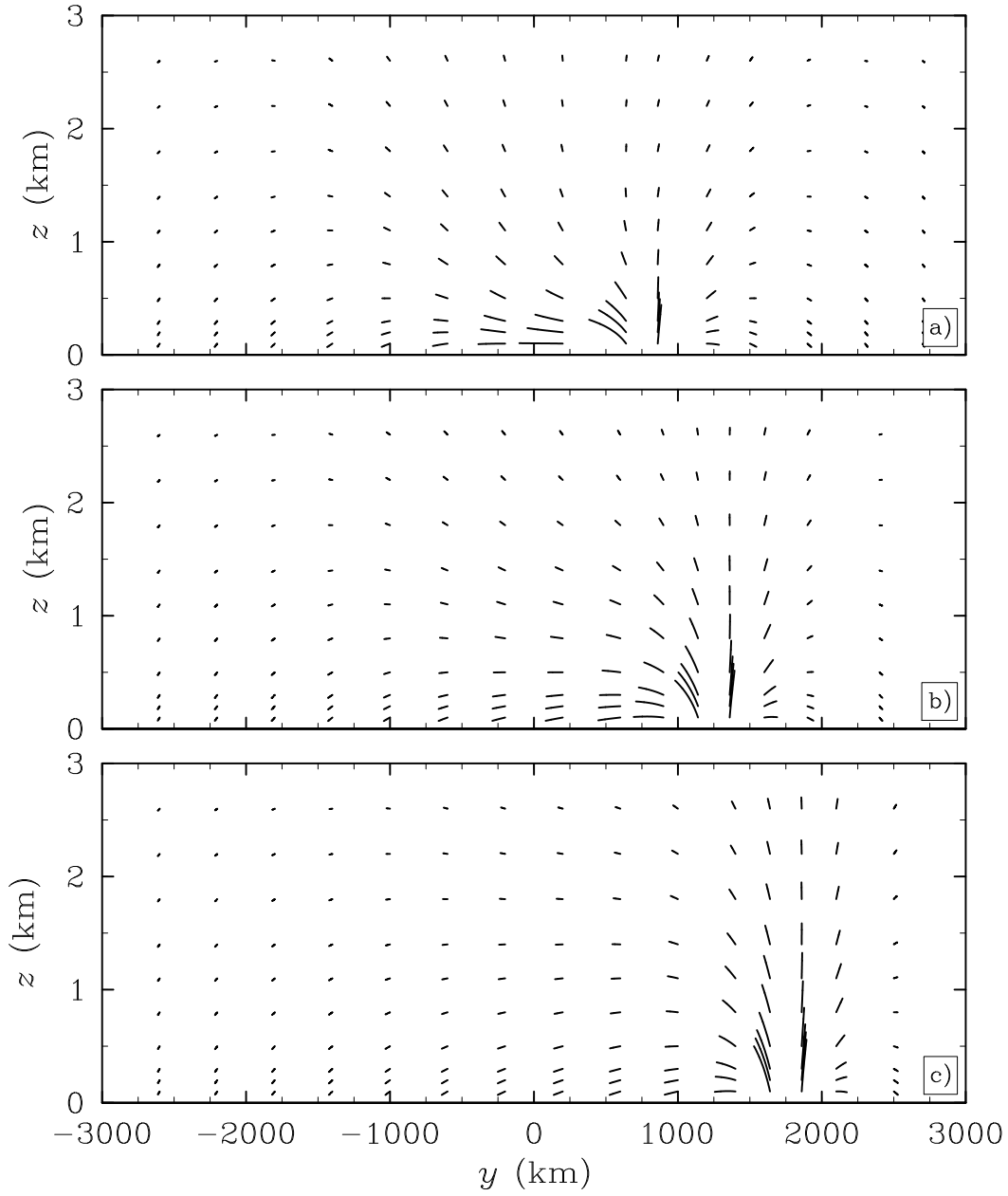

FIG. 4.7. Parcel trajectories during the first three days for three Ekman pumping displacements: (a) $(y_1, y_2) = (500, 1000)$ km; (b) $(y_1, y_2) = (1000, 1500)$ km; and (c) $(y_1, y_2) = (1500, 2000)$ km. Note the grid changes for each ITCZ displacement

$\frac{1}{2}\beta y^2 - u$, and then formulate the zonally symmetric balanced model using (Y, θ)-coordinates, where θ is the potential temperature. In this formulation an Eliassen meridional circulation equation does not arise. Instead, the dynamics reduces to a potential vorticity evolution equation and a potential vorticity invertibility principle (an elliptic problem), from which the balanced wind and

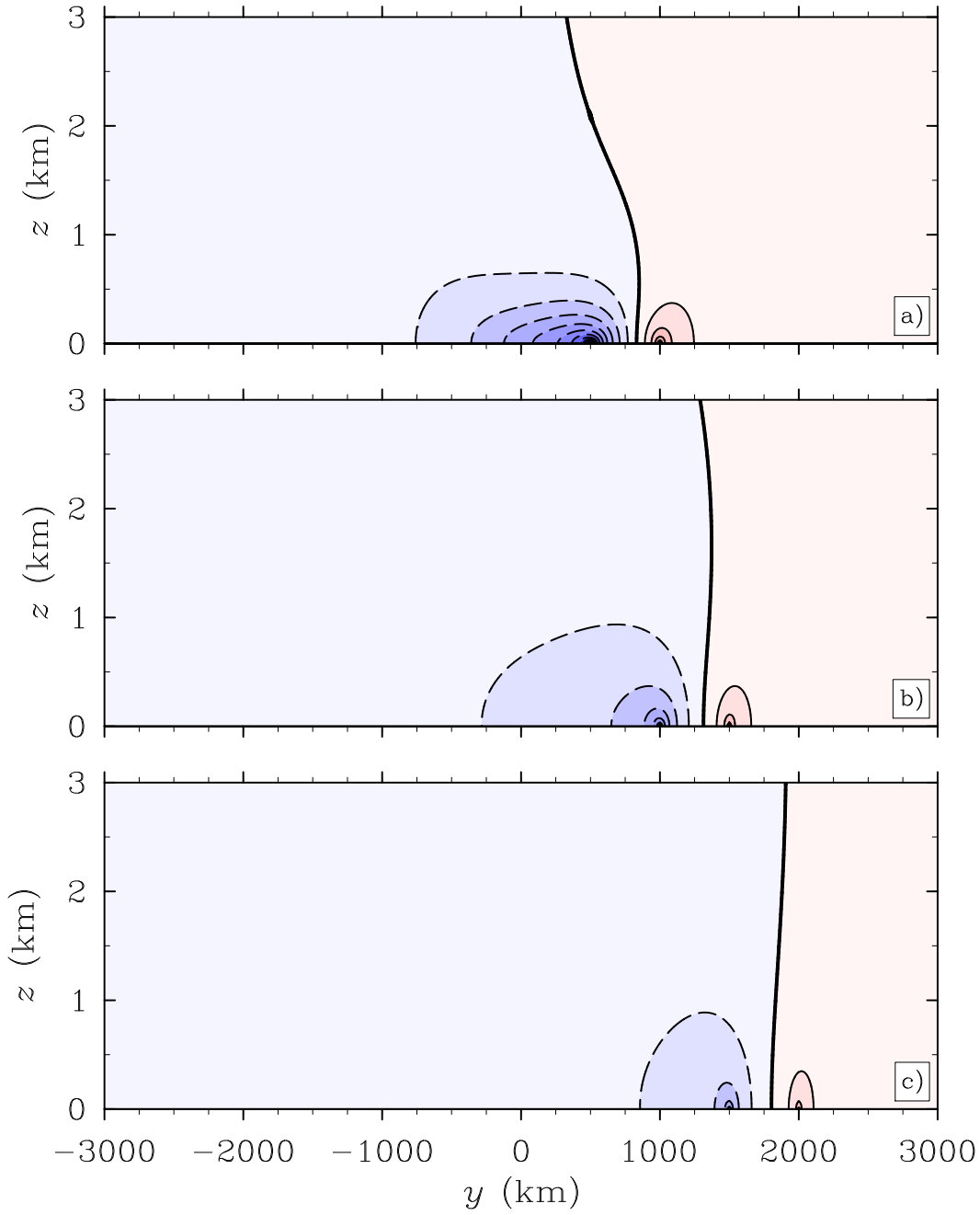

FIG. 4.8. Meridional velocity $v(y, z)$, with red indicating southerly flow ($v > 0$) and blue indicating northerly flow ($v < 0$). The contour interval is 0.5 m s^{-1}. The maximum magnitude for $v(y, z)$ is 7.922 m s^{-1}. Three ITCZ positions are shown: (a) $(y_1, y_2) = (500, 1000)$ km; (b) $(y_1, y_2) = (1000, 1500)$ km; and (c) $(y_1, y_2) = (1500, 2000)$ km.

mass fields are obtained. A more detailed discussion of this approach can be found in Schubert et al. (1991).

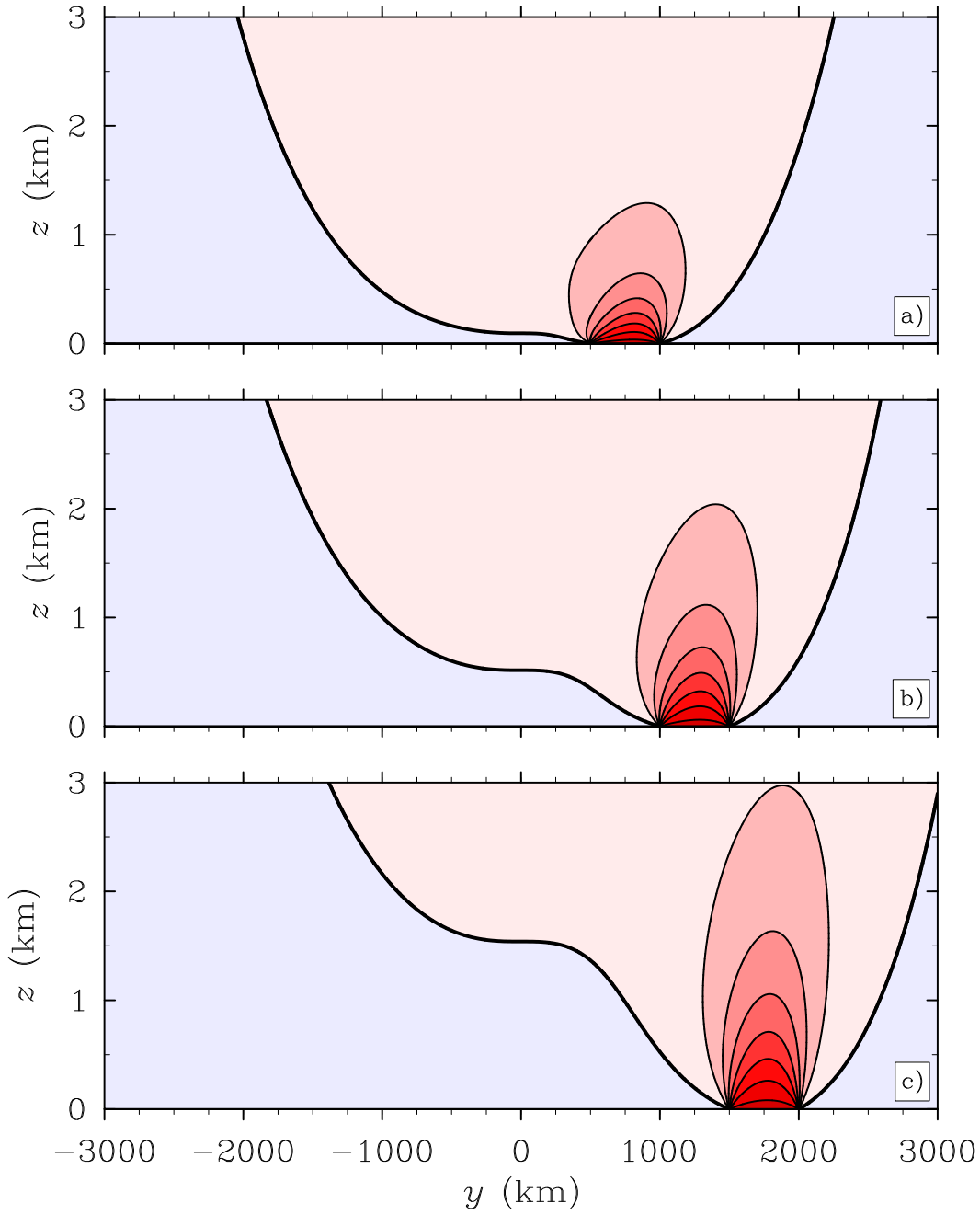

FIG. 4.9. Log-pressure vertical velocity, with red indicating ascent and blue indicating descent. The contour interval is 0.5 mm s^{-1}, with the zero contour indicated in bold. The maximum magnitude for $w(y, z)$ is 3.774 mm s^{-1}. Three ITCZ positions are shown: (a) $(y_1, y_2) = (500, 1000)$ km; (b) $(y_1, y_2) = (1000, 1500)$ km; and (c) $(y_1, y_2) = (1500, 2000)$ km. Note that the vertical penetration depth is reduced when the Ekman pumping is located near the equator.

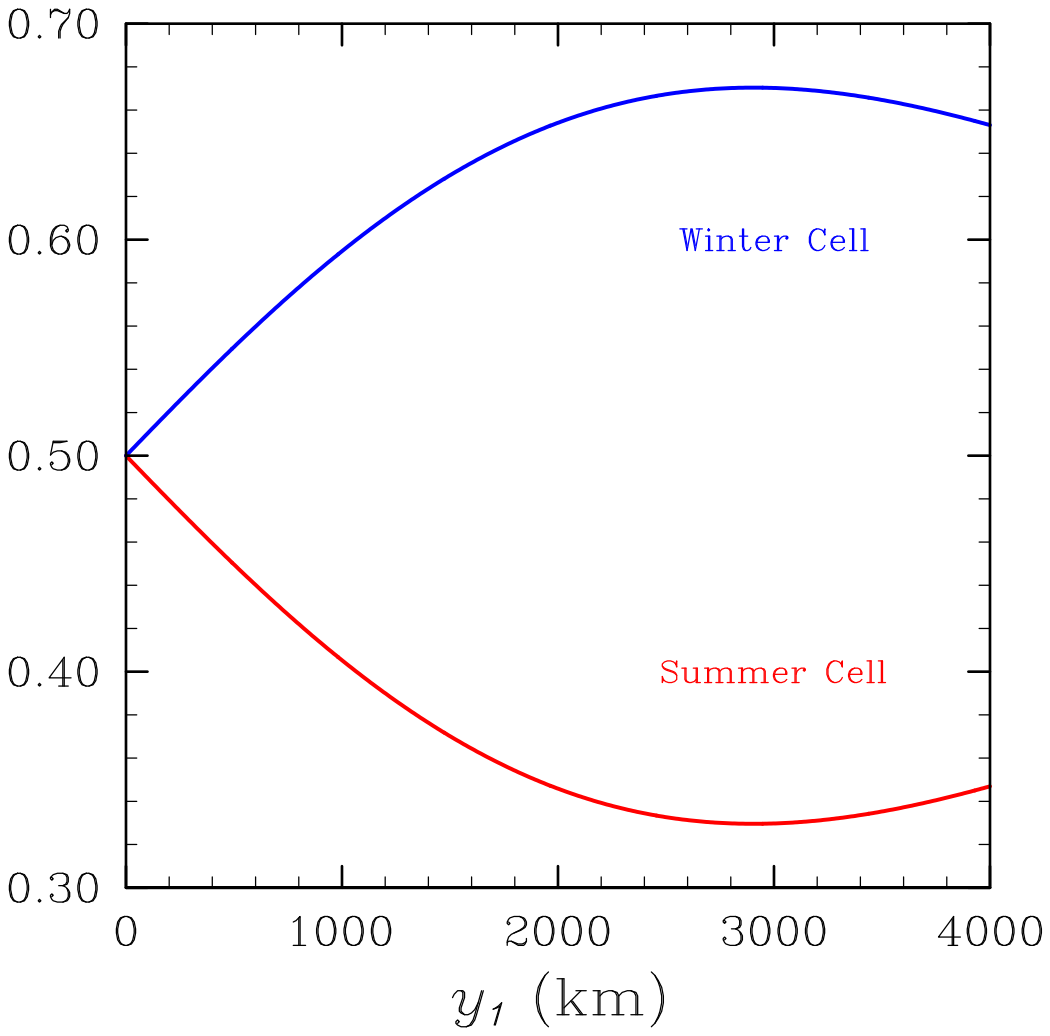

FIG. 4.10. Fractional mass flux carried by the summer hemisphere Hadley cell and fractional mass flux carried by the winter hemisphere Hadley cell, for the case of an infinitesimally thin ITCZ.

The above discussion motivates a potential vorticity perspective of the results shown in section 4.1. The potential vorticity equation, derived from the original system (3.1)–(3.5), is

$$\frac{\partial q}{\partial t} = -\beta v + \frac{gS(t)\,\beta y}{c_p T_0 N^2}\left(\frac{\partial Q}{\partial z} - \frac{Q}{H}\right), \tag{4.13}$$

where

$$q = -\frac{\partial u}{\partial y} + \frac{g\beta y}{T_0 N^2}\left(\frac{\partial T}{\partial z} - \frac{T}{H}\right) \tag{4.14}$$

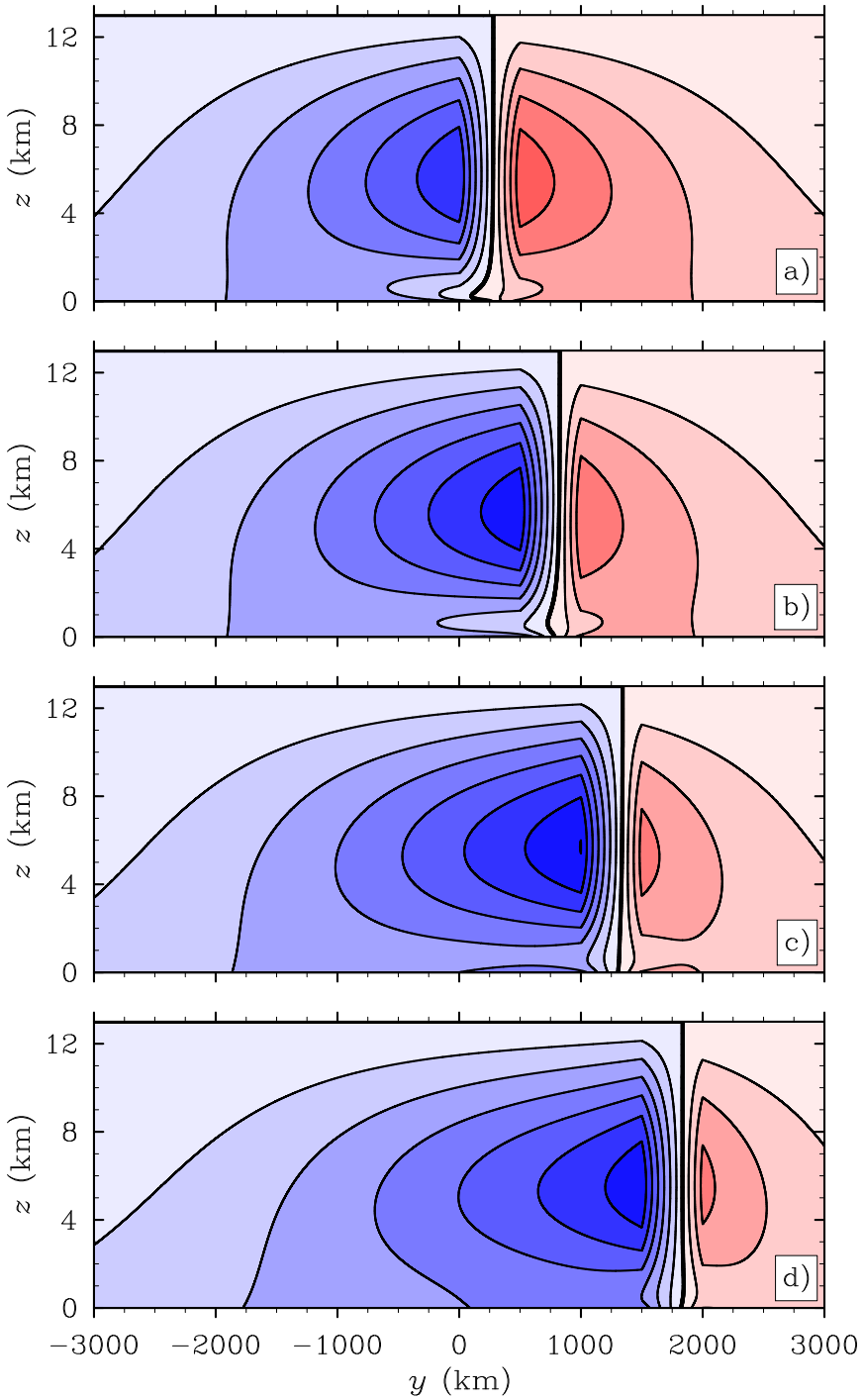

FIG. 4.11. Isolines of the streamfunction $\psi(y, z)$ for the deep and the shallow overturning case. Solid contours and red shading are for $\psi > 0$, with dashed contours and blue shading for $\psi < 0$. The contour interval is 500 m^2 s^{-1}. The maximum magnitude of $\psi(y, z)$ is 2852 m^2 s^{-1}. Four ITCZ positions are shown: (a) $(y_1, y_2) = (0, 500)$ km; (b) $(y_1, y_2) = (500, 1000)$ km; (c) $(y_1, y_2) = (1000, 1500)$ km; and (d) $(y_1, y_2) = (1500, 2000)$ km. The $Q(y, z)\, e^{-z/H}$ shade interval is 0.5 K day^{-1} and the maximum diabatic heating is 3.496 K day^{-1}

is the potential vorticity anomaly. Figure 4.12 shows isolines of $q_t(y, z, t)$ as computed from (4.13). In the ITCZ region the diabatic term $[gS(t)\,\beta y/(c_p T_0 N^2)][(\partial Q/\partial z) - (Q/H)]$ is dominant over the meridional advection term $-\beta v$, producing a positive PV anomaly in the lower troposphere and a negative PV anomaly in the upper troposphere. Because of the βy factor in the diabatic term, the diabatically produced PV anomalies are biased toward the poleward edge of the ITCZ. Outside the ITCZ, the diabatic term vanishes so $q_t(y, z, t)$ is due entirely to the $-\beta v$ term in (4.13).

Since, for large t, the zonal flow $u(y, z, t)$ is in geostrophic balance and the temperature $T(y, z, t)$ is in hydrostatic balance, the right hand side of (4.14) can be expressed entirely in terms of the geopotential, thereby making (4.14) an invertibility principle from which the balanced wind and mass fields can be recovered from the PV via solution of a second order elliptic problem. Thus, the $u_t(y, z, t)$ fields shown in Fig. 4.4 and the $T_t(y, z, t)$ fields shown in Fig. 4.3 can be considered the balanced zonal flow field and mass field tendencies associated, through the invertibility principle, with the PV tendencies shown in Fig. 4.12.

An important feature of the $q_t(y, z, t)$ field shown in Fig. 4.12 is that there is a tendency to reverse the poleward gradient of PV on the north side of the ITCZ in the lower troposphere and on the south side of the ITCZ in the upper troposphere. Thus, the necessary conditions for combined barotropic-baroclinic instability are naturally evolving. Thus, evolving ITCZs seem to naturally contain the seeds of their own destruction.

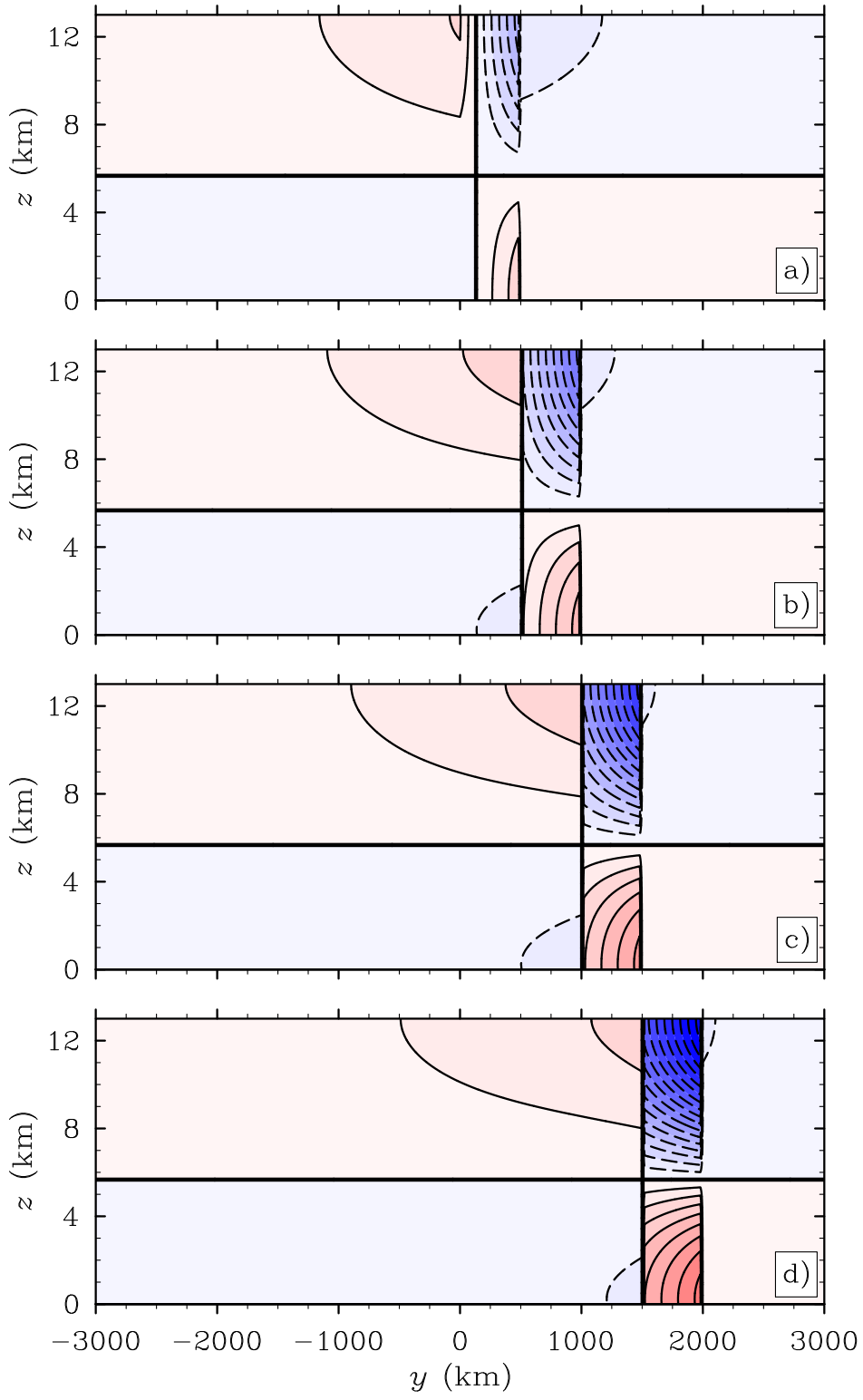

FIG. 4.12. Potential vorticity tendency $q_t(y, z)$, computed from (4.13), with blue indicating $q_t < 0$ and red indicating $q_t > 0$. Four ITCZ positions are shown: (a) $(y_1, y_2) = (0, 500)$ km; (b) $(y_1, y_2) = (500, 1000)$ km; (c) $(y_1, y_2) = (1000, 1500)$ km; and (d) $(y_1, y_2) = (1500, 2000)$ km.

CHAPTER 5

CONCLUDING REMARKS

An observational analysis of YOTC data has confirmed the existence of both a deep and a shallow overturning meridional circulation in the eastern Pacific. To understand the dynamics of these meridional circulations, a zonally symmetric model on the equatorial β-plane has been formulated and the associated meridional circulation equation has been derived. This meridional circulation equation is a partial differential equation in (y, z, t). It contains two types of forcing: (1) horizontal variation of the interior diabatic heating; (2) Ekman pumping at the top of the boundary layer. Since the problem is linear, the meridional circulations attributable to these two forcing effects can be treated separately, and then the resulting flows can simply be added together to obtain the total response.

The meridional circulation equation has been solved analytically by first performing a vertical transform that converts the partial differential equation in (y, z, t) into a system of partial differential equations in (y, t) for the meridional structures of all the vertical modes. These partial differential equations have been solved via both the Green's function approach (evanescent basis functions) and the Hermite transform approach (oscillatory basis functions). These two approaches yield two different mathematical representations of the same physical solution. For understanding the basic asymmetry between the intensities of the winter hemisphere and the summer hemisphere Hadley cells, the Green's function approach is preferable because of the efficiency of the mathematical representation, which is simply a superposition of two Green's functions written in terms of parabolic cylinder functions of order $-\frac{1}{2}$.

The analytical solutions take simple forms in two special cases: (1) Forcing by deep diabatic heating that projects only onto the first internal mode in the absence of Ekman pumping; (2) Forcing by Ekman pumping in the absence of any diabatic heating. Case (1) leads to deep overturning circulations, while case (2) leads to shallow overturning circulations. Both circulations show a marked asymmetry between the winter hemisphere and summer hemisphere overturning cells. This asymmetry is due to the basic anisotropy introduced by the spatially varying inertial stability coefficient in the meridional circulation equation. A simple physical interpretation is that fluid parcels forced near the equator to overturn by diabatic and frictional effects tend to move much more easily in the horizontal direction because the resistance to horizontal motion (i.e. inertial stability) is so much less than the resistance to vertical motion (i.e., static stability). In fact, when Ekman pumping occurs very close to the equator, the resistance to horizontal motion is so weak that the return meridional flow occurs very close to the top of the boundary layer, i.e., there is very little upward penetration of the Ekman pumping. Thus, very shallow Hadley circulations tend to occur when Ekman pumping occurs close to the equator.

In closing we note that the analytical solutions of the meridional circulation equation are consistent with the extent and shape of upper tropospheric dry regions regularly observed in satellite water vapor images, such as the one shown in Figure 3.1. These upper tropospheric dry regions play an important role in our ability to observe the universe with surface-based visible, infrared, and millimeter/submillimeter telescopes. The best astronomical observatory sites are at high altitudes in regions of persistently low upper tropospheric water vapor, such as Mauna Kea, Hawaii, the mountains of northern Chile, and the Canary Islands. These sites are above the trade wind inversion layer, which normally lies between 2000 and 2500 m. Above the trade wind inversion the

clear, dry air generally provides excellent observing conditions, but there can be important variations on synoptic, seasonal, and interannual time scales. As discussed by Businger et al. (2002), forecasts of weather conditions can play an important role in telescope scheduling and observing strategy at these sites.

This work has shown that Ekman pumping is a viable forcing mechanism for the Shallow Hadley Circulation. However, diabatic heating due to shallow precipitating convection and surface heating (in analogy with land/sea breezes, as discussed by Nolan et al. (2007, 2010)) are also viable forcing mechanisms. Further research is needed to understand the relative importance of these three forcing mechanisms.

REFERENCES

Back, L. and C. Bretherton, 2009a: On the relationship between SST gradients, boundary layer winds and convergence over the tropical oceans. *J. Climate*, **22**, 4182–4196.

Businger, S., R. McLaren, R. Ogasawara, D. Simons, and R. Wainscoat, 2002: Starcasting. *Bull. Amer. Meteor. Soc.*, **83**, 858–871.

Cau, P., J. Methven, and B. J. Hoskins, 2007: Origins of dry air in the tropics and subtropics. *J. Climate*, **20**, 2745–2759.

Chelton, D., M. Freilich, and S. Esbensen, 2000a: Satellite observations of the wind jets off the Pacific coast of Central America. part II: Regional relationships and dynamical considerations. *Mon. Wea. Rev.*, **128**, 2019–2042.

Chelton, D., et al., 2000b: Observations of coupling between surface wind and sea surface temperature in the Eastern Tropical Pacific. *J. Climate*, **14**, 1479–1498.

de Szoeke, S., C. Bretherton, N. Bond, M. Cronin, and B. Morley, 2005: EPIC 95°W observations of the Eastern Pacific atmospheric boundary layer from the cold tongue to the ITCZ. *J. Atmos. Sci.*, **62**, 426–442.

Deser, C., J. Bates, and S. Wahl, 1993: The influence of sea surface temperature gradients on stratiform cloudiness along the equatorial front in the Pacific Ocean. *J. Climate*, **6**, 1172–1179.

Dias, J. and O. Pauluis, 2009: Convectively coupled waves propagating along an equatorial ITCZ. *J. Atmos. Sci.*, **66**, 2237–2255.

Eliassen, A., 1952: Slow thermally or frictionally controlled meridional circulations in a circular vortex. *Astrophysica Norvegica*, **5**, 19–60.

Enfield, D. and S. Lee, 2005: The heat balance of the Western Hemisphere Warm Pool. *J. Climate*, **18**, 2662–2681.

Galewsky, J., A. Sobel, and I. Held, 2005: Diagnosis of subtropical humidity dynamics using tracers of last saturation. *J. Atmos. Sci.*, **62**, 3353–3367.

Hack, J. and W. Schubert, 1990: Some dynamical properties of idealized thermally-forced meridional circulations in the Tropics. *Meteorol. Atmos. Phys.*, **44**, 101–117.

Hack, J., W. Schubert, D. Stevens, and H. Kuo, 1989: Response of the Hadley circulation to convective forcing in the ITCZ. *J. Atmos. Sci.*, **46**, 2957–2973.

Haynes, P. and T. Shepherd, 1989: The importance of surface pressure changes in the response of the atmosphere to zonally-symmetric thermal and mechanical forcing. *Quart. J. Roy. Meteor. Soc.*, **115**, 1181–1208.

Held, I. and A. Hou, 1980: Nonlinear axially symmetric circulations in a nearly inviscid atmosphere. *J. Atmos. Sci.*, **37**, 515–533.

Jackson, D. and J. Bates, 2001: Upper tropospheric humidity algorithm assessment. *J. Geophys. Res.*, **32**, 259–270.

Kang, S., I. Held, D. Frierson, and M. Zhao, 2008: The Response of the ITCZ to Extratropical Thermal Forcing: Idealized Slab-Ocean Experiments with a GCM. *J. Climate.*, **21**, 3521–3532.

Lindzen, R. and A. Hou, 1988: Hadley circulations for zonally averaged heating centered off the equator. *J. Atmos. Sci.*, **45**, 2416–2427.

Lindzen, R. and S. Nigam, 1987: On the role of sea surface temperature gradients in forcing low-level winds and convergence in the tropics. *J. Atmos. Sci.*, **44**, 2418–2436.

Masunaga, H. and T. L'Ecuyer, 2010: The Southeast Pacific warm band and double ITCZ. *J. Climate*, **23**, 1189–1208.

Masunaga, H. and T. L'Ecuyer, 2011: Equatorial asymmetry of the East Pacific ITCZ: Observational constraints on the underlying processes. *J. Climate*, **24**, 1784–1800.

McGauley, M., C. Zhang, and N. Bond, 2004: Large-scale characteristics of the atmospheric boundary layer in the Eastern Pacific cold tongue-ITCZ region. *J. Climate*, **17**, 3907–3920.

McNoldy, B., P. Ciesielski, W. Schubert, and R. Johnson, 2004: Surface winds, divergence, and vorticity in stratocumulus regions using QuikSCAT and reanalysis winds. *Geophys. Res. Lett.*, **31**, L08 105.

Neiburger, M., D. Johnson, and C. Chien, 1961: Studies of the structure of the atmosphere over the eastern Pacific Ocean in summer, I. the inversion over the eastern north Pacific Ocean. *Univ. Calif. Publ. meteor.*, **1**, 1–94.

Nolan, D., S. Powell, C. Zhang, and B. Mapes, 2010: Idealized simulations of the Intertropical Convergence Zone and its multilevel flows. *J. Atmos. Sci.*, **67**, 4028–4053.

Nolan, D., C. Zhang, and S. Chen, 2007: Dynamics of the shallow meridional circulation around Intertropical Convergence Zones. *J. Atmos. Sci.*, **64**, 2262–2285.

Philander, S., D. Gu, D. Halpern, G. Lambert, L. N.-C, T. Li, and R. Pacanowski, 1996: Why is the ITCZ mostly north of the Equator. *J. Climate*, **9**, 2958–2972.

Salathé, E. and D. Hartmann, 1997: A trajectory analysis of tropical upper-tropospheric moisture and convection. *J. Climate*, **10**, 2533–2547.

Schneider, E. K., 1977: Axially Symmetric Steady-State Models of the Basic State for Instability and Climate Studies. part II. Nonlinear Calculations. *J. Atmos. Sci.*, **34**, 280–296.

Schreck, C., L.Shi, J. Kossin, and J. Bates, 2013: Identifying the MJO, equatorial waves, and their impacts using 32 years of HIRS upper-tropospheric water vapor. *J. Climate*, **26**, 1418–1431.

Schubert, W., P. Ciesielski, D. Stevens, and H. Kuo, 1991: Potential vorticity modeling of the ITCZ and the Hadley circulation. *J. Atmos. Sci.*, **48**, 1493–1509.

Schubert, W. and B. McNoldy, 2010: Application of the concepts of Rossby length and rossby depth to tropical cyclone dynamics. *J. Adv. Model. Earth Syst.*, **2**, Art. #7, 13 pp.

Sherwood, S., E. Kursinski, and W. Read, 2006: A distribution law for free-tropospheric relative humidity. *J. Climate*, **19**, 6267–6277.

Soden, B. and F. Bretherton, 1993: Upper tropospheric relative humidity from the goes 6.7 μm channel: Method and climatology for July 1987. *J. Geophys. Res.*, **98**, 16,669–16,688.

Soden, B. and F. Bretherton, 1996: Interpretation of TOVS water vapor radiances in terms of layer-average relative humidities: Method and climatology for the upper, middle, and lower troposphere. *J. Geophys. Res.*, **101**, 9333–9343.

Soden, B. and R. Fu, 1995: A satellite analysis of deep convection, upper-tropospheric humidity, and greenhouse effect. *J. Climate*, **8**, 2333–2351.

Sun, D.-Z. and R. Lindzen, 1993: Distribution of tropical tropospheric water vapor. *J. Atmos. Sci.*, **50**, 1643–1660.

Tomas, R. and P. Webster, 1997: The role of inertial instability in determining the location and strength of near-equatorial convection. *Quart. J. Roy. Meteor. Soc.*, **123**, 1445–1482.

Trenberth, K., D. Stepaniak, and J. Caron, 2000: The global monsoon as seen through the divergent atmospheric circulation. *J. Climate*, **13**, 3969–3993.

von Ficker, H., 1936: Die passatinversion. *Veroeff. Meteor. Inst. Univ. Berlin*, **1**, 1–33.

Waliser, D., et al., 2012: The Year of Tropical Convection (May 2008–April 2010) Climate Variability and Weather Highlights. *Bull. Amer. Meteor. Soc.*, **93**, 1189–1218.

Wallace, J., T. Mitchell, and C. Deser, 1989: The influence of sea-surface temperature on surface wind in the eastern equatorial Pacific: Seasonal and interannual variability. *J. Climate*, **2**, 1492–1499.

Wang, C. and D. Enfield, 2001: The tropical Western Hemisphere Warm Pool. *Geophys. Res. Lett.*, **28**, 1635–1638.

Wang, C. and D. Enfield, 2005: A further study of the Tropical Western Hemisphere Warm Pool. *J. Climate*, **16**, 1476–1493.

Wang, Y., S. Xie, B. Wang, and H. Xu, 2005: Large-scale atmospheric forcing by southeast Pacific boundary layer clouds: A regional model study. *J. Climate*, **18**, 934–951.

Zhang, C., M. McGauley, and N. Bond, 2004: Shallow meridional circulation in the tropical eastern Pacific. *J. Climate*, **17**, 133–139.

Zhang, C., D. Nolan, C. Thorncroft, and H. Nguyen, 2008: Shallow meridional circulations in the tropical atmosphere. *J. Climate*, **21**, 3453–3470.

APPENDIX A

VERTICAL TRANSFORM

The mathematical principles underlying the vertical transform pair (3.22) and (3.23) are the orthonormality and completeness of the eigenfunctions $\mathcal{Z}_m(z)$, which we now discuss. Consider the eigenfunction $\mathcal{Z}_m(z)$, which is a solution of (3.24)–(3.26), and the eigenfunction $\mathcal{Z}_{m'}(z)$, which is a solution of (3.24)–(3.26) with m replaced by m'. To obtain the orthonormality relation, multiply the equation for $\mathcal{Z}_m(z)$ by $\mathcal{Z}_{m'}(z)$, then multiply the equation for $\mathcal{Z}_{m'}(z)$ by $\mathcal{Z}_m(z)$, and finally integrate the difference of the resulting equations to obtain

$$\frac{1}{g}\left(\frac{1}{h_m}-\frac{1}{h_{m'}}\right)\int_0^{z_T}\mathcal{Z}_m(z)\mathcal{Z}_{m'}(z)\,N^2(z)\,dz+\left[\mathcal{Z}_{m'}(z)\frac{d\mathcal{Z}_m(z)}{dz}-\mathcal{Z}_m(z)\frac{d\mathcal{Z}_{m'}(z)}{dz}\right]_0^{z_T}=0. \tag{A.1}$$

The boundary terms in (A.1) can be evaluated with the aid of the boundary conditions (3.25) and (3.26). Then, for distinct eigenvalues ($h_m \neq h_{m'}$) and for normalized $\mathcal{Z}_m(z)$, we have the orthonormality relation

$$\int_0^{z_T}\mathcal{Z}_m(z)\mathcal{Z}_{m'}(z)\,dz+\frac{g}{N^2}\mathcal{Z}_m(0)\mathcal{Z}_{m'}(0)=\begin{cases} z_T & \text{if } m=m' \\ 0 & \text{if } m\neq m'. \end{cases} \tag{A.2}$$

To confirm that (3.22) is the proper transform for the expansion (3.23), we multiply (3.23) by $\mathcal{Z}_{m'}(z)$ and then integrate over z to obtain

$$\int_0^{z_T}\hat{\psi}(y,z)\mathcal{Z}_{m'}(z)\,N^2(z)\,dz=\sum_{m=0}^{\infty}\hat{\psi}_m(y)\int_0^{z_T}\mathcal{Z}_m(z)\mathcal{Z}_{m'}(z)\,N^2(z)\,dz. \tag{A.3}$$

Similarly, we multiply (3.2), evaluated at $z = 0$, by $\mathcal{Z}_{m'}(0)$ to obtain

$$\hat{\psi}(y,0)\mathcal{Z}_{m'}(0) = \sum_{m=0}^{\infty} \hat{\psi}_m(y)\mathcal{Z}_m(0)\mathcal{Z}_{m'}(0). \tag{A.4}$$

Multiplying (A.4) by g/N^2, adding the result to (A.3), and then using the orthonormality relation (A.2), we obtain (3.1), confirming the validity of the transform pair (3.1) and (3.2).

To prove that all the eigenvalues of the problem (3.24)–(3.26) are positive, multiply (3.24) by $\mathcal{Z}_m(z)$ to obtain

$$\frac{N^2\mathcal{Z}_m^2}{gh_m} + \frac{d}{dz}\left(\mathcal{Z}_m\frac{d\mathcal{Z}_m}{dz}\right) = \left(\frac{d\mathcal{Z}_m}{dz}\right)^2 + \left(\frac{\mathcal{Z}_m}{2H}\right)^2. \tag{A.5}$$

Integrating (A.5) over z and making use of the boundary conditions (3.25) and (3.26), we obtain

$$\begin{aligned}\frac{1}{h_m}&\left\{\frac{1}{g}\int_0^{z_T}\mathcal{Z}_m^2(z)\,N^2(z)\,dz + \mathcal{Z}_m^2(0)\right\}\\ &= \int_0^{z_T}\left\{\left(\frac{d\mathcal{Z}_m(z)}{dz}\right)^2 + \left(\frac{\mathcal{Z}_m(z)}{2H}\right)^2\right\}dz + \frac{\mathcal{Z}_m^2(0)}{2H}.\end{aligned} \tag{A.6}$$

The right hand side of (A.6) is positive. Since $N^2 > 0$, the term in braces on the left hand side of (A.6) is also positive. Thus, all the eigenvalues are positive, i.e., $h_m > 0$ for all m.

To determine if the eigenfunctions $\mathcal{Z}_m(z)$ form a complete set, we first write (3.1) in the form

$$\hat{\psi}_m(y) = \frac{1}{g}\int_0^{z_T}\left[1+\delta(z')\right]\hat{\psi}(y,z')\mathcal{Z}_m(z')N^2(z')dz', \tag{A.7}$$

where $\delta(z')$ satisfies

$$\frac{1}{g}\int_0^{z_T}\delta(z')N^2(z')dz' = 1. \tag{A.8}$$

Using (A.7) in (3.34), we obtain

$$\hat{\psi}(y,z) = \frac{1}{g}\int_0^{z_T} \left\{ [1+\delta(z')] \sum_{m=0}^{\infty} \mathcal{Z}_m(z)\mathcal{Z}_m(z') \right\} \hat{\psi}(y,z')N^2(z')dz'. \tag{A.9}$$

The right hand side of (A.9) evaluates to $\hat{\psi}(y,z)$ if

$$[1+\delta(z')] \sum_{m=0}^{\infty} \mathcal{Z}_m(z')\mathcal{Z}_m(z) = \delta(z'-z), \tag{A.10}$$

which is the completeness relation. Although we shall not give a general proof of (A.10), we shall confirm it numerically for the special case of constant N in Appendix B. For further discussions on completeness relations, see Arfken and Weber (1990, section 8.4) and Courant and Hilbert (1953, Volume I, section 6.3).

APPENDIX B

CALCULATION OF THE EIGENVALUES h_m AND THE EIGENFUNCTIONS $\mathcal{Z}_m(z)$

To solve the Sturm-Liouville problem (3.24)–(3.26), consider the idealized case in which the buoyancy frequency N is a constant given by $N = 1.2 \times 10^{-2}$ s^{-1}. As we shall see, the solution of the second order equation (3.24) has different forms depending on the eigenvalues h_m. We begin by exploring the possibility that one of the eigenvalues is given by $\hat{h}$, which is defined by $\hat{h} = (2NH)^2/g = 4328$ m. The corresponding eigenfunction $\hat{\mathcal{Z}}(z)$ then satisfies $d^2\hat{\mathcal{Z}}/dz^2 = 0$, in which case the solution satisfying the upper boundary condition (3.25) is $\hat{\mathcal{Z}}(z) = C(z_T - z)$, where C is a constant. The lower boundary condition is satisfied if $\{1 + z_T[(1/H) - (1/\hat{h})]\}C = 0$. We shall assume that the constant z_T is specified in such a way that $z_T \neq [(1/\hat{h}) - (1/H)]^{-1} = 8731$ m, so that $1 + z_T[(1/H) - (1/\hat{h})] \neq 0$ and $C = 0$, meaning that the boundary value problem does not have a nontrivial eigenfunction with corresponding eigenvalue $h_m = \hat{h}$. Since we have already shown that $h_m > 0$, we now separately investigate the two cases: $h_m > \hat{h}$ (Case 1) and $0 < h_m < \hat{h}$ (Case 2).

Case 1. If the eigenvalues satisfy $h_m > \hat{h}$, then the equation for $\mathcal{Z}_m(z)$ is

$$\frac{d^2\mathcal{Z}_m(z)}{dz^2} - \frac{\mu_m^2}{z_T^2}\mathcal{Z}_m = 0, \tag{B.1}$$

where

$$\frac{\mu_m^2}{z_T^2} = \frac{N^2}{g}\left(\frac{1}{\hat{h}} - \frac{1}{h_m}\right) > 0. \tag{B.2}$$

In this case the vertical structure functions satisfying the upper boundary condition are

$$\mathcal{Z}_m(z) = A_m \sinh[\mu_m(1 - z/z_T)], \tag{B.3}$$

where A_m is the normalization factor. Through application of the lower boundary condition (3.26), it can be shown that μ_m is the solution of

$$\tanh(\mu_m) = \frac{\mu_m}{(z_T/\hat{h})[1 - \hat{h}/2H - (2H\mu_m/z_T)^2]}. \tag{B.4}$$

The transcendental equation (B.4) has only one solution, denoted by μ_0 and having the value $\mu_0 = 0.4686$. The corresponding eigenvalue h_0 is obtained from (B.2), written in the form

$$h_0 = \hat{h}\left[1 - (2H\mu_0/z_T)^2\right]^{-1} \approx 7075\,\mathrm{m}. \tag{B.5}$$

The top line in the orthonormality relation (A.2) is satisfied if the normalization factor is given by

$$A_0 = \left\{\frac{N^2 z_T}{2g}\left[\frac{\sinh(\mu_0)\cosh(\mu_0)}{\mu_0} - 1\right] + \sinh^2(\mu_0)\right\}^{-1/2}. \tag{B.6}$$

Case 2. If the eigenvalues lie in the range $0 < h_m < \hat{h}$, then the equation for $\mathcal{Z}_m(z)$ is

$$\frac{d^2\mathcal{Z}_m(z)}{dz^2} + \frac{\nu_m^2}{z_T^2}\mathcal{Z}_m = 0, \tag{B.7}$$

where

$$\frac{\nu_m^2}{z_T^2} = \frac{N^2}{g}\left(\frac{1}{h_m} - \frac{1}{\hat{h}}\right) > 0. \tag{B.8}$$

In this case the vertical structure functions satisfying the upper boundary condition are

$$\mathcal{Z}_m(z) = B_m \sin[\nu_m(1 - z/z_T)], \tag{B.9}$$

where B_m is the normalization factor. Through application of the lower boundary condition (3.26), it can be shown that ν_m is the solution of

$$\tan(\nu_m) = \frac{\nu_m}{(z_T/\hat{h})[1 - \hat{h}/2H + (2H\nu_m/z_T)^2]}. \tag{B.10}$$

After the transcendental equation (B.10) is solved for ν_m, the eigenvalues h_m can be obtained from (B.8), written in the form

$$h_m = \hat{h}\left[1 + (2H\nu_m/z_T)^2\right]^{-1} \approx \hat{h}\left[1 + (2Hm\pi/z_T)^2\right]^{-1}. \tag{B.11}$$

The second (approximate) equality follows from the fact that the solutions of the transcendental equation (A.10) are approximately $\nu_m \approx m\pi$ for $m = 1, 2, \cdots$, with the accuracy of the estimate improving as m increases. The exact and approximate eigenvalues are listed in Table 3.1. Finally, the top line in the orthonormality relation (A.2) is satisfied if the normalization factor is given by

$$B_m = \left\{ \frac{N^2 z_T}{2g}\left[1 - \frac{\sin(\nu_m)\cos(\nu_m)}{\nu_m}\right] + \sin^2(\nu_m) \right\}^{-1/2}. \tag{B.12}$$

Note that the dependence of the normalization factors B_m on m is weak because $\nu_m \approx m\pi$, making the $\sin(\nu_m)$ terms in (B.12) negligible, which leads to $B_m \approx [2g/(N^2 z_T)]^{1/2} \approx 3.2$.

To summarize, the eigenvalue for the external mode is given by (B.5) where μ_0 is the single solution of the transcendental equation (B.4), while the eigenvalues for the internal modes are given by (B.11) where ν_m are the solutions of the transcendental equation (B.10). The corresponding eigenfunctions are

$$\mathcal{Z}_m(z) = \begin{cases} A_0 \sinh[\mu_0(1 - z/z_T)] & m = 0 \\ \\ B_m \sin[\nu_m(1 - z/z_T)] & m \geq 1, \end{cases} \tag{B.13}$$

where the normalization factors A_0 and B_m are given by (B.6) and (B.12). The first eleven eigenvalues h_m ($m = 0, 1, ..., 10$) are listed in Table 3.1, while the first five eigenfunctions are plotted in Fig. 3.1.

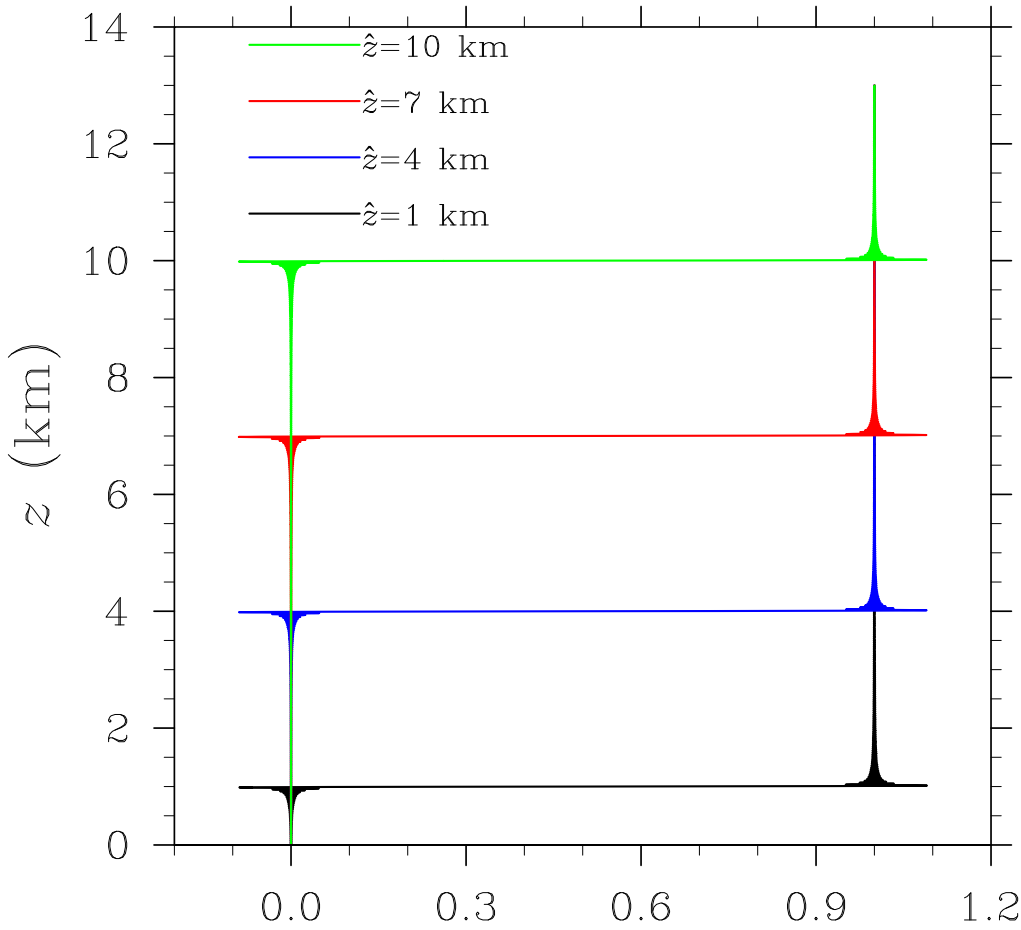

FIG. B.1. Four plots of the left hand side of (B.15) for the choices $\hat{z} = 1$ km (black), $\hat{z} = 4$ km (blue), $\hat{z} = 7$ km (red), and $\hat{z} = 10$ km (green). The two sums on the left hand side of (B.15) have been truncated at $m = 800$. These plots, and others with different truncations, demonstrate that the left hand side of (B.15) converges in the mean to the right hand side of (B.15), thereby confirming the completeness of the basis functions $\mathcal{Z}_m(z)$ for the case of constant N.

To numerically confirm the completeness relation (A.10) for the case of constant N, we first write it in the form

$$[1 + \delta(z')] \left(\mathcal{Z}_0(z')\mathcal{Z}_0(\hat{z}) + \sum_{m=1}^{\infty} \mathcal{Z}_m(z')\mathcal{Z}_m(\hat{z}) \right) = \delta(z' - \hat{z}), \tag{B.14}$$

where, for notational convenience, we have replaced z by $\hat{z}$. The numerical confirmation of (B.14) is simpler if (B.14) is converted to an integrated form because then the two delta functions will not appear. Thus, integrating (B.14) over z' from zero to z, making use of (B.13), and finally multiplying by N^2/g, we obtain

$$\begin{aligned}
&\frac{A_0 N^2 z_T}{g\mu_0}\mathcal{Z}_0(\hat{z})\left\{\cosh(\mu_0)-\cosh\left[\mu_0(1-z/z_T)\right]\right\}\\
&+\sum_{m=1}^{\infty}\frac{B_m N^2 z_T}{g\nu_m}\mathcal{Z}_m(\hat{z})\left\{\cos\left[\nu_m(1-z/z_T)\right]-\cos(\nu_m)\right\}\\
&+\sum_{m=0}^{\infty}\mathcal{Z}_m(0)\mathcal{Z}_m(\hat{z})=\begin{cases}1 & \text{if } z>\hat{z}\\ \\ 0 & \text{if } z<\hat{z}.\end{cases}
\end{aligned} \tag{B.15}$$

Figure B.1 shows plots of the left hand side of (B.15) when $\hat{z}=1,4,7,10$ km and when 800 terms are used in the summation over m. Note that, except for the Gibbs phenomenon near $z=\hat{z}$, the left hand side of (B.15) converges to the unit step function as the number of terms is increased. This is numerical confirmation that (B.14) is valid and therefore that the basis functions (B.13) form a complete set in the special case of constant N.